Connecting the Chemical Composition of Planetary Atmospheres with Planet Formation

CONNECTING THE CHEMICAL COMPOSITION OF PLANETARY ATMOSPHERES WITH PLANET FORMATION

By

ALEXANDER J. CRIDLAND, M.SC.

A Thesis Submitted to the School of Graduate Studies in Partial Fulfilment of the Requirements for the Degree of Doctor of Philosophy in Physics

McMaster University

Descriptive Note
DOCTOR OF PHILOSOPHY (PHYSICS and ASTRONOMY) 2017
McMaster University (Physics and Astronomy) Hamilton, Ontario
AUTHOR: Alexander J. Cridland, M.Sc. (McMaster University)
SUPERVISOR: Dr. Ralph E. Pudritz
NUMBER OF PAGES: xv, 182

Abstract

What sets the observable chemical composition of exoplanetary atmospheres? The available chemical abundance of the planet's natal protoplanetary disk gas will have a deciding role in the bulk abundance of the atmosphere very early in the planet's life. While late accretion of ices and inter-atmosphere physical processing can change the observable chemical abundances. We have developed a theoretical model which connects the chemical and physical evolution of an accretion disk with the growth of a young planet to predict the bulk chemical abundance of the planetary atmosphere that is inherited from the disk.

We assess what variation in atmospheric chemical abundances are attributed to different planet formation histories. We find differences in the relative abundances of primary nitrogen carriers NH_3 and N_2 depending on *when* the planet accreted its gas. Early ($t < 1$ Myr) accreters predominately accreted warmer gas which tend to have its nitrogen in NH_3, while later protoplanets accrete colder, more N_2 dominated gas.

Furthermore we compute the carbon-to-oxygen ratio (C/O) for each planets, which is used to infer *where* a planet forms in its accretion disk. We find that each of our planets accrete their gas very close to the water ice line, thereby accreting 'pristine' gas with C/O_{planet} exactly matching its host star. We extend our results by tuning our initial disk parameters to reproduce the properties of the HL Tau disk. We produce three models that span the range of measured gas masses, and one model which studies a UV quiet system. We generally find that planet formation is efficient enough to produce a Jupiter-massed planet within the predicted 1 Myr age of the disk. We find a correspondence between the radial locations of ice lines within our astrochemical model and the set of observed dust gaps in the HL Tau system.

Acknowledgments

Producing this thesis has been a labour of love, one that I've never experienced before. I am forever grateful to Ralph, your tutelage and supervision has helped shape the work that lead up to what you see before you. I have learned a great deal in the four years that we have worked together. And I look forward to applying the research principles that you have bestowed on me as I continue my career - I'll also never again down play my work during research talks, thanks to your incessant reminding!

To my thesis committee members James and Ted, I am grateful for your support and helpful comments throughout the my time as a PhD researcher. And for a challenging defense! It made the success taste that much sweeter.

To my friends and family - I can never forget the love and support that I felt living as a graduate student. To my office mates: Mikhail, Rachel, Sam, Matt, Sarah, Ben, ... and of course Corey (who would ever forget Corey) - we've all been through a lot together, but we've gotten through it - thank you for your support!

To my parents and sister: you have always believed in me, and pushed me to be the best that I can be. Thank you for all the love you have given me, I hope only to make you proud!

Finally to Brittany: my most important source of strength. You have helped me through the stresses of graduate school like no other, and for that you will always have my love.

Contents

List of Figures

Chapter 1

Introduction

Several key observable properties of exoplanets (size, spectra, average density) depend on the chemical abundances of the gases in their atmospheres. What processes determine this? In the standard core accretion paradigm, the forming proto-planet accretes gas from its natal disk, and inherits the chemical composition of the disk gas in its immediate vicinity. While later, after the gas disk has evaporated, the planet can be enriched by the accretion of icy comets and asteroid-like objects. Both of these processes have an impact on observable properties such as relative abundance of carbon and oxygen (the so-called 'carbon-to-oxygen ratio' or C/O) in the gas of a planetary atmosphere.

The purpose of this thesis is to explore the connection between the astrochemical processes in the disk and the process of planet formation with the bulk chemical composition of early planetary atmospheres.

This link is complex as it involves many different physical and chemical processes. A particular difficult aspect of the problem is that determining the physical and chemical properties of the protoplanetary disk is a closed concatenation - meaning that certain properties of the gas can both govern *and* depend on the physical properties of the disk.

Because of its complexity the first models which linked disk astrochemistry to atmospheric chemical compositions simplified the problem by either considering reduced chemical models (ex. Öberg et al. (2011); Madhusudhan et al. (2014a)), or models of planet formation where the growth and migration of the planet are treated separately (ex. Madhusudhan et al. (2014a)). A common theme that span these previous works, as well as our own, is that the chemical composition of an exoplanetary atmosphere is broadly dictated by *where* a planet forms in relation to the radial location

of the disk's ice lines. Ice lines are positions in the disk where the gas temperature is sufficiently reduced to allow for volatiles to freeze out onto dust grains, and represent the most basic effect that astrochemistry can have on the chemical state of a planetary atmosphere. The water ice line, located at a gas temperature of ~ 170 K, is the most famously used ice line for discussing planet formation as it represents the location where the C/O of the gas changes drastically, and a location for efficient planet growth (see below).

The water ice line is typically the innermost ice line because water has the highest sublimation temperature of the common volatiles, and hence the depletion of water vapour across an ice line has not been directly observed by any generation of telescope. Farther out the gas temperature is much lower, allowing volatiles like CO to freeze out. The CO ice line (at a temperature of ~ 20 K) has been detected at radii between $\sim 30 - 160$ AU (Qi et al., 2013, 2015) according to observations of the rotational transitions of N_2H^+ and H_2CO gas. These chemical species can become abundant when CO freezes out because N_2H^+ is destroyed by reactions with gas phase CO, while H_2CO can be produced through the hydrogenation of frozen CO. More recently, Schwarz et al. (2016) used CO isotopologues to infer a location of $\sim 15 - 30$ AU for the CO ice line in the TW Hya disk.

At the ice line of any abundant volatile the C/O of the gas will change accordingly as the volatile freezes onto grains, and will imprint its C/O on any planet accreting gas in its vicinity. For the purpose of illustrating this point here, we assume that the disk gas is made up of only hydrogen, water, CO_2, and CO. We adopt the abundances of $1.5\times10^{-4}\times n_H$, $0.3\times10^{-4}\times n_H$, and $0.9\times10^{-4}\times n_H$ for CO, CO_2, and H_2O respectively (from Öberg et al. (2011)).

In Figure 1.1 we reproduce Figure 1 of Öberg et al. (2011) using the above abundances, and assuming that the water, CO_2, and CO ice lines are located at 2, 10, and 60 AU respectively. Additionally the carbon and oxygen contributions from carbon and silicate dust grains are included, which sets the C/O of the solid component inward of the water ice line. In this figure we see the simple, step-like nature of the disk C/O which is generally pictured in discussions of the effect that ice lines have on the available C/O for accreting planets. As one moves away from the host star the gas cools, eventually cooling to below the sublimation temperature of water vapour. At the water ice line the water freezes onto the grains, extracting oxygen from the gas (increasing C/O) and enhancing oxygen on the grains (decreasing C/O). Moving farther out we cross the CO_2 ice line, leaving only CO in the gas phase - with C/O = 1. Beyond the CO_2 ice line the solid C/O increases slight with the addition of frozen CO_2. Beyond the CO ice line the gas is fully depleted of heavy

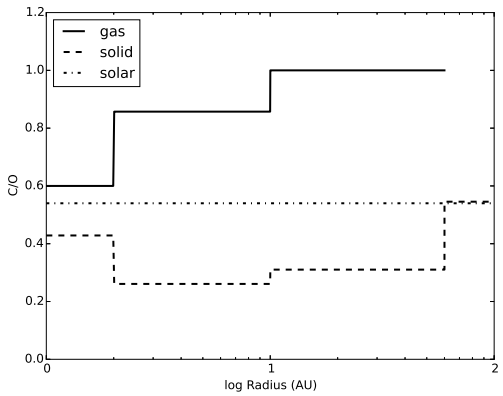

Figure 1.1: Recreation of Figure 1 from Öberg et al. (2011) demonstrating the C/O for a simple disk model. In this figure we fixed the location of the water, CO_2, and CO ice line to 2, 10, and 60 AU respectively. Included in this figure is the carbon and oxygen contributions from carbon and silicate dust grains. Solar abundances (0.54) are also shown for reference.

elements as CO freezes out.

If a planet formed at a single location in the disk then the connection between disk astrochemistry and planetary atmospheres would be very simple, since any measurement of their atmospheric C/O would directly relate to the chemical state of the gas disk from which they accreted. Additionally one would expect to observe a gradient in atmospheric C/O: with low C/O for closely orbiting planets and C/O ~ 1 for planets which orbit far from their host star. This simple picture is complicated by four factors: disk evolution, planetary migration, astrochemistry, and the late accretion of planetesimals.

Along with the gas, a growing planet will accrete solids into its atmosphere in the form of either planetesimals or pebbles. These solids will then deposit their frozen volatiles and solid content either directly onto the planet core, or into the atmosphere (e.g. Brouwers et al. (2017)). Jupiter could be a case study for atmosphere enrichment by solid accretion, because recently it has been observed that Jupiter is carbon rich relative to solar abundance. Gas accretion is unlikely to lead to a carbon enrichment, and so we likely require the accretion of solids to explain this enrichment.

Planetary migration occurs in two phases during a planet's life. While the gas disk is present, the planet perturbs the gas in its vicinity which either generates spiral arms at Lindblad resonances (Type-I, Ward (1997); Paardekooper (2014)) or opens a gap in the disk (Type-II, Lin & Papaloizou (1986); Ward (1997)). In both cases the protoplanet tends to move to smaller radii, and lower gas C/O. Migration changes where a protoplanet accretes its gas, and depending on the rate of migration and gas accretion, can allow the planet to sample a wider range of gas C/O than *in situ* formation

(Madhusudhan et al., 2014a). This last point will depend on the planet formation model, and will be discussed later in the chapter.

The second phase of planet migration occurs after the gas disk has dissipated, when the planet can gravitationally scatter other planetesimals left over from the early phase of planet formation (for example the Nice model, Gomes et al. (2005)). This scattering could shift the planet away from the radius where it formed, and confuse any attempt at linking the observed C/O to a formation history. While there is evidence for dynamical scattering (high eccentricity) in the Kepler data (Kane et al., 2012), planets with smaller orbital radii tended to have smaller eccentricities. These planets are most likely to produce observable spectra to assess the chemical composition of their atmosphere, so we generally ignore the impact of dynamical scattering in the remainder of this thesis.

Astrochemistry can impact the distribution of C/O as the disk ages, because the gas temperature cools and surface density is reduced as gas accretes through the disk and onto the host star. These evolving structures change the rates of astrochemical processes, altering the distribution of chemical elements in the disk (Helling et al., 2014; Eistrup et al., 2016). Most importantly for the C/O as the temperature of the disk is reduced the location of the ice lines shifts inward. This evolution shifts the solid and dotted lines of Figure 1.1 to lower radii, while maintaining their general shape. With the addition of more complicated astrochemical processes, like photochemistry, the shape of the curves in Figure 1.1 will also evolve as the surface density of the gas and dust is reduced with age, and the flux of high energy radiation increases.

A final impact on the observable C/O of a planetary atmosphere is the late accretion of pebbles and planetesimals which carry the frozen phase of abundant volatiles like H_2O and CO (Mordasini et al., 2016; Booth et al., 2017). This phase of accretion primarily occurs after the atmosphere has fully formed, and alters the C/O of the planet by delivering volatiles from elsewhere in the disk.

Moving forward, there has been some work dedicated to combining simple models of astrochemistry with complex planet formation models to study the chemical properties of terrestrial (Moriarty et al., 2014) and Jupiter-mass planet (Mordasini et al., 2016) formation. These models generally include the effects discussed above, and rely on a theoretical framework known as a 'chain' model (Mordasini et al., 2016). Each link of the chain is represented by a separate physical or chemical model, and can only impact the links that follow it. Our theoretical framework follows a similar flow, and will be discussed later in this work. The order of our models are: *Gas disk model* $\rightarrow$ *Dust model* $\rightarrow$ *Ionizing radiative transfer* $\rightarrow$ *Chemical model* $\rightarrow$ *Planet formation.* A benefit of our method is

that we can model important physics like the radial drift of dust and its effect on the disk opacity, and hence on the flux of high energy photons on the disk midplane which drive astrochemistry. On the other hand, Mordasini et al. (2016) used reduced chemical models but computed a self-consistent atmospheric model of the forming proto-planet

There are more complicated interactions that we are not considering with this framework. For example consider calculating the disk's ionization, or abundance of free electrons in the gas. Given that the turbulence in the disk is driven by the magnetorotational instability (MRI, Balbus & Hawley (1994)), the abundance of free electrons dictates how efficiently the magnetic field can couple to the gas, and produce turbulence at a rate faster than it can be dissipated (for ex. see Bai & Stone (2013, 2017)). The ionization depends primarily on photochemical processes, and hence on the flux of ionizing radiation. This flux depends on the amount of material along its line of sight, which itself depends on the density and scale height of the disk's dust and gas. So this simple question of how abundant are free electrons in the disk requires a cyclical chain of computationally expensive calculations to solve self-consistently.

In what follows we will discuss the theoretical and observational aspects of accretion disk physics and chemistry in chapter 1.1 and planet formation in chapter 1.2. Chapters 2-4 constitute the original, peer reviewed and published research in this thesis. In chapter 2 we present our theoretical framework, and three theoretical planets which were computed in our fiducial model. In chapter 3 the addition of a semi-analytic dust model which improved the treatment of dust physics, including the impact of radial drift is outlined. This addition updates our treatment of the dust distribution from a single grain size, constant gas-to-dust ratio to a grain size distribution determined by coagulation and fragmentation and a radially dependent gas-to-dust ratio which is more akin to observed disks. This change leads to a drastic difference in the planet formation history in our fiducial gas disk model. In chapter 4 we present the chemical results for the disk model presented in chapter 3. Chapter 4 also presents our first variations in initial conditions away from the fiducial model and discusses the prospect of full population synthesis models of our method. In chapter 5 we begin to apply our method to what has rapidly become the most important young, possibility planet forming disk - HL Tau. Finally in chapter 6 we conclude, and discuss the future prospects of this project.

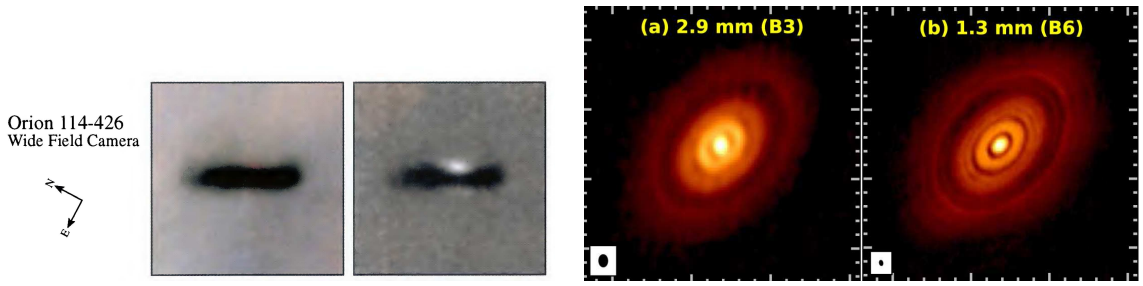

(a) Directly imaged edge-on protoplanetary disk by Hubble Space Telescope. The black band comes from the extinction of radiation caused by the disk's gas and dust. The disk diameter is 1012 AU, and was studied with an angular resolution of 0.1 arcsec/pixel. Reproduced with permission from McCaughrean & O'dell (1996) AJ 111 1977, DOI: 10.1086/117934, Figure 1, ©AAS.

(b) Highly resolved imaged of the (nearly) face-on dust emission in the HL Tau protoplanetary disk by ALMA. The disk diameter is 200 AU, and was studied with angular resolutions of 0.075 arcsec/pixel and 0.025 arcsec/pixel . Reproduced with permission from ALMA Partnership et al. (2015) ApJL 808 L3, DOI: 10.1088/2041-8205/808/1/L3, Figure 1, ©AAS.

Figure 1.2: Examples of observed protoplanetary disks.

1.1 Accretion Disk Physics and Chemistry

It has been well accepted that planet formation occurs within a disk of gas and dust around a young star. Certainly in our own solar system each planet lies along nearly the same orbital plane which suggests that they formed out of a disk-like geometry. On top of this limited evidence, the first observation evidence for disks around young protostars was provided by infrared excess in the spectral energy distribution of young stars by ground based observations Mendoza V. (1966). Later space based missions like the Hubble Space Telescope made direct observations of these planet forming systems (McCaughrean & O'dell, 1996) (see figure 2.1). In the era of the Very Large Array (VLA) (Carrasco-González et al., 2016) and Atacama Large Millimeter Array (ALMA) (ALMA Partnership et al., 2015) (see 1.2(b)) the structure of accretion disks have been brought into even greater focus, with the first high resolution images of a protoplanetary disk. The revolutionary recent mm image of HL Tau taken by ALMA (Figure 1.2(b)) with its large symmetric disk with its many gaps, has excited enormous interest from the planet formation community.

From a theoretical perspective, if star formation occurs through the direct collapse of a rotating, dense molecular cloud core (radius ~ 0.1 pc $\sim 4 \times 10^6$ $R_\odot$) to a star (radius $\sim R_\odot$) then the moment of inertia decreases by a factor of $\sim 10^{13}$! If angular momentum is not lost during this process, the resulting star would have an absurdly large rotation rate (Lynden-Bell & Pringle, 1974). One can show that a natural way of solving this issue is by first accreting most of the gas and dust onto a disk (Hartmann, 2009) which under the action of some general 'viscous stress', leads to inward transport

of disk material with the accompanying outward angular momentum transport and spreading of the disk (Lynden-Bell & Pringle, 1974).

In this chapter we will outline the physical models which motivate our model presented in chapters 2 and 3. Additionally we will discuss basic chemical processes which will govern the distribution of chemical species in the disk.

1.1.1 Disk Structure - Gas and Dust

Gas Viscous Evolution

The process of planet formation occurs on a similar timescale as the lifetime of a protoplanetary disk. So taking the disk evolution into account is an important aspect of any planet formation model. Generally the evolution of the gas is best described by (Lynden-Bell & Pringle, 1974)

$$\frac{\partial \Sigma}{\partial t} = \frac{3}{r}\frac{\partial}{\partial t}\left[r^{1/2}\frac{\partial}{\partial r}\left(r^{1/2}\nu\Sigma\right)\right] + \dot{\Sigma}_{ext}(r,t), \tag{1.1}$$

where Σ and ν are the surface density and viscosity of the gas disk at radius r and time t. The time and position dependent function $\dot{\Sigma}_{ext}$ describes additional sources of surface density evolution that are seperate to the viscous accretion of gas through the disk. These sources could be through photoevaporation (ex. Gorti et al. (2015)) or external accretion from a surrounding envelope. In what follows we will assume that the envelope from which the star had first accreted has completely dissipated, so that external accretion is negligible. Furthermore, photoevaporation is generally a difficult concept to include analytically, so we will leave its impact on the gas evolution to chapter 2.

Assuming that viscous accretion is the sole source of evolution (ie. $\dot{\Sigma}_{exp}(r,t) = 0$) then Equation 1.1 is known as the diffusion equation. Lynden-Bell & Pringle (1974) showed that self-similar analytic solutions to the diffusion equation exist if the viscosity is a power-law of the disk radius. This dependence is obtained by the standard 'α-disk' model of Shakura & Sunyaev (1973), where the viscosity can be written as:

$$\nu = \alpha c_s H, \tag{1.2}$$

where c_s and H describe the gas sound speed and scale height respectively. The parameter α describes the relative strength of turbulence, and is defined as the ratio of the turbulent pressure to

gas pressure (Shakura & Sunyaev, 1973).

A self-similar solution implies that the surface density can be decomposed into time-dependent and radial-dependent parts:

$$\Sigma(r,t) = \Sigma_0(t) f\left(\frac{r}{S(t)}\right), \tag{1.3}$$

where f is a dimensionless function that solves the steady state solution of equation 1.1, and $S(t)$ denotes the outer radius of the disk, and acts as the scale factor for the self-similar solution (Ruden, 1993; Stepinski, 1998).

Following Stepinski (1998) the total disk mass and angular momentum has the form:

$$M_d = 2\pi\Sigma_0 S^2 \mathcal{J}_M, \qquad \mathcal{J}_M = \int_{\frac{R_{in}}{S(t)}}^{1} \xi f(\xi) d\xi, \tag{1.4}$$

$$J_d = 2\pi(GM_*)^{1/2}\Sigma_0 S^{5/2}\mathcal{J}_J, \qquad \mathcal{J}_J = \int_{\frac{R_{in}}{S(t)}}^{1} \xi^{3/2} f(\xi) d\xi, \tag{1.5}$$

Because angular momentum is conserved in the disk Stepinski (1998) combined equations 1.4 and 1.5 to determine how Σ_0 and M_d scale with time:

$$\Sigma_0(t) = (1.58 \times 10^5 g\ cm^{-2})(j/\mathcal{J}_J m^{-1/2} s^{-5/2}, \tag{1.6}$$

$$m_d(t) = 0.11\mathcal{J}_M(j/\mathcal{J}_J)m^{-1/2}s^{-1/2}, \tag{1.7}$$

where we introduce the unitless variables: $m = M_*/M_\odot$, $m_d = M_d/M_\odot$, $j = J_d/(10^{52} g\ cm^2\ s^{-1}$, $s = S/1$ AU, and $r = R/1$ AU. With the determination of the time-dependent component, what remains is to determine the functional form of $f(r/s)$. For that, one relies on the assumption that the disk is accretion material in what is known as a steady disk flow. For a steady disk, Σ has no explicit time dependence, which forces the mass accretion rate of be approximately constant in radius (Frank et al., 1985), with:

$$\dot{M}(t) = 3\pi\nu\Sigma. \tag{1.8}$$

This formalism allows for the determination of $f(r/s)$, provided the radial dependence of ν is known. In an α-disk model (eq. 1.2) this is equivalent to finding the radial temperature structure of the

disk. We will discuss the heating processes in the disk in a later section.

This simple analytic construction provides an excellent underlying model for an evolving disk that can be used for more difficult problems like astrochemistry and planet formation. Its evolution can be easily computed for many million years, covering a wide range of disk lifetimes and initial conditions. One downside of this approach is that it generally requires a fair number of approximations and simplifications to reach a tractable solution. One such simplification is the α-disk model which generalizes the turbulent nature of the disk into a single (constant) parameter. This is a necessary measure which has historically lead to an excellent agreement between theory and observation.

In most standard protoplanetary disk models, and indeed in chapter 2, one assumes that the dust and gas are perfectly coupled with a constant mass ratio. This assumptions works well for small grains, which are indeed coupled to the gas dynamics, but begins to fail when the dust grains grow to larger sizes. More complicated models of dust physics are outlined in the following section. These models are featured in chapters 3 and 4.

Dust Physics

The evolution of the dust has two important implications in our work. First, it is well known that the dust can evolve separately from the viscous evolution of the gas (Blum & Wurm, 2008a; Williams & Cieza, 2011; Birnstiel et al., 2012) so the assumption of perfectly coupled dust is not consistent with observations. Secondly the growth and evolution of the dust is the first step in forming a planet, and its distribution greatly impacts the rate at which the core of the planet grows (Kokubo & Ida, 2002; Ida & Lin, 2004).

The dynamics of small dust grains is completely dictated by the gas, and will flow along the streamlines of the gas. The gas dynamics is dominated by gravity, however gas pressure support dictates that its orbit is not strictly Keplerian. Grains that can decouple from the gas are pressureless, and hence orbit at Keplerian speeds. These grains feel a head wind and lose angular momentum, evolving to smaller radii in a process known as radial drift (Weidenschilling, 1977). The evolution of the dust grain is determined by its Stokes number (Birnstiel et al., 2012)

$$St = \frac{t_{stop}}{t_L}, \tag{1.9}$$

where t_{stop} is the particle stopping time in the gas and t_L is the eddy-turnover time of the largest

turbulent eddy. When the grain size is less than the mean-free path of the gas (Epstein drag law), the grains are approximately spherical, the gas is described by an isothermal density profile, and $t_L \sim \Omega^{-1}$ (Cuzzi et al., 2001) the Stokes number has the form:

$$St = \frac{a\rho_s}{\Sigma}\frac{\pi}{2}, \tag{1.10}$$

where a is the radius of the dust grain, and ρ_s is the internal density of the grain. When $St < 1$ the grain is well coupled to the gas, following its sub-Keplerian orbit. Otherwise the grain will radially drift inward towards the host star. In this way, radial drift limits the maximum size of the dust grains in a disk when the radial drift timescale becomes smaller than the coagulation (growth) timescale. Assuming a self-similar solution for the disk gas density, the maximum grain size depends on disk radius as a power-law (Birnstiel et al., 2012):

$$a_{max,drift} \propto \frac{\Sigma_d}{\rho_s}\frac{V_k^2}{c_s^2}, \tag{1.11}$$

where Σ_d is the dust surface density, and V_k is the Keplerian orbital speed.

A second way of limiting the maximum size of a dust grain, is through fragmentation. If two grains collide with a similar kinetic energy as its internal binding energy, they can break apart (Borkowski & Dwek, 1995; Brauer et al., 2008). Fragmentation is required to explain the existence of small grains in the interstellar medium (Mathis et al., 1977), otherwise coagulation would efficiently use up the smaller grains in building larger ones (Dullemond & Dominik, 2005). The balance between fragmentation and coagulation produces a population of grain sizes (or equivalently mass m) which follows a power-law (Dohnanyi, 1969):

$$n(m)dm \propto m^{-\xi}dm, \tag{1.12}$$

where the exponent $\xi \sim 1.8$ has been determined from theoretical work and observations (Dohnanyi, 1969; Draine & Lee, 1984).

At some mass range in equation 1.12 the population drops dramatically. This maximum grain size occurs when the rate of fragmentation surpasses the growth rate of grains up to that particular size, meaning that grains of size a_{max} fragment faster than they can be built. The maximum grain

from fragmentation also depends on radius as a power-law (Birnstiel et al., 2012):

$$a_{max,frag} \propto \frac{\Sigma_d}{\rho_s} \frac{u_f^2}{c_s^2}, \tag{1.13}$$

where u_f known as the fragmentation threshold speed. Generally we assume that u_f is a constant, when in reality it depends on the chemical structure of the dust grain, the presence of ice, and the shape of the grain (Blum & Wurm, 2008a; Wada et al., 2008; Gundlach et al., 2011).

In real systems both fragmentation and radial drift act to limit the maximum size of the dust grain population, so one would expect to observe the maximum grain size depending on two power-laws, one where fragmentation dominates a_{max}, and one where radial drift dominates.

More details of our dust model are presented in Chapter 3 and its implication to planet formation is presented in Chapter 4. A current inconsistency between theory and near- and mid-infrared observations of protoplanetary disks is the survivability of dust in the outer disk. Dust radial drift rates are currently too high to explain the dust that is observed in the dust emission of disks (see the review by Testi et al. (2014)). In Chapter 3 we showcase our implementation of the dust model introduced in Birnstiel et al. (2012), and demonstrate the differences in the ionization structure of the gas between the constant gas-to-dust model and the Birnstiel et al. (2012) model. Since the radial drift rate is too high in the Birnstiel et al. (2012) model, our framework represents the results of the extremes of dust modelling (no radial drift / fast radial drift), with the true results existing somewhere in between.

1.1.2 Disk Structure - Temperature

In an α-disk model (eq. 1.2) (ie. one in which angular momentum is transported by an average stress taken to be proportional to the disk pressure - the origin of the stress is most often taken to be MRI turbulence, but can also arise from wind torques in which the angular momentum is carried off vertically from the disk) the radial structure of the temperature ultimately sets the radial structure of the gas surface density. The disk has two primary sources of heating: viscous heating and direct irradiation. As mass accretes through the disk it dissipates its gravitational energy, turning it into heat. This dissipative term in the energy equation of a viscously evolving accretion disk (Lynden-Bell & Pringle, 1974) acts as a heating source, and produces a temperature radial power-law with an exponent of $-3/4$. From this temperature profile, Lynden-Bell & Pringle (1974) derived a theoretical

spectral energy distribution (SED) of $\nu F_\nu \sim \nu^n$, where $n = 4/3$, for a disk around a young star.

By coincidence this same SED results from the blackbody emission of a flat, passive disk which remits the radiation it absorbs from its host star. This reprocessing of stellar emission is the second source of heating, and will be known as 'direct irradiation'. An issue with the SEDs of both the blackbody disk and the viscously accreting disk was raised by Chiang & Goldreich (1997). It was pointed out that while both model predict $n = 4/3$, observations of protoplanetary disks frequently derived flatter SEDs with $n \leq 3/4$ (Chiang & Goldreich, 1997). A way of explaining this discrepancy is by considering a disk that flares due to hydrostatic equilibrium at high radii (Kenyon & Hartmann, 1987), which can produce the flatter spectra. Chiang & Goldreich (1997) derived the midplane temperature and SED for a flared accretion disk which was only heated by direct irradiation, and showed that the flared geometry did indeed improve the fit to observations.

In reality both heating sources would be active simultaneously, as argued by Chambers (2009). In the inner regions of the disk, where flaring is suppressed, direct irradiation would tend to produce lower temperatures than would be produced by viscous heating. So one would expect that these inner regions of the disk would be dominated by viscous heating. Meanwhile the outer region of the disk, where flaring becomes significant, the disk can absorb much more energy from direct irradiation than it would produce through viscous evolution. Hence the heating of these outer regions would be dominated by direct irradiation. Each of these heating processes produce a temperature structure with their own radial profile, so the global temperature profile is described by a split power-law with a particular transition point which we will call the 'heat transition'. The radial position of this heat transition is important for planet formation, as will be discussed later.

As the disk evolves the mass accretion rate drops along with the surface density of the gas. Since the mass accretion rate drives the heating in the viscous regime, the temperature of this region will also be reduced. The time evolution of the temperature structure is shown in chapter 2, and here we note the important feature. As the temperature drops in the viscous regime, the heat transition point moves inward and more of the disk is heated by direct irradiation. As the disk evolves the Chambers (2009) derived temperature profile evolves towards the profile derived by Chiang & Goldreich (1997). The evolving temperature profile has important implications on understanding the chemical structure of the disk, as will be discussed in the following section.

In computing the evolution of the mass accretion rate we assume that it smoothly drops with time. This naturally ignores bursts of accretion that can occur due to gravitational instabilities.

These bursts of accretion naturally occur in T Tauri stars as they form. Traditionally known as FU Orionis stars, young stellar systems can undergo accretion bursts of approximately 1000× the standard mass accretion rates through accretion disks (see the review by Bertout (1989)). The mass accretion burst raise the temperature of the disk gas significantly, shifting the chemical features of the gas (like ice lines) to larger radii. It is unclear how these mass accretion bursts will impact our planet formation model below, and how greatly impacted the disk chemistry will be - both of these points will depend on the size of the relevant timescales involved.

1.1.3 Disk Structure - Effect of a Forming Planet

As seen in the ALMA image of HL Tau (Figure 1.2(b)) protoplanetary disks are not the smooth systems as is suggested by Equation 1.3. Possible explanations include density bumps due to opacity transitions (ie. ice lines), a change in the dust properties (ie. average size), or carved by the gravitational influence of planets. These gaps should, in principle, change the accretion of material through the disk as well as the temperature profile. However these latter effects are beyond the scope of this thesis.

A forming planet can also sculpt its natal disk through dynamic interaction with other forming embryos for example through mean motion resonance (MMR) trapping. In our own solar system MMR trapping of Jupiter and Saturn has been proposed to have lead to the structure of our inner solar system (Walsh et al., 2011). Numerical (Pierens & Nelson, 2008) and analytic (Batygin, 2015; Xu & Lai, 2017) studies have shown that MMR trapping is a robust result over a large mass range of a three body system evolving in a gas disk. If a planetary embryo is captured at a MMR with a theoretical inner planet, that embryo will carve out a dust gap in its disk. Similar trapping can occur at condensation fronts (ice lines) of abundant volatiles in the disk. If these embryos carve out a gap in the dust, then we would expect a correspondence between the radial location of the observed dust gaps and the locations of the ice lines.

In chapter 5 we will tailor our theoretical model to best represent the physical properties of the HL Tau disk and investigate whether planetary embryos, trapped at ice lines, are the cause of the observed dust gaps.

1.1.4 Disk Chemistry

Table 1.1: Example of astrochemical processes and rates

	reaction	rate	unit
Photodissociation	$AB + h\nu \rightarrow A + B$	10^{-9}	s^{-1}
Neutral-neutral	$A + B \rightarrow C + D$	4×10^{-11}	cm^3s^{-1}
Ion-molecule	$A^+ + B \rightarrow C^+ + D$	2×10^{-9}	cm^3s^{-1}
Charge-transfer	$A^+ + B \rightarrow A + B^+$	10^{-9}	cm^3s^{-1}
Radiative association	$A + B \rightarrow AB + h\nu$		
Dissociative recombination	$A^+ + e \rightarrow C + D$	10^{-7}	cm^3s^{-1}
Associative detachment	$A^- + B \rightarrow AB + e$	10^{-9}	cm^3s^{-1}

Recreation of table 4.1 in Tielens (2005)

Tielens (2005) describes astrochemistry as "a cosmic dance of the elements in which atoms are constantly reshuffled from one species to another." In a protoplanetary disk there are many thousand of different chemical reactions that may take place, but they can broadly be grouped into three families: bond-formation reactions such as radiative association, bond-destruction reactions such as photodissociation, and bond-rearrangement reactions such as charge-transfer and neutral-neutral reactions (Tielens, 2005).

In Table 1.1 we show a list of gas phase reactions that are present in astrochemical settings along with an estimate of their rates - from this table we see a hierarchy of chemical reactions. If an ion can react with molecular hydrogen, those reactions will tend to dominate because of H_2 is the most abundant molecule in the disk. Otherwise the recombination of a positive ion with a free electron is the most efficient destructive pathway for ions. If neither of these reactions proceed an ion will be used up through a reaction with a neutral molecule. In the gas, neutrals tend to react with ions if they are available, otherwise neutral-neutral reactions become important.

Left off of Table 1.1 are the ionization reactions which produce the free electrons and ions discussed above. T Tauri stars are strong X-ray sources with luminosities between $10^{29} - 10^{31}$ erg s^{-1} (Fogel et al., 2011). Direct irradiation efficiently ionizes the upper atmosphere of the disk, while the midplane remains neutral. Farther out in the disk X-rays can scatter down to the midplane, increasing the electron fraction substantially. Additionally, cosmic rays ionize the gas far out in the disk, where the surface density is below ~ 96 g cm^{-2} (Aikawa & Herbst, 1999; Fogel et al., 2011).

Generally, the number density n of the i^{th} gas in our chemical system will evolve as (Tielens,

2005):

$$\frac{dn(i)}{dt} = -n(i)\sum_j n(j)k_{ij} + \sum_{j,k} n(j)n(k)k_{jk} + \sum_j n(j)k_j - n(i)\sum_j k_j. \tag{1.14}$$

The first term denotes bimolecular reactions that use the i^{th} gas molecule as a reactant. The second term is all bimolecular reactions that produce the species i. The third and fourth terms denote unimolecular reactions like photodissociation which create and destroy the i^{th} gas molecule respectively. The parameters k_j and k_{jk} are the reaction rates for any given chemical reaction. These sets of reactions can be combined with conservation equations for each of chemical element, and solved numerically (Tielens, 2005).

These rates can depend on the temperature profile, and hence at a particular radius the cooling discussed in the previous section will change the molecular abundance of gas as the disk ages. This is most easily seen in neutral-neutral reaction which have reaction rates of the form (Tielens, 2005):

$$k_{jk} = \alpha \left(\frac{T}{300\text{ K}}\right)^{\beta} \exp\left[\frac{-\gamma}{kT}\right], \tag{1.15}$$

where the parameters α, β, and γ are derived from experiment. Because most reactions have activation barriers (γ) they require a higher temperature before they can proceed. So as it cools, the gas molecular abundance will shift way from molecules that require high activation barriers to form.

Dust grains can act as a catalyst to gas chemistry because they offer a surface for gas molecules to meet and react more quickly than they would in the gas phase, as well as circumventing their activation barrier. The accretion of gas species on the grains is the limiting step in the surface chemistry (Tielens, 2005), which scales with the surface area of the dust grain, and can be as low as a few days in a dense environment (Tielens, 2005). Once accreted, the gas species must travel across the grain to find a reaction partner, since the probability of a gas accretion at the same position as the first is low. Light elements like hydrogen can easily explore the whole grain. Heavier species like carbon, nitrogen, and oxygen do not travel as rapidly, but can still sample most of the grain. The largest elements and molecules can not travel far and are effectively trapped at their accretion position. Because it travels to much of the grain, hydrogenation can be an efficient process on dust grains (see Qi et al. (2013)).

In our work, dust grain surface chemistry is only used in the production of H_2 and H_2O. The grains

are also important for the capture and transfer of free electrons which efficiently drives chemistry, as well as a source for gas freeze out. In this way, the grains primarily act as a catalyst of electron transfer and ion chemistry as well as the site for the formation of ice. Our implementation of chemistry is explained in more detail in chapter 2.

1.2 Planet Formation - Observations and Theory

1.2.1 Observational Constraints

Over the last decade the number of observed planets has skyrocketed. Thanks to the *Kepler*, *Hubble* and ground based missions, along with future space based missions *TESS* and *PLATO*, we now live in an age where planet formation has become a statistical science.

In Figure 1.3 we show the mass and semi-major axis of all known exoplanets from the online database *exoplanet.eu*. The colour denotes the detection method of each planet, for planets discovered through transit we only show planets for which mass data was available. In this figure we can see three primary populations: Hot Jupiters ($M > 0.1$ M_{Jup}, $R < 0.1$ AU), Warm Jupiters ($M > 0.1$ M_{Jup}, $0.5 \lesssim R \lesssim 10$ AU), and Super Earths ($M < 0.1$ M_{Jup}). There is another population of planets with $R > 10$ AU, however these are few and far between because they occupy a region of parameter space that is hard to observationally explore. In what follows we will only consider the formation of the three primary populations.

Each of these populations, indeed each planet, has undergone a different formation history which has defined the planetary properties we observe today. It is the goal of planet formation theory to try to link the distribution of initial conditions of disks at their formation to the range of planetary properties seen, as an example, in the mass, semi-major axis diagram. Roughly speaking, the disk's initial mass and lifetime greatly impact how quickly and how massive a planet can grow. Particularly light or short lived disks will struggle to make Jupiter sized planets. Additionally the chemical composition of the dust in a disk impacts the rate at which a planet can accrete an atmosphere (Mordasini et al., 2014). As a result the metallicity of the host star (which is assumed to match the metallicity of the disk) will also play a role in shaping the formation history of the planet.

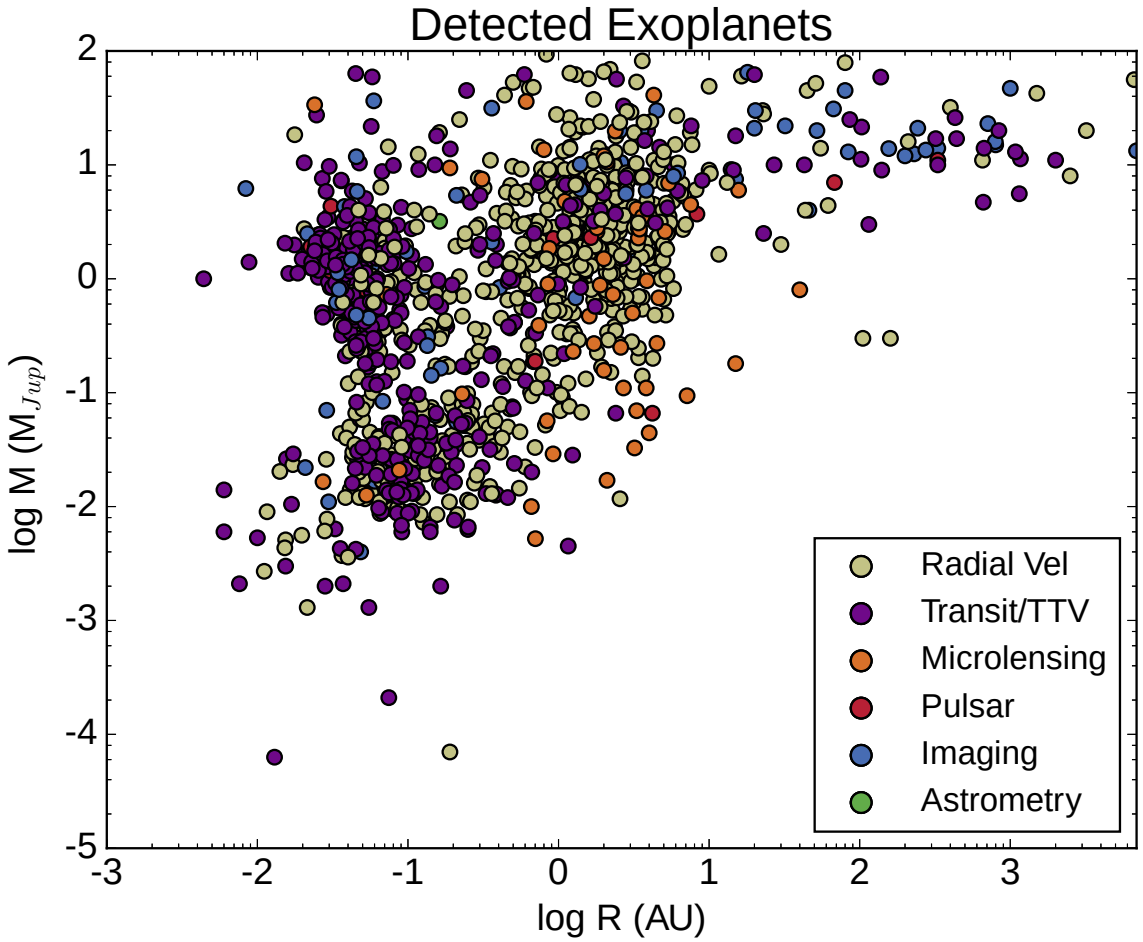

Figure 1.3: Mass and semi-major axis of all known exoplanets. Data taken from *http://exoplanet.eu/catalog/* on May 22nd 2017. The colours denote the observational method by which the planet was discovered.

Spread in Initial Conditions

The disk's initial mass sets the surface density of gas that is available for accretion, while the disk's lifetime ultimately limits the window of time that the planet has to grow. The range of initial disk masses is difficult to estimate observationally because young disks tend to be surrounded by a thick envelope of gas and dust. However given that stars form out of turbulent initial conditions one would expect from the central limit theorem that their mass distribution would be described by a lognormal function. Indeed observations have shown that the stellar initial mass function is described by the combination of a lognormal function with a power-law tail (Chabrier, 2003). It is reasonable to assume that disks would share a similar spread in initial masses, since most accretion onto the star occurs through the disk.

There is observational evidence of older disks which suggests that the disk mass can be described by a Gaussian distribution centred near the Minimum Mass Solar Nebula (MMSN) with $M_{MMSN} \sim 0.01$ $M_\odot$ (Beckwith & Sargent, 1996). Because these observed disk will be a few Myrs old when they are observed we assume that the 'initial mass' function for protoplanetary disks are Gaussian functions that are shifted to heavier masses. Given a standard mass accretion rate of $\sim 10^{-7}$ $M_\odot$ yr^{-1} and the approximate age of the observed systems ~ 1 Myr we choose an initial mass of $M_0 = 0.1$ $M_\odot$ for our fiducial disk model.

Large surveys of star forming regions have been used to study the lifetime of protoplanetary disks (see for example Hernández et al. (2007); Haisch et al. (2001); Strom et al. (1989); Wilking et al. (1989)). These studies find disks around almost all proto-stars of ages ≤ 1 Myr, while nearly all proto-stars older than 10 Myr do not have disks. Hernández et al. (2007) demonstrated that star forming regions with ages between 3-4 Myr had approximately half of their star systems with disk, suggesting that fiducial disk ages may be between 3-4 Myr. In our fiducial models presented in the following chapters we assume that the disk lasts for 4 Myr.

1.2.2 Core Accretion Model of Planet Formation

While planets start out as micron size grains, they quickly grow to kilometre sized objects through a combination of coagulation and hydrodynamic instabilities (see below). As discussed before, this growth is limited by both radial drift and fragmentation which should end the story of planet formation. However a process known as the streaming instability (Youdin & Goodman, 2005; Johansen

et al., 2007) allows for a rapid growth of the first planetary cores and planetesimals which ultimately lead to the formation of planets (Schäfer et al., 2017).

There are currently two variants of the core accretion theories that explain the formation of planets: planetesimal accretion and pebble accretion. The planetesimal accretion model produces planetary cores by accreting planetesimals (size $\sim 10 - 100$ km) on to a 'seed' core (size ~ 1000 km). Such a system is consistent with the initial mass function produced by Schäfer et al. (2017). Likewise, it has been suggested that pebble accretion can build a large planetary core up to ~ 10 $M_\oplus$ from an initial seed core (mass ~ 0.01 $M_\oplus$) by rapidly accreting centimetre sized dust pebbles. The primary difference between the two formation models is the rate at which the planetary core grows. In pebble accretion the core is fed by the rapid radial drift of pebbles, while in planetesimal accretion the planetary core is built by the slower accretion of planetesimals. Recently, it has been shown that pebble accretion struggles to make planetary cores with masses greater than ~ 0.6 $M_\oplus$, because pebbles generally ablate in the planetary envelope before they can reach the core (Brouwers et al., 2017). Planetesimal accretion has historically been used in population synthesis methods (for instance Ida & Lin (2004); Hasegawa & Pudritz (2013); Mordasini et al. (2015, 2016)) to compute the formation of the three primary populations on the mass-semi-major axis diagram - as a result we will be using it in what follows.

Both variants of core accretion begin with a ~ 0.01 $M_\oplus$ mass 'seed' core. It is assumed that the core is built up from the disk's dust through the streaming instability, and is surrounded by a sea of smaller planetesimals (in the case of planetesimal accretion described above) (Ida & Lin, 2004). The core accretion model predicts that a gas giant would be composed of two structural components - an inner solid core on which a gas envelope will accrete. Recently the JUNO mission to Jupiter has begun to measure its internal structure by means of sensitive gravity measurements done from close planetary orbits. The first results of this mission shows that Jupiter likely has a solid core (Bolton et al., 2017), however a measurement of the mass of this core is left to future analysis.

Below we will discuss the formation scenario outlined by the planetesimal accretion model. The core accretes planetesimals from a region of the disk often called the core's 'feeding zone'. This feeding zone scales with the core's Hill radius:

$$r_H \equiv \left(\frac{M_c}{3M_*}\right)^{1/3} r, \tag{1.16}$$

where r is the location of the core, and M_c is its mass. The size of the feeding zone $\Delta r_c \sim 7 - 10\, r_H$ depending on whether gravitational focusing is considered (ie. larger feeding zone) or not - this process is known as Oligarchic growth (Kokubo & Ida, 1998). The mass accretion rate of Oligarchic growth for a core at disk radius r is (Safronov, 1966; Ida & Lin, 2004):

$$\dot{M}_c \sim 2\pi \left(\frac{R_c}{r}\right)\left(\frac{M_c}{M_*}\right)\left(\frac{r\Omega_K}{\sigma}\right)^2 \Sigma_d r^2 \Omega_K, \tag{1.17}$$

where Ω_K is the Kepler frequency, and R_c is the radius of the core. For a planetesimal within the feeding zone to accrete onto the core, its velocity dispersion (σ) relative to the core must satisfy (Ida & Lin, 2004):

$$\frac{\sigma}{\Omega_K} \sim \Delta r_c \sim 10 \left(\frac{M_c}{3M_*}\right)^{1/3} r, \tag{1.18}$$

so that the timescale of Oligarchic growth is:

$$\tau_{c,acc} = \frac{M_c}{\dot{M}_c} \sim \left(\frac{r}{R_c}\right)\left(\frac{M_c}{\Sigma_d r^2}\right)\left(\frac{M_c}{M_*}\right)^{-2/3} \frac{2\pi}{\Omega_K}. \tag{1.19}$$

With the inclusion of gas-drag on the velocity dispersion Kokubo & Ida (2002) derived a new timescale:

$$\begin{aligned}\tau_{c,acc} \simeq 1.2 \times 10^5 \text{yr} &\left(\frac{\Sigma_d}{10\text{g cm}^{-2}}\right)^{-1} \left(\frac{r}{1\text{ AU}}\right)^{1/2} \left(\frac{M_c}{M_\oplus}\right)^{1/3} \left(\frac{M_*}{M_\odot}\right)^{-1/6} \\ &\times \left[\left(\frac{\Sigma}{2.4 \times 10^3 \text{g cm}^{-2}}\right)^{-1/5} \left(\frac{r}{1\text{ AU}}\right)^{1/20} \left(\frac{m}{10^{18}\text{g}}\right)^2\right],\end{aligned} \tag{1.20}$$

where m is the mass of incoming planetesimals, and the growth of the core is described by $\dot{M}_c = M_c/\tau c, acc$. For a fiducial setup the core initially (when $M_c = 0.01 M_\oplus$) grows with timescale of $\sim$ 25000 yr, however as the core accretes material this timescale lengthens. The slowed accretion rate is related to the gravitational impact that the growing core would have on the remaining sea of planetesimals. As it grows the core will tend to gravitationally scatter the surrounding planetesimals ultimately shutting off further accretion.

Eventually the core mass is heavy enough that its feeding zone is nearly cleared out of planetesimals ($\dot{M}_c$ is reduced), the core will begin to accrete gas. The forming gas envelope is heated by

the further accretion of planetesimals, and hence the gas accretion is limited by the gas envelope's ability to efficiently cool, thereby shedding its gravitational energy. We define a critical mass above which the core is sufficiently large that the gas envelope can cool efficiently and contract onto the core (Ikoma et al., 2000; Ida & Lin, 2004):

$$M_{c,crit} \simeq 10 \left(\frac{\dot{M}_c}{10^{-6}\ \mathrm{M_\oplus\ yr^{-1}}} \right)^{0.2-0.3} \left(\frac{\kappa}{1\ \mathrm{g\ cm^{-2}}} \right) \mathrm{M_\oplus}, \tag{1.21}$$

where κ is the opacity of the gas envelope, and the range of exponents depend on the choice of opacity table (Ida & Lin, 2004). Once the core has surpassed this critical mass, gas accretion will proceed at a rate that is dictated by the Kelvin-Helmholtz timescale, which Ikoma et al. (2000) derived:

$$\tau_{KH} \sim 10^b \left(\frac{M_c}{M_\oplus} \right)^{-c} \left(\frac{\kappa}{1\ \mathrm{g\ cm^{-2}}} \right) yr, \tag{1.22}$$

where the exponents b and c fall in the range $8-10$ and $2-4$ respectively, and the dependence of κ is often ignored (Ida & Lin, 2004). In our work we adopt $b = 9$ and $c = 3$ while ignoring the effects of κ, we discuss this in more details in future chapters.

For fiducial values in Equations 1.21 and 1.22 a core will begin accreting gas when it reaches a mass of $\sim 10\ \mathrm{M_\oplus}$ with an accretion timescale of $\sim 10^6$ yr. This timescale is on the same order as the viscous timescale of the accretion disk, which would imply that the disk might change substantially while the planet accretes its atmosphere.

The above analysis has assumed that planetesimals are efficiently produced from a dust disk. This fact has been demonstrated in numerical simulations of the streaming instability and pebble accretion (Schäfer et al., 2017). Pebble accretion has been used as a core formation variant where the planetary core grows not by the accretion of planetesimals, but by the accretion of cm-sized pebbles. The time scale associated with pebble accretion scale nearly identically to the planetesimal formation time scale: $\tau_{c,peb} \propto \tau_{c,acc}$ (Bitsch et al., 2015) however $\tau c, peb$ is roughly $1000\times$ smaller than $\tau c, acc$ for the same core mass. This result is partially caused by radial drift bringing fresh pebbles to the forming core from farther out in the disk, and partially by the fact that pebbles orbit at sub-Keplerian speeds - expanding the core's feeding zone. As a result planets grow much faster in the pebble accretion model than in planetesimal accretion. The difference in accretion rate has important implications on the derived population of planets, because a fast accretion rate

can neglect the impact of planet migration. As discussed before, recent simulations of planetary formation through pebble accretion have demonstrated that the accretion of pebbles struggle to produce planetary cores no larger than ~ 0.6 $M_\oplus$ (Brouwers et al., 2017), while the same analysis demonstrate that planetesimals do not suffer the same ablation that limits core growth through pebble accretion. Because of its apparent limited impact on the formation of large planets, we ignore the impact of pebble accretion in this thesis.

There are two important implications for the relative size of the accretion timescale and the viscous timescale. First if the molecular abundance of the gas changes as the planet accretes, the timing of its atmosphere accretion could be observed in its atmospheric chemical abundances. Second, the planet may change its orbital position through a process known as planet migration (see below), and migrate to a chemically different position in the disk to accrete the majority of its gas. In both cases our hope is that the through observations of exoplanetary atmospheres we can differentiate planets which underwent different planet formation histories, and learn more about the process of planet formation.

1.2.3 Planet Migration

When the gas disk is present, a planet rarely remains at the same orbital radius. As it grows the planet perturbs the surrounding gas forming spiral density waves or opening up gaps in the gas disk. At low mass, the global structure of the disk is effectively unchanged, apart from spiral density waves that are generated by Lindblad resonances - this is known as Type-I migration. These density waves interact gravitionally with the planet, transferring angular momentum and causing the planet to change its orbital radius. The closest inner and outer Lindblad resonances contribute strongest to the transfer of angular momentum. The outer resonance generally lies closer to the planet than the inner resonance, which generally results in a net outward transfer of angular momentum and an inward migration of the planet (Ward, 1997; Seager, 2010).

In Figure 1.4 we can easily see the structure that is perturbed by the planet. The outer spiral arms tends to have more material, leading to outward angular momentum flux and inward migration. As the planet grows it slowly carves a gap out of the annulus of gas centered on its orbital radii. Eventually the gap becomes large enough that it encompasses the Lindblad resonance radii, shutting off the production of the spiral arms and turning off Type-I migration. This will be discussed later in this chapter.

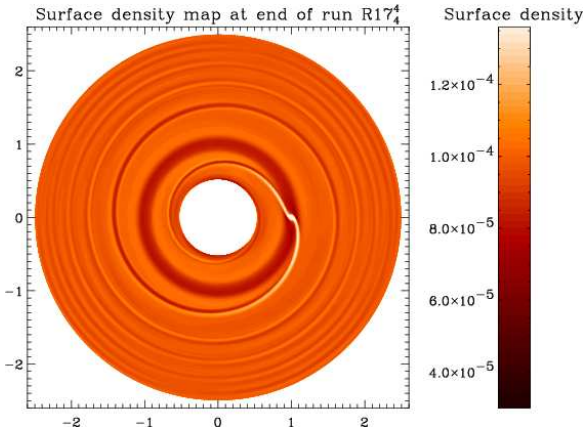

Figure 1.4: Numerical simulation of Type-I migration. The planet generates spiral waves at Lindblad resonances which interact with the planet. Masset (2002) A& A 387 605-623, DOI: 10.1051/0004-6361:20020240, Figure 2, reproduced with permission ©ESO.

A second source of angular momentum transfer in the Type-I migration regime is through the co-rotation torque, and is generated by gas that orbits very near to the planet. Near to the planet gas is perturbed from an orbit with larger orbital radii to lower orbital radii (and vice versa) as the planet orbits past. The crossing gas flows in horseshoe orbits around the planet, and during the libration at each end of the horseshoe angular momentum is transferred between the gas and planet (Paardekooper et al., 2010). If both ends of the horseshoe are perfectly symmetric then the angular momentum that is lost be the gas on one end of the orbit is returned on the other end. As a result the net angular momentum transfer is zero, and the co-rotation torque is said to be 'saturated'. For an 'un-saturated' co-rotation torque, the direction of the net angular momentum transfer is dependent on the temperature structure of the disk (Paardekooper et al., 2010).

More details of these torques are outlined in chapter 2.4, here we outline a particular important feature of the combined impact of both torques - planet trapping. Early studies of planet formation suggested that the typical migration rate of Type-I migration was smaller than the Oligarthic growth timescale (Ward, 1997; Masset et al., 2006). This suggested that a growing planet would tend to migrate into the host star before it had time to effectively grow. However because the direction of the un-saturated co-rotation torque was dependent on the power-law of the temperature profile, there could be regions of the disk where the direction of the net torque is reversed - hence trapping a planet at positions where the net torque vanishes. One such location is the heat transition mentioned before, where the primary source of heating and temperature profile changes. This was demonstrated by

Hasegawa & Pudritz (2010) in theoretical work, and numerically by Lyra et al. (2010). One can also demonstrate this effect using the work of Paardekooper et al. (2010) (see chapter 2). More recently, this trapping was demonstrated in more general numerical work by Coleman & Nelson (2016), who self-consistently compute the net torque on the planet in an evolving disk. In this thesis, we simply assume that the trapping occurs if the co-rotation torque is un-saturated, see chapter 2 for details.

When the planet is sufficiently large it perturbs its surrounding gas enough to open a large gap in the disk. When the gap is opened, Type-I migration is suppressed and is replaced by Type-II migration. The location of the gap evolves with the viscous evolution of the gas, as the planet acts as an intermediary to the transport of angular momentum through the disk. Generally Type-II migration is slower than un-trapped Type-I migration, evolving on timescales similar to the viscous timescale: $t_{mig} \sim t_{vis} = r^2/\nu$.

To open a gap, the gravitational tug of the planet must exceed the viscous torques of the gas which would try to fill the gap. Alternatively in an invisid disk the planet's gravitational influence must exceed the length scale of the gas pressure, otherwise the pressure of the gas will suppress gap formation. Combining these two effects leads to a critical mass of (Matsumura & Pudritz, 2006):

$$M_{gap} = M_* min\left[3h^3(r), \sqrt{40\alpha h^5(r)}\right], \tag{1.23}$$

where $h \equiv H/r$, the ratio of the gas scale height to orbital radius of the planet.

In principle, when the gap opens the accretion rate onto the planet should be affected. Because flow across the gap is reduced, Mordasini et al. (2015) sets the gas accretion rate of the gas after the gap opens to the global mass accretion rate of the disk ($\dot{M}$). This dramatically reduces the accretion rate of the gas (equation 1.22) to a timescale similar to the viscous timescale. Because both the accretion rate and migration rates are reduced to the viscous rate of the gas, a planet would evolve diagonally from low mass and large radius to high mass and small radius (ie. diagonally upward to the left of figure 1.3). There is some numerical work (for ex. Kley (1999); Lubow et al. (1999)) that suggests that the mass accretion rate of the planet can exceed the accretion rate of the disk with mass flow streaming through spiral density waves produced on the edge of the gap. As the planet grows, however, this mass accretion is eventually suppressed (Lissauer et al., 2009). To account for the eventual accretion shutoff, we parameterize the maximum mass of the planet as a scale factor of the gap opening mass $M_{max} = f_{max} M_{gap}$. In doing this we simplify a process which requires

full hydrodynamic simulations to fully understand, while maintaining the end result of post gap formation gas accretion.

1.3 Exoplanetary Atmospheres

The primary focus of this thesis is to connect the physical principles outlined in this chapter to predict the chemical composition of planetary atmospheres. There are few examples of complete theoretical prescriptions for predicting the chemical composition and structure of exoplanets. These include detailed chemical models paired with accretion disk models (ie. Helling et al. (2014); Eistrup et al. (2016)) as well as simple chemical models paired with detailed planet formation models (ie. Madhusudhan et al. (2016b); Mordasini et al. (2016)). These theoretical models have attempted to explain recent exoplanetary atmosphere observations which have begun to show variations in their chemical compositions.

1.3.1 Observational Constraints

New to our understanding of planetary properties are observations of emission and absorption spectra from the atmospheres of predominately Hot Jupiters. Approximately a dozen planets have been observed in the infrared using *Hubble* and *Spitzer*, and have confirmed the detection of water vapour (Kreidberg et al., 2014; MacDonald & Madhusudhan, 2017), as well as inferred the presence of other molecules such as CO_2, CO, and CH_4 (Lee et al., 2012, 2013; Miguel & Kaltenegger, 2014; Moses et al., 2013; Line et al., 2014b; Ranjan et al., 2014; Sing et al., 2015; Wakeford & Sing, 2015) in exoplanetary atmospheres. A primary observable in this study is the carbon-to-oxygen ratio (C/O) that was mentioned earlier. This ratio can be very difficult to constrain - our own Jupiter, for example, is missing an accurate estimation of the oxygen abundance in its atmosphere. This mystery is caused by the presence of ammonia and methane clouds in the upper atmosphere, obscuring of view of the deeper layers of the planet's atmosphere where most of its gas resides. A similar issue has been observed in exoplanetary systems (Wakeford & Sing, 2015) which complicates the observational studies by smoothing out emission spectra. Along with requiring advanced models of atmospheric structure, inferring the chemical structure of atmospheres is complicated by observational systematic error (Croll et al., 2015). For example, studies of emission spectroscopy often combine the transit depths of secondary eclipses at different wavelengths and at different epochs. Combining data from

different epochs assume that the emission of the planet does not change between different epochs, however the opposite is often true (Croll et al., 2015).

Of particular interest to our work is the work of Brewer et al. (2017) who measured C/O for a set of exoplanets and their host stars. Their observations suggest that on average: $\mathrm{C/O_{host\ star}} \lesssim \mathrm{C/O_{planet}} \lesssim 2 \times \mathrm{C/O_{host\ star}} < 1$. We assume that the host star's photosphere is reflective of the chemical composition of the disk, and that a Hot Jupiter is at least comprised of the same gas as the disk. The observation that $\mathrm{C/O_{planet}} > \mathrm{C/O_{host\ star}}$ suggests that Hot Jupiters might have accreted their gas outside the water ice line (where C/O is enhanced, see Figure 1.1), and then migrated to their current orbital radii.

1.3.2 Theoretical Considerations

The theoretical framework that we have developed combines a viscously evolving analytic disk model with a numeric dust physics code to compute the surface density and temperature of the gas and dust. In this evolving disk we compute the flux of UV and X-ray radiation with the Monte Carlo radiative transfer scheme RADMC3D. The distributions of the gas, dust, and radiation is used by a non-equilibrium astrochemistry code to compute the molecular abundance of the gas and ice throughout the whole lifetime of the disk. We combine this evolving astrochemical disk with the standard core (planetesimal) accretion model to track the chemical abundance of the gas that is accreted by the forming proto-planet throughout its formation period. We confront our model with observed molecular abundances that are inferred through retrieval techniques of Hot Jupiter atmospheres. This comparison assumes that no chemical or physical evolution has occurred within the atmosphere after it has formed. It is generally accepted that equilibrium chemistry will shift the molecular abundance of the atmospheric gas depending on its temperature and pressure. Meanwhile, elemental ratios, like the carbon-to-oxygen ratio, are insensitive to chemical processes, as long as molecular species are not removed from the gas phase. Because of this insensitivity, we also analyze the elemental ratios that are produced by our predicted atmospheres.

The most similar theoretical framework to our work was developed by Mordasini et al. (2016) who combined a comprehensive disk and planet formation model, a simple disk chemical model, and a planetary atmospheric model to produced synthetic spectra which was compared to observations. They generally conclude that Hot Jupiters tend to be oxygen-rich (ie. $\mathrm{C/O} < 1$), and that even in carbon rich disks, carbon rich planets are rare. As will be seen, our model generally agrees with their

conclusion, however our model takes this a step further - concluding that $C/O_{planet} = C/O_{host\ star}$. Mordasini et al. (2016) call their theoretical construct a 'chain' model, where every physical model is connected together like links in a chain. Moving down the chain each link influences the next, while no link may impact the links above them. In this way the model can be easily computed by ignoring complicated interactions like the link between the radial structure of the dust and the ionization structure of the gas - this is outlined in chapter 3.

Along with studying the resulting atmospheric C/O, being armed with a powerful astrochemical code allows for the analysis of other elemental ratios like the carbon-to-nitrogen ratio (C/N). It remains to be seen whether this ratio can be determined observationally. Important for modeling the structure of planetary atmospheres, a complicated chemical model allows for the determination of the molecular abundances of H_2O, CO, CO_2, CH_4, NH_3, N_2, among others. These abundances will depend not only on *where* the planet accretes its gas (as has been discussed), but also *when* the gas is accreted. As the disk ages, the temperature of the gas cools and the surface density of the gas and dust is reduced, and hence the chemical structure of the gas will evolve. This evolution could be imprinted onto the forming planet, producing observable features in exoplanetary atmospheres. This will be further discussed throughout the later chapters.

1.3.3 Outline of the Following Chapters

In the next three chapters we outline our theoretical framework, which was presented in three published papers. This work combines sophisticated astrochemical methods with planet formation models to predict the chemical composition of exoplanetary atmospheres - a first of its kind. The goal of this work is to understand what range of chemical abundances should be expected from observations, and to link observed abundances to a planet's formation history. As will be discussed, we have found a difference in the abundance of nitrogen carriers in the atmospheres of planets that accreted gas early in the disk's life when compared to planets that accreted gas later.

Additionally we have investigated the impact of including the radial drift of dust grains on the chemical processes in protoplanetary disks. We have found that the redistribution of dust grains by radial drift reduces the disk's opacity to ionizing radiation - leading to higher electron fraction in the disk gas when compared to a simple dust model (constant gas-to-dust ratio). The distribution of free electrons impacts the generation of turbulence through the magnetorotational instability (see chapter 2.4.1).

The author's contribution to the three following published papers was in leading the development of the software needed to combine the models that have been discussed in this chapter, and will be discussed in the following chapters. The author was also the primary writer and corresponding author of each of these papers.

In chapter 2 we outline in detail our fiducial model including the disk model, core accretion, planetary migration, and astrochemical model. We outline our fiducial model parameters, and report the first chemical results for the atmospheres of the two Hot Jupiters that form in the disk. Generally we find that both planets accrete their gas within the water ice line which results in C/O $= \mathrm{C/O_{disk}}$ for both planets. In this chapter we used a dust model with a constant gas-to-dust ratio - which is a standard approach in accretion disk modelling (for ex. D'Alessio et al. (2006); Fogel et al. (2011); Semenov (2011)), but argued that the dust model was over simplified. It has been well constrained by recent observations that the gas and dust are not distributed the same way that a constant gas-to-dust ratio implies.

In chapter 3 we introduce a new dust model which we incorporated into our theoretical framework. We outline the dust model in detail, and demonstrate the primary difference between the new dust model and the simple 'constant gas-to-dust' model which was used in chapter 2. In this new model the size distribution of the dust grains is determined by the coagulation and fragmentation of dust grains, while its radial distribution is dependent on the radial drift of the dust grains. Because in the new dust model the surface density of the dust decreases faster than in the constant gas-to-dust model, the disk becomes more ionized and the dead zone shrinks faster. This faster shrinking leads to different formation histories of the planets in the fiducial model.

In chapter 4 we compute the chemical evolution of the disk model presented in chapter 3 and, for the first time, present the chemical evolution of a viscously evolving gas disk with coupled dust physics. To our knowledge, this has never been done before. We use this evolving astrochemical disk to predict the chemical composition of planets formed in that model. Additionally we present two disk models with different initial disk masses to study the variation in final bulk chemical composition of the planets formed in these models. Generally we find that C/O does not vary between the planets because the planet traps where each planet formed converge as the disk ages. We do find a variation in the primary nitrogen gas carrier depending on *when* and *where* the planet forms, while the carbon-to-nitrogen (C/N) does not vary strongly.

In chapter 5 we confront our model with a real system. HL Tau is a very well study protoplan-

etary system, most recently with the Atacama Large Millimeter Array (ALMA). We choose a set of disk parameters which reproduce observed quantities in the HL Tau system, and compute the astrochemistry and planet formation within the system.

Chapter 2

Composition of Early Planetary Atmospheres I: Connecting Disk Astrochemistry to the Formation of Planetary Atmospheres

What follows has been published in Monthly Notices of the Royal Astronomical Society (MNRAS). See: Cridland, Pudritz & Alessi 2016. MNRAS **461**: 3274.

Abstract

We present a model of the early chemical composition and elemental abundances of planetary atmospheres based on the cumulative gaseous chemical species that are accreted onto planets forming by core accretion from evolving protoplanetary disks. The astrochemistry of the host disk is computed using an ionization driven, non-equilibrium chemistry network within viscously evolving disk models. We accrete gas giant planets whose orbital evolution is controlled by planet traps using the standard

core accretion model and track the chemical composition of the material that is accreted onto the protoplanet. We choose a fiducial disk model and evolve planets in 3 traps - water ice line, dead zone and heat transition. For a disk with a lifetime of 4.1 Myr we produce two Hot Jupiters (M $= 1.43, 2.67\,\mathrm{M_{Jupiter}}$, r $= 0.15, 0.11$ AU) in the heat transition and ice line trap and one failed core (M $= 0.003\,\mathrm{M_{Jupiter}}$, r $= 3.7$ AU) in the dead zone. These planets are found with mixing ratios for CO and H_2O of 1.99×10^{-4}, 5.0×10^{-4} respectively for both Hot Jupiters. Additionally for these planets we find CO_2 and CH_4, with mixing ratios of $1.8 \times 10^{-6} \rightarrow 9.8 \times 10^{-10}$ and $1.1 \times 10^{-8} \rightarrow 2.3 \times 10^{-10}$ respectively. These ranges correspond well with the mixing ratio ranges that have been inferred through the detection of emission spectra from Hot Jupiters by multiple authors. We compute a carbon-to-oxygen ratio of 0.227 for the ice line planet and 0.279 for the heat transition planet. These planets accreted their gas inside the ice line, hence the sub-solar C/O.

2.1 Introduction

Understanding the chemical composition and structure of exoplanetary atmospheres is now feasible with the advent of large surveys from the Hubble space telescope and Lowell observatory (TrES - Transatlantic Exoplanet Survey, Alonso et al. (2004)) along with planned missions like the Transiting Exoplanetary Survey Satellite (TESS), Extremely Large Telescope (ELT) follow up to PLATO, and the James Webb Space Telescope (JWST). A number of authors (Madhusudhan & Seager (2009, 2010), Lee et al. (2012, 2013), Venot et al. (2014), Line et al. (2011, 2014a), Stevenson et al. (2010), Miguel & Kaltenegger (2014), Van Grootel et al. (2014),Sing et al. (2015), Kreidberg et al. (2014), Brogi et al. (2016),Kataria et al. (2016),Oklopčić et al. (2016)) have begun retrieving chemical abundance data from the spectra of directly observed, and transiting exoplanets. These efforts have detected the chemical signatures of about a dozen chemical species including H_2O, CO, CO_2, CH_4, HCN, Na and Mg for about a dozen planets.

By an early atmopshere we mean a young system ($t_{age} \lesssim 10$ Myr) that has not seen enough dynamical and chemical evolution to alter the chemical composition of the gas that it accretes from its natal protoplanetary disk. Computing the early chemical composition of an exoplanetary atmosphere requires the combination of three areas of study: accretion disk physics, astrochemistry, and planet formation physics. The work presented here combines these studies in a series of steps. The local chemical composition of a disk at any position or time is indicated by non-equilibrium

chemical processes in the viscously evolving disk. Planetary cores migrating through their host disk will accrete materials of different chemical composition as they move. The final mix of materials accreted onto the planet will therefore depend on the astrochemistry of the evolving disk, and the details of its accretion history during its formation.

In past works, the astrochemistry of accretion disks has been studied by applying numerical, 1+1D photo-chemical codes as seen in Bergin et al. (2003), Fogel et al. (2011) and Cleeves et al. (2014) and 2D radiative thermo-chemical codes (ie. ProDiMo, see Woitke et al. (2009)) in the context of static, viscous and radiatively heated accretion disks (eg. D'Alessio et al. (1998, 1999), Lynden-Bell & Pringle (1974) and Chiang & Goldreich (1997)). For a comprehensive review of this topic see Henning & Semenov (2013). Population synthesis models as given in Ida & Lin (2004) and Hasegawa & Pudritz (2013) have been used to study the physics of planet formation. These population synthesis models rely on the core accretion model (Kokubo & Ida, 2002) which describes the rate of formation of a protoplanet out of a sea of planetessimals ranging between 1-10 km in size.

It is the goal of this paper to combine these streams of research to compute the chemical composition of the gas that is delivered to planets. This provides the initial conditions for building models of planet and atmospheric structure that do not depend on the assumption of solar abundances. Indeed we will show that there are significant deviations from solar abundances depending on *where* and *when* the planet forms in the disk.

For example the carbon and oxygen content of an exoplanetary atmosphere has been compared to the composition of gas at the location where the protoplanet accretes its gas (see for example Madhusudhan et al. (2014a)). To first order, the chemical content of the atmosphere is set by the location where the planet accretes its gas relative to the condensation fronts of H_2O, CO_2 and CO. At larger radii than the condensation front a particular chemical species resides in the solid (frozen) phase, while at smaller radii it is a gas. As shown in Madhusudhan et al. (2014a), tracking the mass and orbital evolution of the accreting planet allows for the determination of the chemical content of planets at different final semi-major axes.

A more complete analysis of the connection between disk astrochemistry and planetary atmospheres was done by Helling et al. (2014). In this work the chemical structure of the material available for planet formation was computed using the ProDiMo code (Woitke et al., 2009) in a Lynden-Bell & Pringle (1974) disk model. Helling et al. (2014) showed that after a short relaxation time ($<< 10^3$ yr) the gas chemistry reaches an equilibrium state at the midplane of the disk, where the time evolu-

tion becomes dominated by cosmic ray ionization driven reactions. This time evolution is traced by the elemental ratio of carbon to oxygen (C/O) in the gas, which increases with time in their model. Their connection to planetary atmospheres was made by studying the formation of clouds. Cloud formation is sensitive to the presence of silicate grains in the atmosphere that acts as a seed for clouds. Helling et al. (2014) demonstrated that oxygen poor planets, with C/O ~ 1, formed clouds less efficiently than oxygen rich planets because of the lack of oxygen to form silicates.

Absent from previous works is the important fact that material is accreted through the disks and onto the host star due to torques caused by disk winds and viscosity, and is later photoevaporated by FUV photons. This accretion history changes the surface density and global temperature structure of the disk as it ages, thereby changing the location of the condensation fronts while the planets evolve. This evolution of disk accretion is also a driver for the evolution of the chemistry within disk. Finally, photoevaporation ultimately sets the lifetime of disks, which determines the planet's final mass and ends their orbital evolution by purely disk-planet interactions. Our method of modeling these important physical processes will be discussed below.

The lifetime of a disk is set by the strength of photoevaporation from the host star, and is between $3-4$ Myr on average (eg. Hernández et al. (2007), Haisch et al. (2001), Strom et al. (1989) and Wilking et al. (1989)). The source of the photoevaporating UV rays is the hot accretion shock ($\sim$ 9000 K) produced by material accreted onto the star along magnetic field lines (Gorti et al., 2015). The accretion shock also acts as a point source of X-rays which are partially responsible for setting the ionization structure of the disk. The ionization structure controls the coupling between the magnetic field and the gas disk (an important feature of MRI driven turbulence, see below) as well as the production of ions. These ions are an important part of gas phase chemistry because of their low activation barrier during reactions with neutral molecules.

Apart from these factors that impact isolated disks, several external agents can change how the structure of the disk evolves when the young system is in a cluster environment. These include dynamical interactions between stars that could truncate disks, and the influence of the cluster UV and X-ray background arising from O and B stars in the cluster. However, observational studies have shown that the proximity to the most massive stars in a cluster does not affect the survivability of disks (Richert et al., 2015). Furthermore dynamical interactions with other cluster stars do not scatter planets with orbital separations less than $\sim$ 200 AU from their host star (Zheng et al., 2015). Most observed planets have orbital separations much less than $\sim$ 200 AU (see Figure 2.1), so we

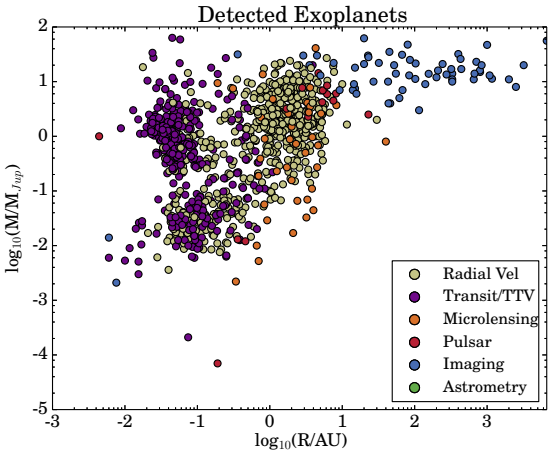

Figure 2.1: All available exoplanetary data accessed from http://exoplanet.eu/catalog/ on November 23rd, 2015. The colour of the scatter points show the detection method used to determine the mass of the planet.

choose to ignore the impact of these external effects.

Gas chemistry in the disk is dominated by ion-molecule, photodissociation and dissociative recombination reactions. These reactions are supplemented by neutral-neutral molecular reactions, however they are limited by an activation barrier and generally have reaction rates that are two orders of magnitude smaller than the above reactions (Tielens, 2005). On the surface of dust grains, the reaction rates of these neutral-neutral reactions are increased because the collisional probability of two gas molecules is higher than in free space. As a result, grain surface reactions are very important for the production of more complicated gas species like formaldehyde (H_2CO) which is formed through the proton capture of frozen carbon monoxide. As discussed above there is a stellar source for the high energy photons responsible for the photodissociation and ionizing reactions in the gas phase, however these photons may not reach deep into the interior of the disk. A second source of photodissociating photons can be produced from the radiative relaxation of excited H_2 molecules. The source of these excited molecules is from primary electrons produced by cosmic rays (Tielens, 2005).

Astrochemical models of static protoplanetary disks are well developed (Woitke et al., 2009; Semenov & Wiebe, 2011; Fogel et al., 2011; Henning & Semenov, 2013; Thi et al., 2013; Walsh et al., 2013; Cleeves et al., 2014). These combine passive models (no time evolution) of 2D protoplanetary disks with advanced methods of high energy radiative transfer (eg. Bethell & Bergin (2011b)). These models are combined with a large set of gas phase reactions that number over 6000 (eg. the

destruction of N_2H+ by carbon monoxide gas: Equation 2.1) with grain surface reactions (eg. the formation of water by proton capture of frozen oxygen: Equation 2.2) and photodissociative reactions (eg. Equation 2.3) to produce a complete snapshot of the chemical structure in the disk.

$$N_2H^+ + CO \rightarrow HCO^+ + N_2 \tag{2.1}$$

$$H + H + O(gr) \rightarrow H_2O(gr) \quad (net) \tag{2.2}$$

$$HCO + \gamma \rightarrow H + CO \tag{2.3}$$

A significant range of molecules has been detected by large sub-millimeter arrays such as ALMA, IRAM and SMA. At the time of writing, emission lines from H_2O, CO, HCN, NH_3, C_2H_2, CO_2 and OH (Pontoppidan et al., 2014) have been detected, including many that are important to the origins of life (eg. Glycolaldehyde (Jørgensen et al., 2012)). Even with this wealth of data the full content of carbon and nitrogen based molecules in accretion disks has not been fully determined (Pontoppidan et al., 2014).

We now turn to the second aspect of the problem: accretion and migration processes involved in planet formation. We adopt the core accretion picture of planet formation within the inner 100 AU of protoplanetary disks, which has broad observational support (Ida & Lin, 2004; Mordasini et al., 2012; Andrews et al., 2013; Ida et al., 2013; Hasegawa & Pudritz, 2013; Dittkrist et al., 2014). This model is appropriate for the majority of gas giant planets which have been observed within a few AU, and the new population of planets known as Hot Jupiters that orbit at semi-major axes less than a tenth of an AU (see Figure 2.1).

Successful methods of finding exoplanets include radial velocity, transit methods and direct imaging. The majority of planets have been reported in the last five years (Batalha et al., 2013; Rowe et al., 2014). Inferring the chemical abundance of an exoplanetary atmosphere requires the detection of the transmission or emission spectra from transiting or nearly transiting exoplanets (eg Lee et al. (2012, 2013); Snellen et al. (2015)) or direct measurement of the emission spectra for a direct imaging planet (Konopacky et al., 2014). The most abundant molecules found so far are: H_2O, CO, CO_2 and CH_4, along with some trace detections of Na and K (Sing et al., 2015; Wilson et al., 2015; Wyttenbach et al., 2015; Montalto et al., 2015). There remains a wide range of uncertainty in these detections, mostly caused by systematic errors in observational techniques (Croll et al., 2015). Fur-

thermore there are insensitivities in the resulting features of observed emission spectra from chemical atmospheric models that vary chemical element ratios (like C/O, see Moses et al. (2013)).

Moreover, chemistry impacts the physical system through the dependence of the planetary atmosphere's total opacity at a given wavelength to the chemical abundance of the gas (Seager & Deming, 2010). The opacity of the gas sets its temperature and temperature gradient, thereby affecting the way that energy can be transported through the atmosphere. When the opacity is very high, energy will be transferred through convection because the radiative temperature gradient in the planetary atmosphere becomes very large. Having a good estimate of the gas opacity is dependent on having an accurate account of present chemical species in the gas.

Our astrochemistry model follows the same methods used in Fogel et al. (2011) and Cleeves et al. (2014), however we follow the evolution of the chemical structure by computing the physical and chemical state of the disk over 300 snapshots extending over 4 million years.

The paper is organized as follows: our disk model and chemical model are outlined in §2 and §3 respectively. The migration and accretion model is discussed in §4. We compute and report initial chemical compositions of early atmospheres in §5. We compare our results to observations and discuss their implications in §6. Concluding remarks are found in §7.

2.2 Disk Model

Computing the astrochemistry in an accretion disk requires the temperature and surface density structure, as well as the local distribution of ionizing photons. Accretion disks are heated by a combination of viscosity in the inner regions (Lynden-Bell & Pringle, 1974) and radiative heating (Chiang & Goldreich, 1997). Both of these heating sources produce power laws that describe the temperature and surface density profile, with exponents that depend on which heating source is dominating. It has been demonstrated through numerical work that the true midplane temperature profile can be described by a double power law. The inner region (within the heat transition point) mimics the temperature profile caused by a viscously heated disk. The outer region of the disk mimics the profile caused by direct illumination (D'Alessio et al., 1998, 1999). From this numerical picture it has become clear that a purely viscous disk would be too cold in the outer regions, affecting the distribution of important ices like CO and NH_3. A purely radiative disk on the other hand would be too cool at smaller radii, affecting the distribution of important gases like H_2O and CO_2.

In our work, we wish to incorporate the double power law form of the temperature and surface density profiles observed in numerical simulations. However, a full numerical treatment of the disk is too computationally expensive when the disk properties must be traced over millions of years of evolution. Fortunately, a model introduced by Chambers (2009) reproduces the disk structure caused by two separate heating sources while remaining fully analytic, allowing for the density and temperature structure to be traced over the whole life of the disk.

The temperature and surface density is described by a power law,

$$T\left(r\right) \propto r^{-\beta}; \quad \Sigma\left(r\right) \propto r^{-s}, \tag{2.4}$$

where the exponents β and s are given by the source of heating in the disk. These exponents are determined by solving the diffusion equation for a viscously evolving disk (Lynden-Bell & Pringle, 1974),

$$\frac{\partial \Sigma}{\partial t} = \frac{3}{r}\frac{\partial}{\partial t}\left[r^{1/2}\frac{\partial}{\partial t}\left(r^{1/2}\nu\Sigma\right)\right], \tag{2.5}$$

based on the previous work of Stepinski (1998) which included heating from both viscous evolution and direct irradiation. The Chambers (2009) solution is self-similar, with the variable $r/s(t)$ where $s(t)$ is the time-dependent size of the disk. This approach computes the temporal evolution of the temperature and surface density profiles simultaneously, and relies on how the viscosity of the disk varies, as a power-law in radius (Lynden-Bell & Pringle, 1974).

Angular momentum transport that enables disk accretion can be driven radially by turbulent stress, or vertically due to the MHD torque exerted by a magnetized disk wind (eg. see Pudritz et al. (2007); Bai & Stone (2013); Gressel et al. (2015)). We assume that both the effective viscosity due to either turbulent or wind stress ν can be modeled following the standard α-disk model (Shakura & Sunyaev, 1973)

$$\nu = \alpha c_s H, \tag{2.6}$$

where c_s is the sound speed of the gas and H is the pressure scale height. In Equation 2.6, the α parameter for turbulent transport is generally defined as the ratio between the turbulent and thermal pressures (Shakura & Sunyaev, 1973). While in the case of angular momentum loss to the disk by

disk winds, it is the ratio between the vertically directed component of the Maxwell stress and the thermal pressure. Generally speaking the disk's effective α is due to a combination of both of these transport mechanisms: $\alpha \equiv \alpha_{turb} + \alpha_{wind}$.

In this work we assume that the source of the turbulence is caused by the operation of a magnetorotational instability (MRI) (Balbus & Hawley, 1991a). The strength of the MRI driven turbulence (magnitude of α_{turb}) depends on the level of ionization in the disk. It is characterized by the Ohmic Elsasser number, which is the ratio of the dissipation timescale to the growth timescale of the most unstable mode:

$$\Lambda_O \equiv \frac{\tau_{diss}}{\tau_{grow}} = \frac{v_{A,z}^2}{\eta_O \Omega}. \tag{2.7}$$

In this expression $v_{A,z} \equiv B_z/\sqrt{4\pi\rho}$ is the Alfvén speed in the z-direction, B_z is the local magnetic field in the z-direction, ρ is the gas density and Ω is the orbital frequency (Bai & Stone, 2013; Gressel et al., 2015). When $\Lambda_0 > \Lambda_{0,crit} \equiv 1$ (Simon et al., 2013) we assume that that region of the disk is turbulently active, with $\alpha_{turb} = 10^{-3}$, while in the opposite case we assume that the disk is turbulently 'dead' with $\alpha_{turb} = 10^{-5}$. The Ohmic resistivity,

$$\eta_O = \frac{234\ T^{1/2}}{x_e}\ cm^2 s^{-1}, \tag{2.8}$$

depends on the electron fraction (x_e) and temperature structure in the disk (Kunz & Balbus, 2004).

The Ohmic resistivity will vary throughout the disk due to the changing temperature and ionization structure of the gas. This leads to changes in the activity of the MRI. Our research differs from previous works (see Matsumura et al. (2009) and Hasegawa & Pudritz (2013)), where a semi-analytic approach was taken to compute the electron fraction. Instead, we compute the electron fraction of the disk directly with our photochemical code for a given temperature and surface density profile to determine the Ohmic Elsasser number. At the midplane of the disk, MRI-inactive regions will be present where there is low ionization. This has implications on the global angular momentum transport and ultimately on the mass accretion through the disk.

It has been suggested that angular momentum transport can be maintained through the dead zone by other means such as magnetocentrifugally driven winds (Pudritz & Norman, 1983) or layered accretion through regions higher in the disk's atmosphere (Lesniak & Desch, 2011). In both cases,

the mass is accreted through higher regions of the disk where densities are lower and more susceptible to angular momentum transport by MRI driven turbulence or winds (Gressel et al., 2015; Gressel & Pessah, 2015). Because the mass accretion rate through dead zones can be maintained by these mechanisms, we assume that the mass accretion rate $\dot{M}$ remains constant in radius through the disk. As a mathematical constraint, we assume that the disk effective viscosity parameter $\alpha \equiv \alpha_{turb}+\alpha_{wind}$ also remains constant in both space and time.

In light of the idea of a turbulently dead zone, we will treat the chemical structure of the disk as a passive feature of our disk model. Any impact on the physical structure from the chemical evolution (eg. opacity, α or density jumps at condensation fronts) is thus ignored. The inclusion of the effect of the chemistry can be achieved through an iterative process as was done for brown dwarf and hot Jupiter atmospheres (Marley et al., 1996; Fortney et al., 2005). However this iterative process is computationally expensive and requires multiple calculations of the temperature and chemical structure in the disk, with no guarantee of a converging solution.

As mass is accreted onto the host star due to angular momentum transport by viscous stress, the disk must spread out, which forces a reduction in mass accretion rate. In the Chambers (2009) model, the mass accretion rate decreases as a power law in time. It has been shown in population synthesis models however (Hasegawa & Pudritz, 2013) that a dissipative model of the mass accretion rate more accurately reproduces the population of exoplanets that have been observed. The photoevaporation of disks results in an exponential decay of the mass accretion rate, so that:

$$\dot{M} \equiv \dot{M}_{vis}(t) \rightarrow \dot{M} \equiv \dot{M}_{vis}(t)e^{-(t-t_{in})/t_{dep}}, \tag{2.9}$$

where $\dot{M}_{vis}$ is the equilibrium accretion rate determined by the solution to the viscous Equation 2.5, t_{in} is the starting time of the simulation (0.1 Myr), and t_{dep} is an estimate of the depletion time of the dissipation. The standard source of the dissipation is assumed to be the photoevaporation (Hasegawa & Pudritz, 2013) of the disk from the UV or X-ray emission of the host star. The impact of photoevaporation on disk structure has been studied in great detail, and impacts both the overall surface density structure and lifetime of accretion disks around young stars (Alexander et al., 2014). It has been shown (Gorti et al., 2015) that disk dispersal due to photoevaporation happens very quickly, with time scales on the order of 10^4 years. Because of this small timescale we treat the disk lifetime as a free parameter, constrained by observations, and assume that at $t = t_{life}$ the disk is

abruptly cleared. The full form of equation 2.9 is

$$\dot{M} \equiv \begin{cases} \dot{M}_{vis}(t) e^{-(t-t_{in})/t_{dep}} & t < t_{life} \\ 0 & t \geq t_{life}. \end{cases} \tag{2.10}$$

Any planets that are forming in the disk at t_{life} are frozen in orbital radius when the disk is cleared, and we assume no further orbital or mass evolution takes place due to gas dynamical processes. The values used for t_{in}, t_{dep} and t_{life} are found in Table 5.2 below.

2.2.1 Heating Sources

The sources of heating determine the surface density and temperature distributions, as well as how the distributions depend on the evolution of the mass accretion rate with time. Ultimately, the heating is also strongly connected to the chemical makeup of the disk, through the temperature dependence of most chemical reactions.

Viscous Heating

In the viscous regime, heating results from the viscous stress on the disk. The resulting effective temperature, T_{eff}, describes the flux of radiation emitted by a ring of radius R caused by the viscous accretion of material through the ring, assuming the material acts as a blackbody. The effective temperature is given by (Chambers, 2009),

$$2\sigma T_{eff}^4 = \frac{9\nu\Sigma\Omega^2}{4}. \tag{2.11}$$

The temperature at the midplane is then:

$$T^4 = \frac{3\tau}{4} T_{eff}^4, \tag{2.12}$$

where the optical depth is defined by:

$$\tau = \frac{\kappa_0 \Sigma}{2}, \tag{2.13}$$

where $\kappa_0 = 3\ cm^2/g$ is an assumed constant opacity.

With that, we express the midplane temperature as

$$\left(\frac{T}{T_{vis}}\right)^4 = \left(\frac{\nu}{\nu_0}\right)\left(\frac{\Sigma}{\Sigma_0}\right)^2\left(\frac{\Omega}{\Omega_0}\right)^2. \tag{2.14}$$

All subscripts of 0 denote the value of all variables at the outer edge of the disk at $t = 0$, denoted by s_0 and

$$T_{vis}^4 = \left(\frac{27\kappa_0}{64\sigma}\right)\nu_0\Sigma_0^2\Omega_0^2. \tag{2.15}$$

It has been shown that accreting disks enter into a quasi-steady state (Papaloizou & Terquem, 1999) with a constant (in radius) mass accretion rate of $\dot{M} = 3\pi\nu\Sigma$ (Alibert et al., 2005; Chambers, 2009). In more recent simulations (see Baillié & Charnoz (2014) and Baillié et al. (2015)), this result has been confirmed at later disk lifetimes ($t > 10^5$ yr) for radii less than a few tens of AU. Following these previous works we will assume that the mass accretion rate is constant in radius over the whole disk, with the value of the steady state solution from above. Due to angular momentum conservation one would require that

$$\begin{aligned} \dot{M}_{vis} &= 3\pi\nu\Sigma && r < r_{turn} \\ \dot{M}_{vis} &= -3\pi\nu\Sigma && r > r_{turn}, \end{aligned} \tag{2.16}$$

where $\dot{M}_{vis}$ is the same mass accretion rate shown in Equation 2.9 and 2.10, and r_{turn} is the hypothetical turning point of the gas accretion direction. For visual simplicity we drop the subscript from the mass accretion rate in Equation 2.16 and assume in the final expressions that the mass accretion rate is determined by both viscous (Eq. 2.16) and evaporative (Eq. 2.10) sources. Viscous heating only depends on the magnitude of the accretion rate, not the direction of accretion. In what follows, only the magnitude of $\dot{M}$ will be important and not its sign. Combining equation 2.14 with the mass accretion rate results in the radial dependence of the surface density:

$$\Sigma = \Sigma_{vis}\left(\frac{\dot{M}}{\dot{M}_0}\right)^{3/5}\left(\frac{r}{s_0}\right)^{-3/5}, \tag{2.17}$$

this results in the temperature profile:

$$T = T_0 \left(\frac{\dot{M}}{\dot{M}_0}\right)^{2/5} \left(\frac{r}{s_0}\right)^{-9/10}, \tag{2.18}$$

where the initial mass accretion rate $\dot{M}_0 = 3\pi\nu_0\Sigma_0$ is set by the choice of initial surface density Σ_0 at the edge of the disk, which for a purely viscous disk is exactly $\Sigma_0 = \Sigma_{vis}$. This density can be constrained by computing the total mass,

$$M \equiv 2\pi \int_0^s r\Sigma dr, \tag{2.19}$$

at the initial time. Substituting in Equation 2.17 we find $\Sigma_{vis} = 7M_0/10\pi s_0^2$, where M_0 is the initial mass of the disk. Using conservation of angular momentum one finds (see Chambers (2009)) that the size of the disk scales with the total mass as:

$$\left(\frac{s}{s_0}\right) = \left(\frac{M}{M_0}\right)^{-2}. \tag{2.20}$$

The spread in the radial direction is primarily due to the viscous evolution of the fluid rather than other angular momentum transport mechanisms like winds, which direct angular momentum vertically. So we assume that the spreading rate will only depend on the mass accretion rate due to viscous evolution. In combining eqs. 2.16, 2.17, 2.19 and 2.20 we find:

$$\frac{dM}{dt} \equiv -\dot{M}_{vis} = -\dot{M}_0 \left(\frac{M}{M_0}\right)^{19/3}. \tag{2.21}$$

Radiative Heating

When the optical depth in the disk has dropped sufficiently, its heating becomes dominated by the direct irradiation of the host star. Chiang & Goldreich (1997) first studied the temperature structure of a passive disk in thermal equilibrium with the irradiation of its host star. Their results were then used by Chambers (2009) to compute the density structure of his disk in the radiatively heated regime. The transition between these two regimes is referred to as the heat transition and is defined as the point where the temperatures derived by both heating sources is equal (see Chambers (2009), Equation 38). This transition point slowly moves inward as the disk ages and the accretion rate drops. As the accretion rate drops, the viscous heating rate is reduced and so the viscously heated

region of the disk cools with time, until the disk is exclusively heated through direct irradiation.

We have made a small modification to the formalism of Chambers (2009) who assumed that the disk acted as a perfect blackbody in thermal equilibrium with the host star's radiation. As is well known, the perfect blackbody model does not accurately reproduce the SEDs of young stars, whereas a superheated upper atmosphere that heats the midplane (Chiang & Goldreich, 1997) more accurately reproduces SEDs. This more complicated model reduces the temperature at the midplane by a factor of $2^{1/4}$ when compared to the full blackbody temperature structure.

From the superheated atmosphere model for radiatively heated disks (Chiang & Goldreich, 1997), the midplane temperature is given by:

$$T = \left(\frac{\theta}{4}\right)^{1/4} \left(\frac{R_*}{r}\right)^{1/2} T_*, \tag{2.22}$$

where T_* and R_* are the stellar temperature and radius respectively. The grazing angle θ of the light on the disk is dominated by the flaring of the disk, which has the form (Chambers, 2009):

$$\theta = r\frac{d}{dr}\left(\frac{H_{ph}}{r}\right), \tag{2.23}$$

where H_{ph} is the height of the disk where the gas optical depth from the host star reaches one. As in Chambers (2009) and Chiang & Goldreich (1997) we assume that the disk is roughly vertically isothermal which results in a disk height of (Chiang & Goldreich, 1997),

$$\frac{H_{ph}}{r} \simeq 4\left(\frac{T_*}{T_c}\right)^{4/7} \left(\frac{r}{R_*}\right)^{2/7}, \tag{2.24}$$

where T_c is a constant with units of Kelvins (see Chambers (2009), his Equation 30). Combining eqs. 2.22, 2.23, 2.24 the resulting temperature profile is:

$$\left(\frac{T}{T_{rad}}\right) = \left(\frac{r}{s_0}\right)^{-3/7}, \tag{2.25}$$

where

$$T_{rad} = \left(\frac{2}{7}\right)^{1/4} \left(\frac{T_*}{T_c}\right)^{1/7} \left(\frac{R_*}{s_0}\right)^{3/7} T_*. \tag{2.26}$$

An important distinction between the viscously heated regime and the radiatively heated regime is the lack of $\dot{M}$ dependence in the latter. In the viscous regime the temperature of the disk cools as it ages (mass accretion rate decreases), however the radiative regime is passive. and the temperature does not change with time. As the mass accretion rate drops and the viscous regime cools the heat transition point moves inwards as radiative heating becomes more dominant. The density profile in the radiative regime has the form:

$$\Sigma = \Sigma_{rad} \left(\frac{\dot{M}}{\dot{M}_0} \right) \left(\frac{r}{s_0} \right)^{-15/14}, \tag{2.27}$$

where Σ_{rad} is the surface density of the disk at the edge of the radiative region. We assume that the host star does not evolve in time as the disk accretes. This is a fair assumption for G-type stars but would need to be taken into account for M-type stars which spend up to an order of magnitude longer in their pre-main sequence stage of evolution (Hayashi, 1961). The evolution of the disk mass due to viscous accretion is modified when a radiative region is present. Combining eqs. 2.16, 2.27, 2.19 and 2.20 we find:

$$\frac{dM}{dt} \equiv -\dot{M} = -\dot{M}_1 \left(\frac{M}{M_1} \right)^{20/7}, \tag{2.28}$$

where $\dot{M}_1$ is the mass accretion rate when the radiative regime appears and M_1 is the disk mass at that time.

For the purpose of computing the temperature and density profiles at a given time we use the temperature profile (Equation 2.18 or 2.25) that gives the higher temperature for a given radius, and the corresponding density profile (Equation 2.17 or 2.27). The mass accretion rate in Equation 2.17 is computed by substituting the mass accretion rate solution of Equation 2.21 if no radiatively heated regime exists. Otherwise 2.28 is substituted into Equation 2.10 and is used to evolve the mass accretion rate. The disk model is initialized at a time of 0.1 Myr with initial disk mass M_0 and size s_0. For further details see Chambers (2009).

Table 5.2 shows the fiducial values for our disk model parameters, including the luminosity normalization used in the radiative transfer of X-rays.

Table 2.1: Fiducial disk model parameters

$M_{disk}(t=0)$	0.1 $M_\odot$
$s_{disk}(t=0)$	66 AU
M_{star}	1.0 $M_\odot$
R_{star}	3.0 $R_\odot$
T_{star}	4200 K
α	0.001
t_{in}	0.1 Myr
t_{dep}	1 Myr
t_{life}	4.10 Myr
L_{xray}	10^{30} erg

Note: t_{in}, t_{dep} and t_{life} are from Equation 2.10. L_{xray} is the normalizing luminosity of the x-ray source in the system.

2.3 Disk Chemistry

The chemistry in the disk is computed with a non-equilibrium, coupled, differential equation solver as seen in Bergin et al. (2003), Fogel et al. (2011) and Cleeves et al. (2014) and is based on the gas-grain chemical code: ALCHEMIC (Semenov et al., 2010). Generally, the abundance of a given chemical species $n(i)$ will evolve as (Fogel et al., 2011):

$$\frac{dn(i)}{dt} = \sum_j \sum_l k_{jl} n(j) n(l) - n(i) \sum_j k_{ij} n(j), \tag{2.29}$$

which is to say that the abundance is determined by the sum of all producing reactions (of reactants $n(j)$ and $n(l)$) subtracted by the sum of all destructive reactions. The set of reactions (and their associative reaction rates k_{ij}) are taken from the Ohio State University Astrophysical Chemistry Group gas-phase model of 2008 (Smith et al., 2004) and was expanded on by adding unshielded photodissociation reactions from the UMIST 2006 database (Woodall et al., 2007) by Fogel et al. (2011) and has since been updated with the photodissociation rates of the UMIST 2012 database (McElroy et al., 2013). The chemical code and database have been well tested by these previous authors, and we have made no modifications to the core of the chemical code. The complete chemical database includes reaction rates for gas phase chemistry, grain surface reactions of hydrogen and water, photo-dissociation, X-ray and cosmic ray ionization, and grain absorption/desorption including thermal, cosmic ray and photodesorption. The chemical network includes 5909 chemical reactions and 9 chemical elements: H, He, C, N, O, S, Si, Mg, Fe (see Table 2.2).

The most prominent of the above reactions are driven through interactions between the gas and

the local radiation field. Reactions like ion driven gas chemistry, photo-dissociation and photodesorption are much faster than neutral gas reaction because of a lack of an activation barrier between reactants. To determine the UV and X-ray radiation field, previous works have relied on an in-house Monte Carlo radiative transfer code that included both opacities due to dust and gas (Weingartner & Draine (2001) and Bethell & Bergin (2011a) respectively) as well as line transfer for Lyman-alpha photons (see Bergin et al. (2003)), which can carry the majority of the UV flux through the disk. We found that this algorithm was computationally expensive, as it requires an iterative calculation to determine the number density of molecular hydrogen and the resulting radiation field (Bethell & Bergin, 2011a). A much more efficient radiative transfer code was needed to compute the chemical profiles in many disk snapshots (~ 300) in order to achieve the necessary temporal resolution discussed below.

Towards this end, we employ RADMC3D (Dullemond, 2012) to compute the radiation field, maintaining the same opacities as in the above sources. However the tradeoff is that we are neglecting the line transfer of Lyman-alpha photons, which means we are likely underestimating the total UV flux through our disk and the final abundance of some molecules that are dependent on UV photolysis to drive their production. For example the production of CN from the photolysis of HCN will obviously be reduced. This limitation is an issue when comparing computed disk astrochemistries to observations, a field that has seen major developments over the last decade. However, the molecules that have been detected or inferred in exoplanetary atmospheres are not as sensitive to the UV field. Since our focus is to compare our work with observations of abundances in exoplanetary atmospheres, neglecting Lyman-alpha photons will not significantly affect our results. In future works, we will improve both our disk model and radiative transfer schemes to more accurately replicate the chemical structure in accretion disks.

At every time step we initialize the chemical code with the temperature, surface density, and radiation field profiles calling the combinations of these profiles a 'snapshot' of the disk. The chemical code uses a 1+1D method where the chemistry is computed at each radii individually, up to ten scale heights. In this method no chemical information is exchanged between radii, so effects like radial mixing are ignored. To minimize possible errors from radial mixing we resolve the temporal evolution of the chemistry to timesteps that are less than the viscous time in the disk at 1 AU. This results in a timestep of approximately 13000 years. With this choice of timestep, changes in the chemical structure between temporal snapshots of the chemical disk are due to changing disk properties like

Table 2.2: Initial abundances relative to the number of H atoms. Included is the initial ratio of carbon atoms to oxygen atoms (C/O) and the initial ratio of carbon atmos to nitrogen (C/N).

Species	Abundance	Species	Abundance
H_2	0.5	H_2O	2.5×10^{-4}
He	0.14	N	2.25×10^{-5}
CN	6.0×10^{-8}	H_3^+	1.0×10^{-8}
CS	4.0×10^{-9}	SO	5.0×10^{-9}
Si^+	1.0×10^{-11}	S^+	1.0×10^{-11}
Mg^+	1.0×10^{-11}	Fe^+	1.0×10^{-11}
C^+	1.0×10^{-9}	GRAIN	6.0×10^{-12}
CO	1.0×10^{-4}	N_2	1.0×10^{-6}
C	7.0×10^{-7}	NH_3	8.0×10^{-8}
HCN	2.0×10^{-8}	HCO^+	9.0×10^{-9}
C_2H	8.0×10^{-9}	C/O	0.288
		C/N	4.09

temperature and surface density rather than radial transport of material.

As an additional approximation, we assume that the initial chemical abundances are the same for all disk snapshots, as shown in table 2.2. In doing this, the chemical structure of any given snapshot does not depend on the chemical abundances computed in the previous snapshot. This assumption does have implications on the chemical structure that is computed, however the majority of the effect is seen in regions of the disk where photochemistry has the highest impact. At the midplane, differences between a snapshot that is initialized with the values of table 2.2 and the same snapshot that is initialized with the abundance from the previous one are less than $\sim 10\%$ in the region of the disk where atmospheric gas accretion takes place (at radii within 1 AU). This assumption reduces our average computation time by a factor of 20 because successive snapshots can be run in parallel on a supercomputing cluster. This decrease in computing time is necessary for the time resolution we required for this work and will become increasingly important when a parameter study of our model is done. The initial concentration of the chemical species are shown in table 2.2 and was taken from Fogel et al. (2011) and Aikawa & Herbst (1999).

Figures 2.2 and 2.3 show the time evolution of the radial profiles of a set of gas and ice species in the chemical code. Generally we see strong variations in the abundance of most molecules over all radii as the disk ages. At low radii, where the disk is viscously heated the decreasing temperature causes features in molecular abundances to shift inward while maintaining most of its shape. Examples of this type of evolution is in both the gas and ice species of H_2O, CH_3OH, CO and CO_2, as well as the gas species of HCO+ and N_2H+. On the other hand at larger radii the temperature structure

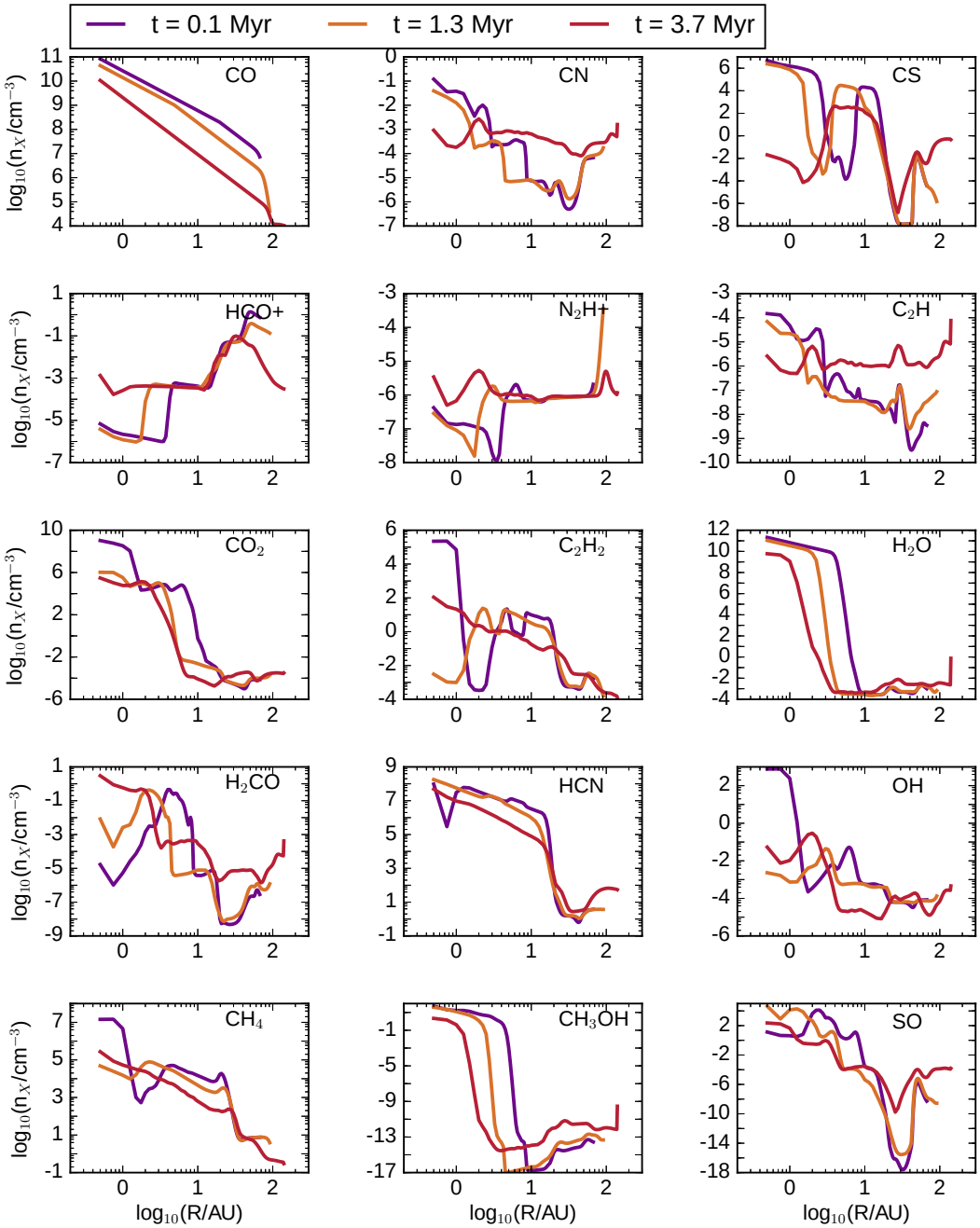

Figure 2.2: Number density at the midplane of the disk as a function of radius for a number of important gas molecules in our chemical model.

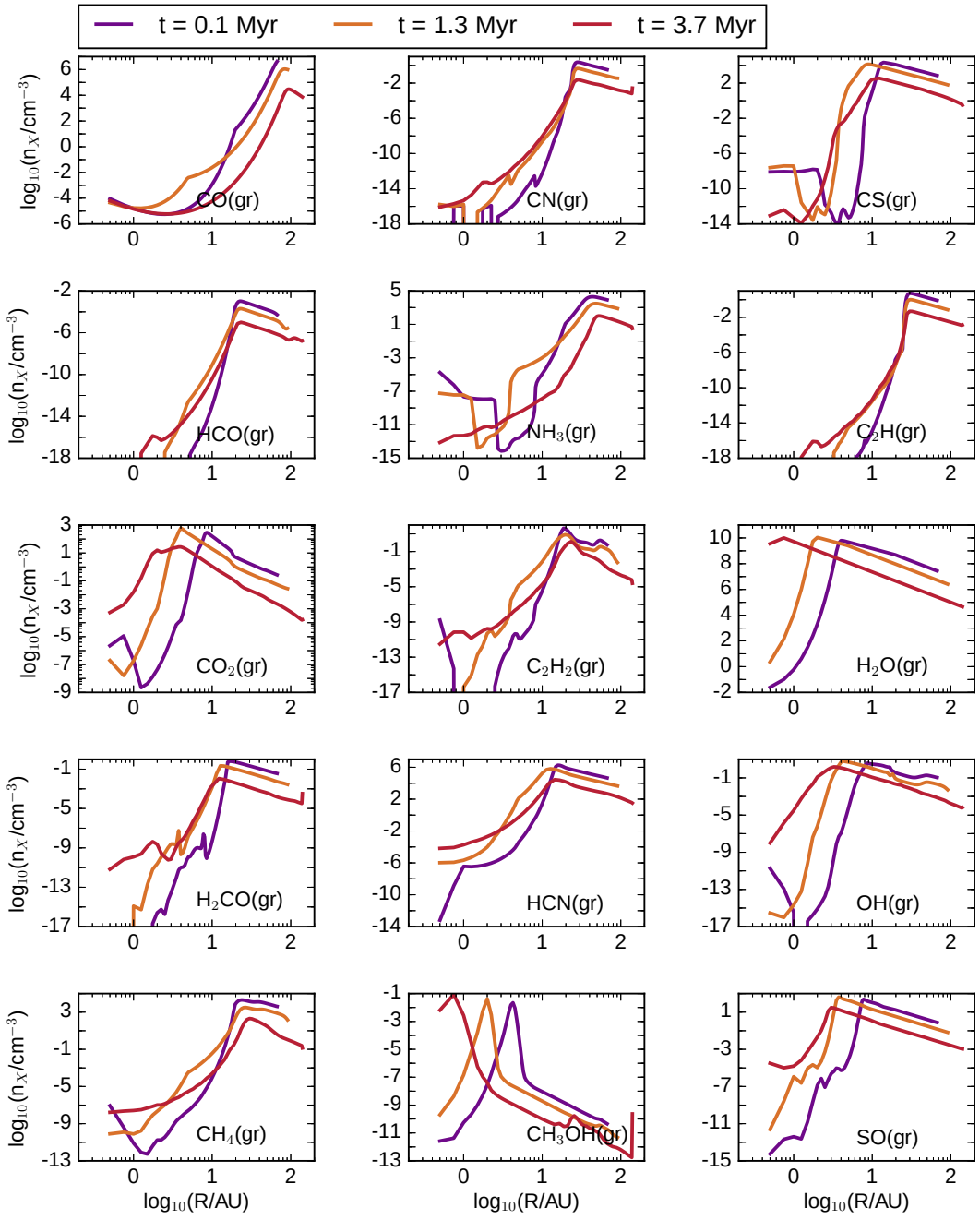

Figure 2.3: Same as in Figure 2.2 except for molecules frozen on grains. The only different chemical species is in the middle of the second row, as no frozen component of N2H+ exist in the model. Instead, the frozen component of NH3 is shown.

becomes passive in the radiatively heated regime of the disk and the evolution of the surface density becomes the primary driver of evolution. In the radiative regime, surface density reduction caused by the accretion of matter through the disk results in a larger flux of high energy photons, leading to variations in molecular abundance due to radiation driven chemistry. For example, the rate of reaction of photodissociation reactions has the form (Fogel et al., 2011)

$$k_{photodiss} = \int \frac{4\pi\lambda}{hc}\sigma(\lambda)J_\lambda(r,z)d\lambda \ s^{-1}. \tag{2.30}$$

As the surface density decreases the flux of photodissociating photons $J_\lambda(r,z)$ increases, leading to stronger irradiation of the midplane at all radii and a higher rate of gas species destruction.

This higher irradiation is also tied to the overall destruction of some species like CH_3OH at higher radii. While hydrogen and water are allowed to react on grains, other species are protected from further chemical evolution when they freeze onto dust grains because there are no other surface reactions included in the model (Fogel et al., 2011). However at higher radii species become more susceptible to desorption caused by high energy photons or cosmic rays. Once in the gas phase, these species are destroyed through reactions with ions or dissociation caused by cosmic rays. The rate of photodesorption depends both on the local radiation field as well as the properties of the dust species that are present.

In particular, this process appears important for methanol (CH_3OH, row 5, column 2 in Figures 2.2 and 2.3). From the Figures, we observe a freeze out at disk radii of ~ 5, 2.5 and 1 AU at 0.1, 1.3 and 3.7 Myr respectively, tracing the cooling of the disk as observed in other plots of other volatiles like water. At larger radii in each of the snapshots of the disk, there is a strong depletion of the frozen component of CH_3OH without an increase in the gas abundance at the same location. The survivability of methanol has interesting impacts on observations and is important for the formation of biologically relevant molecules like glycolaldehyde (Jørgensen et al., 2012).

Water undergoes a simpler time evolution and is in a class of species that is less sensitive to the presence of high energy radiation. Water vapour undergoes a strong reduction as seen in the ninth (row 3, column 3) panel of Figure 2.2 which is correlated with the strong increase of water ice in the ninth panel of Figure 2.3. This process is dominated by the equilibrium of freeze out and sublimation of water. The half height of this strong reduction will be where we define the location of the Ice line trap (see below).

2.4 Planet Formation and Migration

When a sufficiently small planetary core ($\leq$ a few Earth masses) is embedded in the disk, the disk structure is not drastically changed. However, spirals waves are excited through constructive interference of density waves at Lindblad resonances (Ward, 1997). These density waves exert torques on the planet which generally result in a loss of angular momentum from the planet to the disk, forcing the planet to migrate inwards (this is known as Type-I migration). The direction of the migration is set by both the surface density and temperature profiles. For simple disk distributions, only the two closest Lindblad resonance positions contribute to the net torque on the planet. One resonant location is at a larger disk radius than the planet, while the other is at a smaller radius (outer and inner resonances respectively). The outer resonance lies closer to the planet than the inner resonance. It has a stronger effect transferring angular momentum from the planet to the disk, causing net inward migration. Early on in planet formation theory, it was realized that the timescale for planet formation ($\sim 10^6$) was much longer than the timescale for Type-I migration ($\sim 10^5$, Ward (1997), Masset et al. (2006)). Current three dimensional migration calculations reproduce these low migration timescales, and still need to be reduced by a factor of between 10-100 (Masset et al., 2006) to account for the survival of planets.

There is a second source of torque on the migrating planet which contributes to Type-I migration: the corotation torque. Also known as the horseshoe drag, corotation torques are caused by gravitational interactions between particles on horseshoe orbits around the planet (Ward, 1991). Horseshoe orbits occur for fluid packets that have orbital frequencies similar to that of the planet. Since a fluid packet is initially at a larger orbital radius than the planet, as the planet catches up to the packet it is perturbed to a lower orbit and loses angular momentum. The packet at the lower orbit now moves faster around its orbit than the planet, catching up to the planet within an orbital period. At this point the planet perturbs the packet again up to a higher orbital radius, regaining the lost angular momentum from the first encounter of the horseshoe orbit.

Since a disk is generally cooler the further it is from the star, a fluid packet that moves from the outer region of the horseshoe orbit to the inner region will be cooler than the surrounding gas. If the fluid packet returns to the opposite side of the horseshoe orbit without changing (ie. no turbulent mixing) there is no net angular momentum transfer between the fluid packet and the planet over the full horseshoe orbit described above. Under such a situation the corotation torque is said to be

'saturated'. This occurs if the viscous diffusion timescale are longer than the libration time of the horseshoe orbit. In the opposite case the torque is called 'unsaturated'. The corotation torque, when unsaturated, can overcome the Lindblad torques in most disk set-ups, leading to slowed or outward migration. To determine if the corotation torque is saturated, one must compare the libration and the viscous timescales. The libration time and viscous time has the form (Masset & Papaloizou, 2003):

$$t_{Lib} = \frac{4\pi r_p}{1.5\Omega_p x_s} \tag{2.31}$$

$$t_{vis} = \frac{x_s^2}{3\nu}, \tag{2.32}$$

respectively. Here r_p is the radial position of the planet and Ω_p is the Kepler frequency at r_p. The viscosity ν is defined in Equation 2.6. The distance traversed by the fluid packet through the horseshoe orbit x_s is defined by

$$x_s = 0.96 r_p \sqrt{\frac{M_p r_p}{M_* h_p}} \tag{2.33}$$

where the M_p is the mass of the planet and h_p is the scale height of the disk at the location of the planet.

In Figure 2.4 the ratio of these timescales are shown for four different planet masses for our evolving fiducial disk. The smallest bodies are trapped over a long time by an unsaturated corotation torque for both turbulently dead and turbulently active disk (denoted by an α_{turb} of 10^{-5} and 10^{-3} respectively). If the libration time is larger than the viscous time the turbulence is sufficiently strong to mix the packet of fluid with the surrounding fluid, keeping the corotation torque unsaturated. In the turbulently active disk, only the most massive planets ($\gtrsim 10$ $M_\oplus$) will see a saturated corotation torque at times $\gtrsim 1$ Myr; however at this higher mass Type-II migration will set in and this test does not apply. In the turbulently dead zone a 1 $M_\oplus$ planet will be trapped by the corotation torque for a few hundred thousand years before the corotation torque saturates. In general a protoplanet will begin its evolution on the trajectory of the smallest planet in Figure 2.4. As a planet accretes matter it will shift from one line to another, entering into a saturated region earlier than a planet that is not undergoing mass accretion.

Strong density, temperature or vortensity gradients can reverse the direction of Lindblad torques

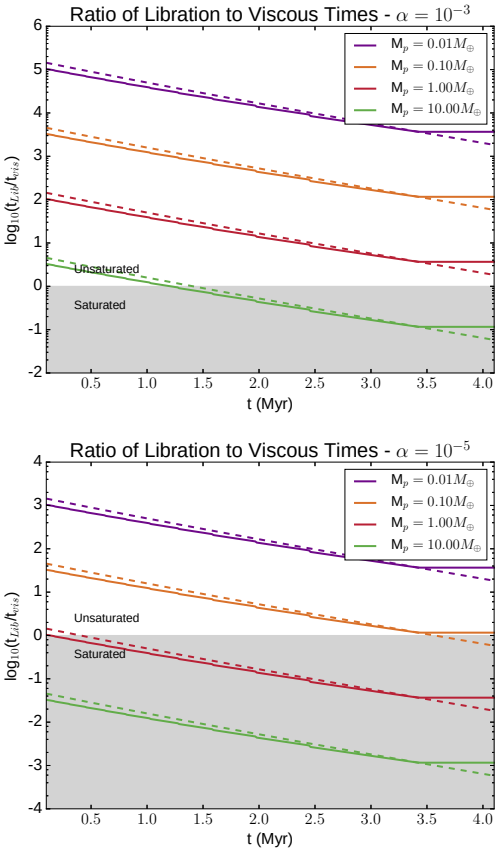

Figure 2.4: Ratio of libration time to viscous time for an active ($\alpha_{turb} = 10^{-3}$) and dead ($\alpha_{turb} = 10^{-5}$) disk. In both cases, the location of the planet is determined by the location of the ice line (solid line) and heat transition traps (dashed line) for a fiducial disk model. The gray region denotes the parameter space where the corotation torque is saturated.

or can strengthen the impact of corotation torques, halting Type-I migration (Paardekooper et al., 2010). We call these inhomogeneities 'planet traps' and we select discrete disk properties to define their position and evolution. A complete picture of the evolution of our three planet traps of interest (see below) has been computed by Hasegawa & Pudritz (2011). The three planet traps of interest in our model are the water ice line, heat transition, and dead zone. In what follows, we extend the work of Hasegawa & Pudritz (2011) by including the above mass dependent saturation test when the ice line and heat transition traps are located within the dead zone of the disk.

2.4.1 Defining a Planet Trap

Our disk chemistry calculations allow us to improve on previous methods of defining the location of the above planet traps, as two of the traps can be defined by the chemical structure of our protoplanetary disk model.

Heat Transition Trap

The simplest trap to identify is the heat transition trap, which is located at the transition radius between a region primarily heated through viscous heating and a region heated through direct irradiation. This radius is defined in Chambers (2009) and is identified for three computed temperature profiles in Figure 2.5.

In Figure 2.5 we show the evolution of the midplane temperature profile for our fiducial disk model at $0.1, 1.3$ and 3.7 Myr. The times are selected to represent the disk at its 'early', 'middle' and 'late' ages for the fiducial model presented. The lowest temperatures are due to direct irradiation and is time independent, as we assume that the star is not evolving during the full lifetime of the disk, and that the disk is isothermal from the disk photosphere down to the midplane. At the highest temperatures its functional form is modified by what is known as the evaporative region in Chambers (2009). In this region the opacity is allowed to vary with temperature while the disk is heat through viscous evolution. Aside from this innermost regime, both the viscous and irradiated regimes are assumed to have the same opacity. As in Chambers (2009) we note that a constant opacity is not a realistic representation for an astrophysical accretion disk, and indeed a more complete representation of opacity has been carried out by Stepinski (1998), Bell et al. (1997) & Bell & Lin (1994). However this picture is further complicated by dust settling and growth and a full description evades an analytical solution, as in the combination of Equations 2.18, 2.25, 2.17 and

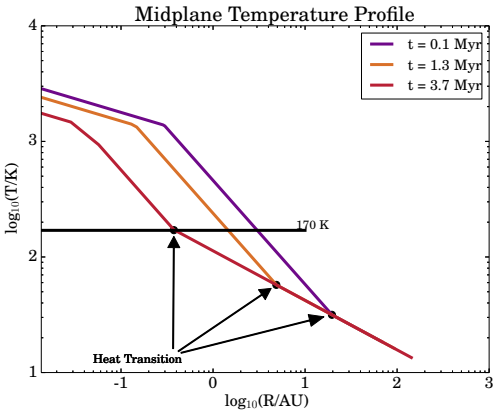

Figure 2.5: The temperature profile (Equations 2.18 and 2.25 along with the modification from Equation 2.34 on Equation 2.18) for three snapshots are shown for the fiducial disk (Table 5.2). The black dot and arrows denote the defined location of the heat transition trap for three temperature profiles shown here. The intersection between the horizontal line and the temperature profile at $170K$ denotes an approximate location of the water ice line in this model. In the radiative region, the temperature profile becomes independent of time, and the profiles overlap in this region.

2.27. In other astrochemical works, dust settling has been completely ignored (Walsh et al., 2012) or has been been computed as a consequence of the equilibrium between gravitation and turbulent mixing (Cleeves et al., 2014; Helling et al., 2014) in a passive disk. A time dependent treatment of dust evolution, which is susceptible to processes like radial drift (Birnstiel et al., 2012), has yet to be connected to chemical evolution. We leave the analysis of the impact of evolving dust structure to a future paper.

In the context of our analytic disk model, we choose to keep the dust opacity constant at a temperature below the evaporation temperature of dust ($\sim$ 1380 K). The full functional form of the opacity is (Chambers, 2009),

$$\begin{aligned} \kappa &= \kappa_0 && T < T_e \\ \kappa &= \kappa_0 \left(\frac{T}{T_e} \right)^n && T > T_e, \end{aligned} \tag{2.34}$$

where $T_e = 1380$ K is the evaporation temperature and $n = -14$ (Stepinski, 1998). This equation is combined with Equations 2.13 and 2.14 where it replaces the constant κ_0. With this modification, the temperature profile changes from the standard profile in the viscously heated region of the disk at small radii.

Table 2.3: Power law exponents and ratio of specific heats used in the Chambers model. The last row denotes the sign of the total torques on the planet locally around the heat transition.

	Viscous	Radiative
s	$\frac{3}{5}$	$\frac{15}{14}$
β	$\frac{9}{10}$	$\frac{3}{7}$
γ	1.4	1.4
ξ	$\frac{33}{50}$	0
$sign(\Gamma)$	$+1$	-1

The location of the heat transition trap is highlighted three times in Figure 2.5. As time goes on the position of the heat transition moves inward as the viscous region cools and more of the disk is heated by direct irradiation. The origin of this trap is generally due to an entropy gradient across the trap, on which the strength of the corotation torque depends.

Paardekooper et al. (2010) showed that the total torque from both the Lindblad resonances and unsaturated corotation torques are,

$$\frac{\gamma\Gamma}{\Gamma_0} = -2.5 - 1.7\beta + 0.1s + 1.1\left(\frac{3}{2} - s\right) + 7.9\frac{\xi}{\gamma}, \tag{2.35}$$

where s and β are the exponents in Equation 2.4, $\xi \equiv \beta - (\gamma - 1)s$ is the power law exponent for the entropy and γ is the ratio of specific heats. $\Gamma_0 = (q/h)^2\Sigma_p r_p^4 \Omega_p^2$ is the standard normalization of torques on a planet at position r_p of the planet. In the Chambers (2009) model the relevant values in both heating regimes are shown in Table 2.3.

Substituting power law indices in both the viscous and irradiated regimes shows that the sign of the total torque is positive in the viscous region, so that the planet will migrate outwards. Meanwhile, in the radiative region the sign of the total torque is negative and the planet will migrate inward. The reversal of the total torques cause the planet to be trapped at the transition point between the two heating sources. As seen in Figure 2.5 the heat transition begins out beyond 10 AU and moves inward of 1 AU by $2 - 3$ Myr. A trapped planet will travel over an order of magnitude in radius through the disk, and should sample a wide range of gas with varying chemical abundances.

Ice Line Trap

In the previous work of Hasegawa & Pudritz (2011) the ice line trap was defined as the position in the disk that has a temperature equal to the sublimation temperature of water vapour (directly from ice). This sublimation temperature is approximately 170 K and is denoted by the horizontal line in

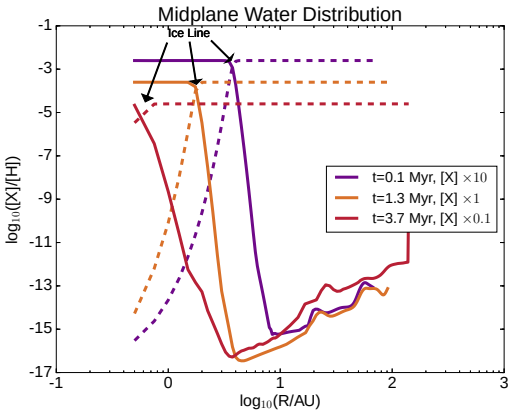

Figure 2.6: Number density of water vapour (solid line) and water ice (dashed line) relative to hydrogen - offset to minimize overlap. In reality each curve has the same maximal abundance. The ice line refers to the transition point between the disk's water content being primarily in vapour form to primarily in ice. As the disk ages and cools, the ice line moves inward on the viscous timescale, eventually disappearing beyond our resolution range.

Figure 2.5. The traditional methods assumed that the only limiting effect on the amount of water vapour was the local temperature of gas, and the relative rates of thermal absorption and desorption. To improve on this previous method we use the results of our astrochemical code to locate the radial position of the ice line at the midplane.

In Figure 2.6 we show the abundance of water vapour (solid line) and water ice (dotted line) relative to the abundance of hydrogen at the same times shown in Figure 2.5 for our fiducial disk. At the earliest times the abundance of water vapour, relative to hydrogen, does not evolve other than across the ice line. So in the figure, we have multiplied each line by a factor of 10, 1, and 0.1 for the times 0.1, 1.3 and 3.7 Myr respectively to better display each curve. The water ice line is defined by the position in the disk where the abundance of water vapour and ice is equal. By using a full chemical code, we gain an immediate insight into other effects that might play a role in determining the position of the ice line outside of simply the gas temperature, such as pressure and radiative effects.

At the ice line, the opacity κ is reduced as the dust grains are coated with water ice, and the associated cooling rate of the gas is increased (since $D \sim 1/\kappa$, Bitsch et al. (2013)). Coupled to the cooling rates, the local temperature and thus the disk scale height, is reduced ($H \sim c_s \sim T^{1/2}$). In the standard α-disk model the mass accretion through the disk ($\dot{M} \sim \nu\Sigma$) is assumed to be constant. Because the viscosity is dependent on the local gas temperature ($\nu \sim c_s H \sim T$), a reduced

temperature results in an enhancement in the local surface density at the ice line to maintain a constant mass accretion. Both a modified temperature structure and density enhancement impact the direction of the net torques by locally increasing the scale height of the disk at radii just larger than the trap location. This increased scale height results in a large negative temperature gradient ($\beta > 0$) and a large positive surface density gradient ($s < 0$) across the ice line trap, and a strong negative torque outside of the trap (see Equation 2.35).

Figure 2.5 also shows that two traps might cross in space at some point in the disk history, which appears to occur at about 3.7 Myr in the fiducial model. Two interesting dynamic questions can be asked: what happens to two planets that are forming simultaneously in the two traps when they cross? If only one planet is forming in one of the traps, does the planet 'jump' to the other trap when they cross? Both of these questions are beyond the scope of this work but offer an interesting future addition to our model, where forming planets are allowed to interact dynamically with each other.

Dead Zone Trap

As was outlined in §2 we focus on disk turbulence that is driven by the magnetorotational instability (MRI). The ability of the MRI to excite turbulence is dependent on the magnetic field's coupling to the ionized gas in the accretion disk. This ability is often characterized by the Ohmic Elsasser number (Equation 2.7) which compares the rate of growth of MRI driven turbulence to the rate that energy is dissipated through Ohmic diffusion. As shown in Equation 2.8 the Ohmic resistivity depends on the disk electron fraction which we compute by comparing the abundance of electrons to the abundance of hydrogen from the chemical code.

When the disk ionization is high enough that the Ohmic Elsasser number is above a critical value of $\Lambda_{O,crit} \equiv 1$ the disk is turbulently active from the MRI (Blaes & Balbus, 1994; Simon et al., 2013; Fromang, 2013). We define the location of the dead zone trap as the radius in the disk where $\Lambda_O = 1$ and track this radius. In the dead zone the turbulent parameter (α_{turb}) drops by about two orders of magnitude relative to the active region of the disk and the disk accretion rate due to turbulence is drastically decreased. In the dead zone the dust scale height is lower than in the active zone, thereby presenting a 'dust wall' to the incident radiation. The back scattered radiation from the wall produces a radial temperature inversion and a thermal barrier to Type I migration (Hasegawa & Pudritz, 2010).

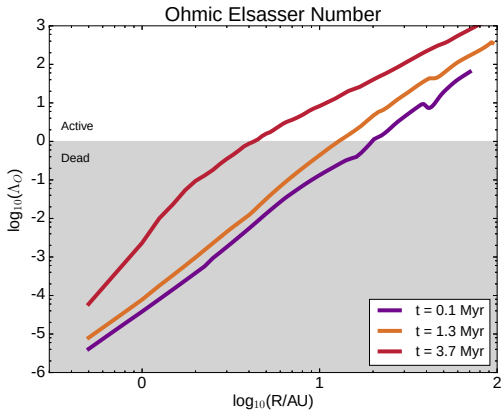

Figure 2.7: Ohmic Elsasser number over three disk snapshots. The line between the white and grey regions denote the critical Ohmic Elsasser number $\Lambda_{O,crit} \equiv 1$ above which the disk would be turbulently active due to the MRI. The dead zone trap is denoted by the location where the Ohmic Elsasser number first (from the right) crosses into the dead region.

In Figure 2.7 we show the Ohmic Elsasser number in the fiducial model at the same times as in Figure 2.5. We also show the Ohmic Elsasser numbers which suggest where the disk would be active (white region) and where we expect it to be dead (gray region). As the surface density of the disk drops the flux of ionizing radiation can increase, enhancing the electron fraction and Ohmic Elsasser number. The electron fraction is computed by our astrochemical code and is dependent on the local radiation field, as well as the average size of the dust grains. In this fiducial model the dust grains are completely mixed with the gas and do not undergo any size evolution, remaining at a radius of ~ 4 μm for the lifetime of the disk. This size represents an average grain in the MRN distribution (Mathis et al., 1977) weighted by a freezing efficiency factor that is found in the chemical code. This factor affects the absorption rate of gas species onto grains and scales with the grains size. Larger grains have less surface area for absorption per mass of dust, and so the freezing efficiency is reduced.

As was outlined earlier, the likelihood that a planet will be trapped by the combined effect of the Lindblad and corotation torques depends on the magnitude of the α_{turb} parameter at a particular location of the disk. This implies that the location of the dead zone will also determine whether the corotation torque responsible for the other traps will be saturated or unsaturated. If either the ice line or heat transition traps exist within the dead zone of the disk (where we assume $\alpha_{turb} = 10^{-5}$) our analysis has shown that the corotation torque could saturate for a large enough planet. With the saturated corotation torque the semi-major axis of the young planet evolves only through Lindblad

torques in a standard Type-I migration scenario.

The magnitude of the total torque is (Seager, 2010),

$$\Gamma = C_\Gamma \Sigma \Omega_p^2 a^4 \left(\frac{M_p}{M_s}\right)^2 \left(\frac{a}{|\Delta r|}\right)^2. \tag{2.36}$$

When the scale height of the disk at the planet location H_p is less than the Hill radius R_H of the planet the gravitational effect of the planet on the gas is larger than the internal pressure of the gas and the relevant length scale of the density gradient is $|\Delta r| = R_H$. The opposite is true when the effects of gas pressure are larger than gravity, so we write $|\Delta r| = max(H, R_H)$ to account for both limits. The constant C_Γ has been computed through numerical simulations of Type-I migration, it has a value of $C_\Gamma = -(2.34 - 0.10s)$ (Seager, 2010) for the saturated corotation torque.

The radial evolution of the planet is $\dot{r}_p/r_p = \Gamma/J_p$ where $J_p = M_p \Sigma_p r_p^2$ is the orbital angular momentum of the planet, leading to,

$$\frac{1}{r_p}\frac{dr_p}{dt} = \frac{C_T \Sigma \Omega_p r_p^2}{M_p} \left(\frac{M_p}{M_s}\right)^2 \left(\frac{r_p}{max(H, R_H)}\right)^2. \tag{2.37}$$

If the ice line and heat transition trap are within the dead zone we calculate the ratio of the libration and viscous time to determine whether or not the planet would be trapped at each timestep. If the ratio of the libration time (Equation 2.31) is larger than the viscous time (Equation 2.32) the radial position of the forming planet is defined by the location of the trap.

This analysis is a recent addition to our model because of our chemically motivated method of inferring the location of the dead zone. Previous works relied on an analytic method of determining the ionization structure in the disk. It was generally found that the radial position of the dead zone was well within the other two traps for the entire disk lifetime (Hasegawa & Pudritz, 2013) or evolved inwardly of the two traps quickly enough (Alessi et al., 2017) that such an analysis was not necessary.

Generally we assume that the radial location of the trapped planet will follow the location of its planet trap exactly. At every timestep we check the ratio of the libration time to viscous time, and in the case that the ratio t_{Lib}/t_{vis} is less than one the radial evolution is defined by Equation 4.7.

2.4.2 Planet Formation Model

Our planet formation model is based on the standard core accretion model of Ida & Lin (2004). The planet grows by first growing a solid core through oligarchic growth (Kokubo & Ida, 2002) followed by gas accretion onto the established core regulated by the Kelvin-Helmholtz (KH) timescale (Ikoma et al., 2000). The core begins at one hundredth the mass of Earth and quickly migrates into one of the three planet traps. The core then grows at the radii defined by the planet trap until it reaches a mass large enough to open a gap and begin Type-II migration.

In the core accretion model the core undergoes three phases of accretion. The first phase is a rapid solid oligarchic growth, with growth timescales of $O(10^5)$ yr. The mass accretion rate of the solid core is defined as (Ida & Lin (2004), their equations 5 and 6):

$$\begin{aligned}\frac{dM_c}{dt} &= \frac{M_c}{\tau_{c,acc}} \\ &\simeq \frac{M_c}{1.2\times10^5}\left(\frac{\Sigma_d}{10\mathrm{gcm}^{-2}}\right)\left(\frac{a}{1\mathrm{AU}}\right)^{-1/2}\left(\frac{M_c}{M_\oplus}\right)^{-1/3}\left(\frac{M_s}{M_\oplus}\right)^{1/6} \\ &\times\left[\left(\frac{\Sigma_g}{2.4\times10^3\mathrm{gcm}^{-2}}\right)^{-1/5}\left(\frac{a}{1\mathrm{AU}}\right)^{1/20}\left(\frac{m}{10^{18}\mathrm{g}}\right)^{1/15}\right]^{-2}\ \mathrm{g\ yr}^{-1},\end{aligned} \tag{2.38}$$

where Σ_g and Σ_d is the surface density of gas and dust respectively, M_c is the mass of the core and m is the average mass of the accreting planetessimals.

During oligarchic growth little to no gas is accreted since the accreting oligarchs keep the core too hot. When the core reaches its 'isolation mass', defined by Ida & Lin (2004) as the maximum available solid mass within 10 Hill radii of the core, solid accretion stops and a phase of slow ($O(10^6)$ yr) gas accretion begins. The gas accretion is regulated by the KH timescale, parameterized by (Hasegawa & Pudritz, 2012),

$$\tau_{KH} \simeq 10^c\mathrm{yr}\left(\frac{M_p}{M_\oplus}\right)^{-d}, \tag{2.39}$$

so that the gas accretion rate has the form,

$$\frac{dM_p}{dt} \simeq \frac{M_p}{\tau_{KH}}, \tag{2.40}$$

where M_p is the total mass of the forming planet, and the parameters $c = 9$ and $d = 3$ are fiducial

values (Ida & Lin, 2004) that adequately reproduce the mass-period relation for the population of observed exoplanets (Hasegawa & Pudritz, 2013). If the forming planet accretes enough mass for the KH timescales to drop below about 10^5 yr the planet enters into a phase of unstable gas accretion, where it rapidly draws down the remaining gas in its feeding zone.

At some point before this final accretion phase the planet becomes massive enough to open a gap in the disk and decouples from its planet trap, entering into a phase of Type-II migration. The 'gap opening' mass requires the planet's Hill radius to be larger than the pressure scale height at the planet's location, otherwise the gap will be closed by gas pressure. A second requirement is that the torques from the planet on the disk exceeds the torques caused by viscous stress. These requirements are summarized by, (Hasegawa & Pudritz (2012),Lin & Papaloizou (1993)),

$$\frac{M_{gap}}{M_*} = min\left[3h_p^3, \sqrt{40\alpha_{turb}h_p^5}\right], \tag{2.41}$$

where $h_p \equiv H_p/r_p$. When the gap is opened the planet decouples from the evolution of the planet trap, evolving on the viscous time

$$t_{mig} = t_{vis} = \frac{r_p^2}{\nu}. \tag{2.42}$$

This migration timescale is increased due to the inertia of the planet when it is above a critical mass $M_{crit} = \pi\Sigma_p a^2$, which is the approximate mass of the disk interior to the planet. Above the critical mass the migration time scale is,

$$t_{mig} = \frac{r_p^2}{\nu}(1 + M_p/M_{crit}), \tag{2.43}$$

and the radial evolution for Type-II migration is,

$$\frac{dr_{p.II}}{dt} = \frac{r_p}{t_{mig}}. \tag{2.44}$$

Understanding how mass accretes onto the planet after the gap opens is still an open question and one that requires the results of detailed 3D numerical simulations of accretion onto migrating planetary cores (see for example the numerical simulation of Kley (1999)). It may be that the accretion is at least regulated by the global mass accretion rate in the disk.

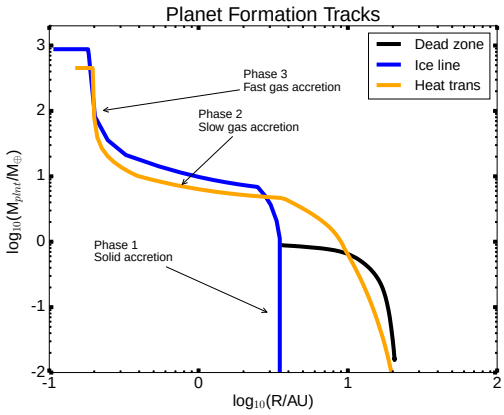

Figure 2.8: Full planet tracks for our fiducial disk setup. Each track is associated with a single planet forming in isolation, without any dynamical interactions between other planets in other tracks. We also ignore interactions if two traps cross in space, so that there is no 'trap jumping'. We annotate the three phases of mass accretion: Phase 1: Oligarchic growth, Phase 2: Slow gas accretion, limited by the Kelvin Helmholtz timescale and Phase 3: Rapid gas accretion, regulated by a Kelvin Helmholtz timescale $t_{KH} < O(10^5)$.

In this work, we parameterize the maximum mass of the planet with a fiducial value of fifty times the gap opening mass (fiducial value in Hasegawa & Pudritz (2012, 2013) and Alessi et al. (2017)), above which we shut off the accretion onto the planet. This is a necessary parameterization due to the unstable nature of the Kelvin Helmholtz rate of accretion. Between the gap opening mass and the maximum mass we maintain the same prescription for gas accretion as in Equation 4.3.

When combined with the planet trap model for planet migration this prescription for planet formation produces a well defined evolutionary track through the planet mass-semimajor axis space that we define as a 'planet track'.

In Figure 2.8 we show three examples of such tracks. For our choice of disk parameters ($M_{disk}(t = 0) = 0.1$ M$_\odot$, $s_{disk}(t = 0) = 66$ AU, t$_{life} = 4.10$ Myr) we find that two of the planets end up being 'Hot Jupiters' while the third fails to grow to a significant mass by the end of the disk lifetime. The location of these planet tracks, and the overall evolution of the growing planet depends on the location of the planet's natal planet trap. The location of the planet traps will depend on the disk model parameters that are selected, so a complete picture of possible planets will depend on a full population synthesis model that we leave for future work. Qualitatively, our planet tracks match the results from Hasegawa & Pudritz (2012), apart from a trend that planets whose corotation torque saturates will tend to tilt farther to the left (migrate to lower orbital radii) during their phase of

solid accretion than planets whose torques remain unsaturated.

During the oligarchic growth phase the mass accretion of the core is given by Equation 2.38. When the core reaches its isolation mass the mass accretion is dominated by gas accretion given by Equation 2.40. When the planet reaches its gap opening mass (Equation 2.41) the radial evolution is no longer governed by Type-I migration, and is instead given by Equation 2.44.

Combining the core accretion model with planetary migration allows us to track the chemical composition of the material accreted onto the exoplanetary atmosphere. When combined with our full set of temporal snapshots of the chemical disk and our migration model outlined above, we can compute a full picture of the chemical makeup of the material being accreted onto the forming planet.

2.5 Atmospheric Compositions: Results

We evolve a fiducial disk model with parameters listed in table 5.2 and compute the formation of planets in each of the three planet traps outlined above. When evolved these disk model parameters produce a disk which ranges in mass from $0.013 \rightarrow 0.0044$ $M_\odot$ for a disk age range of $2 \rightarrow 3$ Myr respectively. Submillimeter surveys of star forming regions have yielded mass ranges of $0.00143 - 0.0153$ $M_\odot$ for disks around stars with ages ranging between $2 - 3$ Myr (see Andrews et al. (2013), Williams et al. (2013) and Cieza et al. (2015)).

2.5.1 Condensation Front Locations: Comparison with TW Hya and HL Tau

Some of the most important observational features in protoplanetary disks are condensation fronts (or equivalently 'ice lines') which are the disk radii where the temperature falls below the sublimation temperature of volatile species. At these temperatures, the freezing efficiency of the volatile species approaches unity and the majority of chemical species become frozen onto grains. Carbon monoxide is a convenient molecule to study the effects of condensation fronts as it reacts with another easily detected molecule, N_2H+. In the gas phase, N_2H+ is created through protonation of gaseous N_2 down to a few degrees above the freezing temperature of CO ($\sim$ 20 K). It is destroyed primarily through reactions with gaseous CO (Qi et al., 2013). Another important observational tracer is

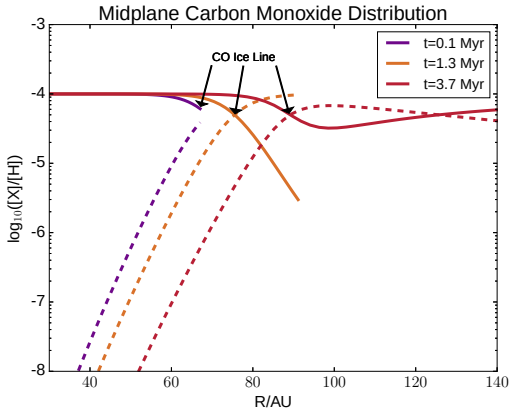

Figure 2.9: Midplane CO distribution of the gas (solid line) component and frozen (dashed line) component, from 10 AU to 100 AU. The location of the CO ice line (condensation front) is denoted with the arrow, at a position that varies from $\sim$ 60 AU out to 65 AU for disk time from 0.1 Myr to 3.7 Myr respectively.

formaldehyde (H_2CO) which can be efficiently produced by Hydrogen capture of frozen CO, then non-thermally desorbed to produce a gas component of H_2CO (Qi et al., 2013).

Observational surveys use the emission from these tracer molecules to infer the location of the CO condensation front. The quoted locations vary considerably between observational studies, from 25, 30 to 160 AU (Qi et al., 2013; Pontoppidan et al., 2014).

In Figure 2.9 we show the ratio of CO gas and ice to Hydrogen atoms for radii ranging from 30 AU to the outer edge of the disk, highlighting the evolution of the location of the CO ice line in our model. It evolves outward from $\sim$ 62 AU out to $\sim$ 90 AU between 0.1 and 3.7 Myr in the region of the disk that is primarily heated through direct irradiation. As seen in section 2.4.1 the region of the disk that is heated through direct irradiation produces a temperature profile that is constant in time. Unlike water in Figure 2.6, carbon monoxide also evolves through a variety of other reactions other than freezing onto grains. In particular it is sensitive to the local UV field which photodesorbs the molecule off of dust grains. As the density of the dust is reduced the efficiency of CO adsorption is reduced and the rate of photodesorption is increased. Both of these affects conspire to move the location of the ice line outward as the disk evolves and the density drops.

The condensation front of water is another important feature in protoplanetary disks as it represents a sharp transition in the opacity structure of the disk. Detecting the effect of the water ice line is generally limited by resolution, and only a limited number of detections have been completed with *Spitzer* and *Herschel*. In TW Hya a strong water vapour emission is detected at about 4 AU

but drops off by orders of magnitude at 4.2 AU (Zhang et al., 2013), suggesting that the ice line can be defined as a sharp transition point between the gas and ice phase of water.

This sharp transition can be seen in our own work in Figure 2.6 where the water vapour drops off by over two orders of magnitudes within half an AU. The disk around TW Hya is classified as a transitional disk, which is a class of old systems that are undergoing the final stages of photoevaporation of the gas disk. The potential detection of the ice line in TW Hya represents an upper limit to the radial location of the ice line during the early stages of the protoplanetary disk. As the gas disk evaporates from the inside out, any remaining water ice will be photodesorbed back into the gas and then lost from the disk by the photoevaporating UV field of the host star. The strong water vapour detection would then represent the evaporation front of the disk as seen in theoretical calculations of photoevaporation (Gorti et al., 2015).

Condensation fronts have also been proposed as the source of the emission gaps observed in the HL Tau disk by ALMA. Recent experiments have suggested that icy covered grains tend to be 'stickier', increasing the efficiency of dust coagulation. Because the (sub)mm observations of ALMA predominately detect the emission of micron sized grains, it fails to detect the larger grains that are expected to exist at the condensation front (Zhang et al., 2015). The observations made of HL Tau show three main bands of reduced intensity at approximately 13 AU, 32 AU and centered at 63 AU (although the reduced intensity is about 10 AU wide).

Zhang et al. (2015) interpret the locations of the first two gaps as being the ice lines of water and pure or hydrated NH_3. While the third gap is interpreted as starting at the ice line of CO_2 and passing through the freeze out of CO and N_2.

HL Tau is identified as a young disk, with an age $O(10^5)$ yrs into the Class 2 phase, so we compare to our fiducial model at $t = 10^5$ yr. The ice lines for H_2O, CO_2, NH_3, and CO are located in our fiducial model at approximately 3.5, 10, 20, and 62 AU respectively. We find that the approximate locations of the NH_3 and CO ice lines agree with the locations inferred through observations of HL Tau, which is the first source that could be studied in enough detail to infer these properties. The disagreement at small radii may imply that HL Tau is more representative of a disk with parameters that differ from our fiducial model. This region of the disk is heated primarily by viscous sources which tend to be more sensitive to disk parameters such as the initial mass accretion rate and disk size than the radiatively heated region at larger radii. Our forthcoming population synthesis paper will address these issues.

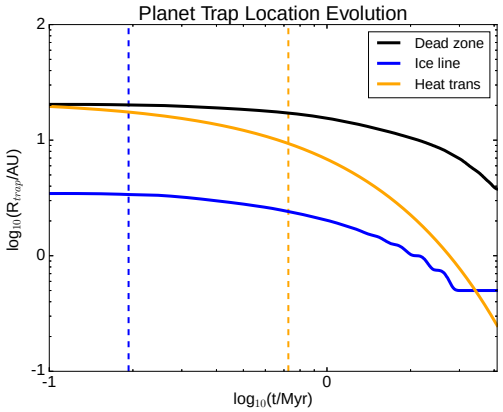

Figure 2.10: The temporal evolution of the planet traps in our model. The vertical lines denote the location and time where the corotation torque saturates and the radial evolution of the planet decouples from the radial evolution of the trap.

2.5.2 Computing the Initial Atmospheric Composition of a Forming Exoplanet

We begin our planet formation model (see Table 5.2) at 0.1 Myr, giving enough time for the initial core of 0.01 $M_\oplus$ to grow and initialize our computation. At this initial time the three planet traps are located at:

$$\begin{aligned} \text{Dead zone}: &\quad 21 \text{ AU} \\ \text{Heat transition}: &\quad 19.6 \text{ AU} \\ \text{Water ice line}: &\quad 3.5 \text{ AU} \end{aligned}$$

With the ice line and heat transition trap both starting within the dead zone we must assess whether the forming planet will actually be trapped using Equations 2.31 and 2.32. Where the trap initially starts determines the length of time prior to the saturation of the corotation torque. The ice line saturates at a time of about 0.19 Myr and the heat transition saturates later at 0.73 Myr.

Figure 2.10 shows the time evolution of each planet trap and the location where the corotation torque saturates and the planet migrates under standard Type-I migration caused by Lindblad torques. When combined with our planet formation model we compute the planet tracks shown in Figure 2.11.

In Figure 2.11, each planet track is annotated to demonstrate how much time the planets linger

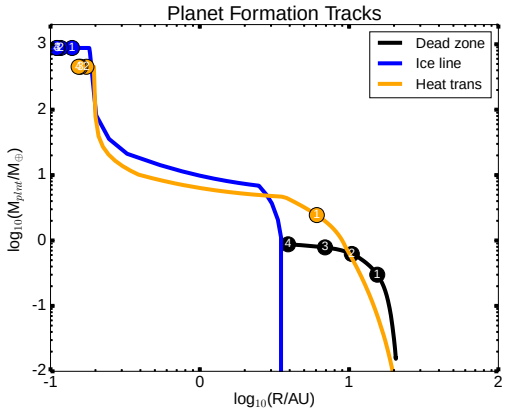

Figure 2.11: Full planet formation tracks along with annotations showing the location of the planet in the mass-semimajor axis space for 1, 2, 3 and 4 Myr. At small radii planets spend a very short time accreting its solids and can reach super-Jovian masses in less than 1 Myr. The saturation of the corotation torques also help to speed up formation of Jupiter mass planets, as the planet quickly moves into regions of the disk with higher surface densities.

Table 2.4: Final planetary properties at $t = t_{life}$

	M ($M_{\rm Jupiter}$)	a (AU)
Dead zone	0.003	3.7
Ice line	2.67	0.11
Heat transition	1.43	0.15

in each evolutionary phase. In general we see that the planet which is initialized in the ice line trap grows very quickly, and reaches its maximum mass within 1 Myr of disk evolution. This rapid growth is due to the rapid inward migration caused by the early saturation of the corotation torque at the location of the ice line. At larger radii, the heat transition planet accretes at a slower rate and takes 2 Myr to reach its maximum mass. When the ice line and heat transition planets reach their maximum masses before the disk is dispersed, they proceed to evolve radially through Type-II migration for the remainder of the disk history. On the other hand, the dead zone planet does not reach its maximum mass by the time the disk disperses.

For the disk parameters shown in Table 5.2 we compute three planets with the final planetary mass and orbital radius shown in Table 2.4. We compute two Hot Jupiters and one sub-Earth mass planet, the former having a small spread in planetary mass and orbital radius while the latter represents a 'failed' core that never reached a sufficient mass to draw down an atmosphere.

In Figure 2.12 we show the cumulative minor gas abundances as a percentage of the total mass of

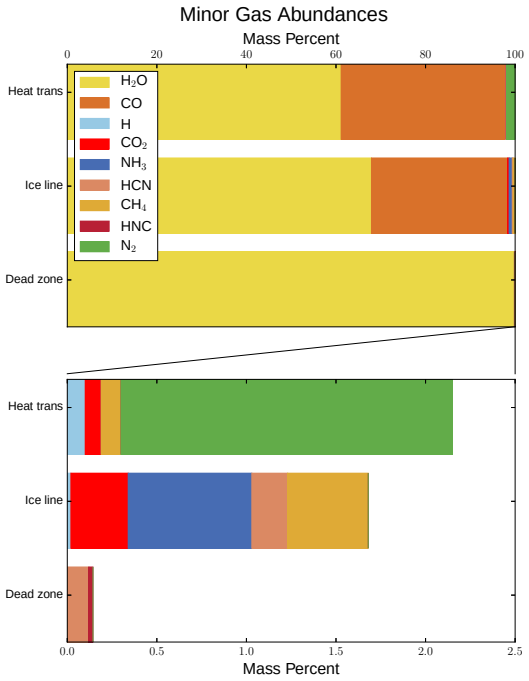

Figure 2.12: Mass percentage of most abundant gases other than H_2 and He. The bottom panel zooms into the gas species other than H_2O and CO. The heat transition and ice line planets show similar abundances in both H_2O and CO. The dead zone planet did not accrete an atmosphere, and the reported species are the most abundant ices that could contribute to an atmosphere through out gassing. It is exclusively dominated by water ice. The difference between the heat transition and ice line planets is in the nitrogen carriers, and is determined by *when* the planet undergoes unstable gas accretion (see Figure 2.11). At early times (when the ice line accretes) the nitrogen gas is primarily in NH_3 and HCN, while at later times the disk cools and the nitrogen content is dominated by N_2. The values are shown in Table 2.5.

Table 2.5: Minor gas abundance as percent of mass not in H2 and He. The dead zone atmosphere is populated by a theoretical out gassing of frozen material.

	Dead zone	Ice line	Heat transition
H2O	99.84	67.92	61.15
CO	< 0.01	30.40	36.70
H	< 0.01	0.02	0.1
CO2	< 0.01	0.32	0.09
N2	< 0.01	< 0.01	1.85
NH3	< 0.01	0.69	< 0.01
HCN	0.12	0.2	< 0.01
CH4	< 0.01	0.45	0.11
HNC	0.02	< 0.01	< 0.01

each planet formed in the three planet traps. These minor gas abundances are all gas species other than H_2 and He (which dominate the total mass of the planet, making up between 99.5% and 99.8% of the total mass). Only the gas species that have mass percentages greater than 0.01% of the total minor gas mass are shown (see Table 2.5 for numerical values). The dominant minor gases in our planets are CO and H_2O, owing to the high abundance of these molecules in the disk. For the dead zone planet which accreted no atmosphere, we have estimate an 'out gassed' atmosphere based on the amount of frozen material it accreted during the oligarchic growth phase. In producing Figure 2.12 we have assumed that all of the ice that is accreted is out gassed into an atmosphere.

The ratio between H_2O and CO in the atmospheres of gas giants is determined largely by the relative amount of those species in the gas phase where the planet rapidly draws down the majority of its gas (Phase 3 accretion). If this occurs outside the radial location of the ice line the majority of the water is in the ice phase rather than the gas phase. The dead zone planet underwent its oligarchic growth outside of the water ice line and within the CO ice line, hence its high abundance of water in its hypothetical atmosphere.

By contrast the abundance of the nitrogen carriers (primarily NH_3, N_2, HCN) show variation between the ice line planet (primarily NH_3 and HCN) and the heat transition planet (primarily N_2). This variation appears to depend on *when* the gas giant accretes its gas. As seen in Figure 2.11 the ice line accretes its gas very early in the disk evolution (prior to 1 Myr) while both the heat transition and dead zone accrete later than 1 Myr. As the disk ages the viscously heated regime of the disk cools and the gas phase nitrogen content of the disk is primarily converted to N_2 while species like NH_3 and HCN freeze out onto grains.

Figure 2.12 assumes that no chemical processing has occurred once the gas has accreted onto the planet. We call these atmospheres *early* atmospheres as they represent the chemical abundances of a homogeneous, passive atmosphere that has not had time to change the chemical abundances that it accretes during its formation. In what follows, when we compare the chemical results of our theoretical atmospheres to the observational data we also assume that there is no physical processing (vertical transport, atmospheric loss) of the atmosphere to change its chemical make up.

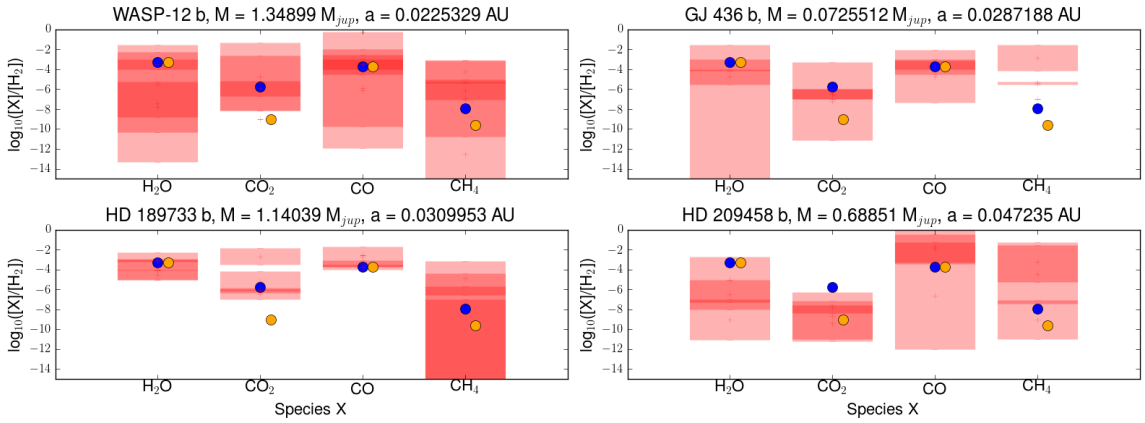

Figure 2.13: Mixing ratio $[X]/[H_2]$: the abundance of the molecule X over the abundance of molecular Hydrogen. The red bars denote the range of inferred mixing ratios from Madhusudhan & Seager (2009, 2010); Miguel & Kaltenegger (2014); Lee et al. (2012); Line et al. (2011, 2014a), where the darker opacities denote regions of overlap between different sources. The mixing ratios are shown in the colour denoted in Figure 2.11: Ice line (blue) and Heat transition (orange). The dead zone planet is absent from this comparison as it is not representative of a Hot Jupiter atmosphere.

2.6 Discussion

2.6.1 Comparison with the Observations

We wish to compare the computed chemical abundance of the atmospheres of our theoretical planets to the available retrieved abundances from observed planets. The atmospheric data has generally been obtained for Hot Jupiters with orbital seperations of a few hundredths of an AU (Lee et al. (2012), Lee et al. (2013), Line et al. (2011), Line et al. (2014a), Madhusudhan & Seager (2009), Madhusudhan & Seager (2010) and http://exoplanets.eu for orbital properties). The orbital radii of the ice line and heat transition planets (R$\sim 0.11, 0.15$ respectively) are an order of magnitude farther out than the planets available in the atmospheric data. Regardless, we will compare their atmospheric contents to the ones in the data because our theoretical planets could migrate into the orbital radii range of Hot Jupiters if the disk was allowed to evolve for longer than 4.1 Myr. Moreover, we assume that the chemical content of the atmosphere is unchanged once the planet reaches its maximum mass, because it no longer accretes any disk material and we do not evolve the atmosphere once it has been accreted onto the planet. Indeed, in a full population synthesis model one of the variable parameters is the lifetime of the disk, which can have a range of values as low as 1 Myr and as high as at least 10 Myr. A longer disk lifetime would also let the dead zone planet

accrete more matter which would allow it to collect an atmosphere. For this reason, the disk lifetime is one of the most important disk parameters to study in future work.

Figure 2.13 shows the range of inferred mixing ratios from observations (see Madhusudhan & Seager (2009, 2010); Miguel & Kaltenegger (2014); Lee et al. (2012); Line et al. (2011, 2014a)) and compares the range to our theoretically computed mixing ratios.

Generally speaking we see a good agreement for our computed models in the ice line and heat transition trap as well as the range of inferred ratios that had the highest agreement (darkest region) between observers. While we lack the statistical breadth of a full parameter search to fully understand the connection between our theoretical predictions and the observations, these results suggest that our early (non-processed) atmospheres are a good representation of the chemical make up of observed Hot Jupiter atmospheres. Variations between these early atmospheres and the observations have a variety of potential causes. This may include chemical processing in the atmosphere as well as mixing due to turbulent transport and atmospheric loss from a variety of sources. Only the chemical abundance of the upper atmosphere (down to one optical depth) of the planet can be observed through emission and transmission spectra. Thus the observable abundance of CH_4 and H_2O is sensitive to UV photolysis, while H_2O and CO_2 are sensitive to the efficiency of vertical mixing. Alternatively, molecules like CO appear to be unchanged when testing different UV flux and mixing efficiency (Miguel & Kaltenegger, 2014).

2.6.2 Elemental Ratios: C/O

The elemental ratio of an atmosphere is another probe for studying the chemical abundance and physical properties of exoplanetary atmospheres. The most relevant elements are Carbon and Oxygen because of their abundance and ease of detection. Nitrogen is a third important element however it has yet to be directly detected or inferred in the emission spectra of Hot Jupiters. The carbon-to-oxygen ratio (C/O) is a widely studied elemental ratio and is believed to track the approximate formation location of gas giant planets (Öberg et al., 2011).

The general picture assumes that the abundance of H_2O, CO_2 and CO are only determined by their condensation onto grains at each of their respective ice lines. If a gas giant accretes its gas inside the CO ice line but outside the ice lines of both CO_2 and H_2O then $C/O \sim 1$. If the planet accretes within the CO_2 ice line then $0.66 < C/O < 1$ depending on the relative abundance of CO_2 to CO with the lowest ratio requiring equal amounts of CO_2 and CO. CO_2 is rarely more abundant than

CO, as is the case for the chemistry outputs shown here. Within the water ice line a planet would accrete an elemental ratio $C/O \sim 0.5$ if H_2O and CO are equally abundant and CO_2 is negligible (as we see in our planets) and $C/O \sim 0.25$ if H_2O, CO_2 and CO are all equally abundant.

In our model the ice line and heat transition planets have $C/O = 0.227; 0.279$ respectively. The dead zone planet has an incredibly low $C/O \sim 0.001$ in its out gassed atmosphere. Both the heat transition and ice line planets have C/O of less than a third, due to the abundance of water over CO and the low abundance of CO_2. The difference in relative abundances and C/O appears to arise because the heat transition trap begins its gas accretion outside of the ice line, before moving within the location of the water condensation front where it accretes the vast majority of its gas. The planet that started forming in the water ice line began and ended its gas accretion within the ice line due to the early saturation of the corotation torque in the water ice line. Because of its early saturation, the ice line accretes more water (by mass) than the heat transition trap.

Again we see the importance of *where* and *when* the planet forms: the radial location of gas accretion sets the bulk of the carbon-to-oxygen ratio. We initialized our chemical code with the dominant chemical species computed from a chemical simulation of a molecular cloud. This initial condition has a C/O of 0.288 which is close to the C/O ratio of both planets. This suggests that the gas that each planet accreted had very little elemental processing prior to accretion. This processing depends on the physical conditions of the disk, and thus is sensitive to the radial location of the forming planet and the age of the disk.

2.6.3 Elemental Ratios: C/N

The Carbon-to-Nitrogen ratio has yet to be used for analyzing exoplanetary atmospheres. However it has been used to characterize the astronomical bodies in our solar system (for example, the review by Bergin et al. (2015)). Our sun has C/N ~ 4 while the Earth has an average ratio of ~ 49. This large discrepancy is likely caused by the Earth accreting material that had been thermally processed (Bergin et al., 2015). For the Hot Jupiter formed in the ice line trap we find C/N ~ 47. For the Hot Jupiter formed in the heat transition trap we find C/N ~ 10. Drawing the same conclusion as before, this discrepancy is caused by the thermal processing of the gas disk. This thermal processing is reduced as the disk cools, so C/N can be used as a measure of *when* the planet accretes its gas. High ratios suggest that the planet forms earlier in the disk lifetime. The ice line planet began its gas accretion at about 0.29 Myr into the simulation while the heat transition planet began accreting

gas at 1.13 Myr. From Figures 2.2 and 2.3 we can see that a significant amount of chemical evolution has taken place between these two starting points.

2.7 Conclusions

We have developed a method of linking the time dependent, non-equilibrium astrochemistry of accretion disks to the chemical abundances of exoplanetary atmospheres. With this model of a disk undergoing viscous evolution as well as photoevaporation, we have run 4.1 Myr lifetime model of a fiducial disk and planet formation model to produce a set of exoplanets in three basic planet traps. We find that:

- It contains condensation fronts of H_2O, CO_2, NH_3 and CO located at 3.5, 10, 30 and 62 AU at $t = 0.1$ Myr respectively, corresponding well with the inferred locations of the condensation fronts proposed to exist in HL Tau .
- We compute three planets with M = 2.67 M_{jup}, 1.43 M_{jup} and 0.003 M_{jup} and a = 0.11 AU, 0.15 AU and 3.7 AU in the ice line, heat transition and dead zone traps respectively.
- In these three traps we find an atmospheres with Carbon-to-Oxygen ratios (C/O) of 0.227, 0.279, 0.001 in the ice line, heat transition and dead zone traps respectively .
- Three planets were produced that had mixing ratios for CO, H_2O, CO_2 and CH_4, of 1.99×10^{-4}, 5.0×10^{-4}, $1.8\times10^{-6} \rightarrow 9.8\times10^{-10}$ and $1.1\times10^{-8} \rightarrow 2.3\times10^{-10}$ respectively. These correspond well with the mixing ratios inferred from observed emission spectra.
- C/O is largely influenced by the location of the accreting protoplanet with respect to the location of the water ice line when the planet accretes the majority of its gas.
- C/N is influenced by thermal processing of the accreted gas and is set by the location of the accreted gas and when the gas was accreted.
- The chemical abundance of the atmosphere depends on *where* and *when* the planet accretes its atmosphere. This is seen in both the carbon-to-oxygen ratio as well in the mass weighted abundances.
- Early (in time) accreters generally have their nitrogen content in the form of NH_3 and HCN, while the later accreters have their nitrogen in the form of N_2.

It is not clear if these results are representative of the full population of exoplanets, or are simply the result of our very limited sample of disk parameters. In future work, we will improve our methods by including dust growth, fragmentation, settling and radial transport into the radiative transfer model which will change the global ionization structure of the disk. Additionally we will perform a population synthesis study based on distributions of disk lifetimes and initial masses in order to develop a statistical treatment of planetary atmospheres.

Chapter 3

Radial Drift of Dust in Protoplanetary Disks: The Evolution of Ice lines and Dead zones

What follows has been published in Monthly Notices of the Royal Astronomical Society (MNRAS). See: Cridland, Pudritz & Birnstiel 2017. MNRAS **465**: 3865.

Abstract

We have developed a new model for the astrochemical structure of a viscously evolving protoplanetary disk that couples an analytic description of the disk's temperature and density profile, chemical evolution, and an evolving dust distribution. We compute evolving radial distributions for a range of dust grain sizes, which depend on coagulation, fragmentation and radial drift processes. In particular we find that the water ice line plays an important role in shaping the radial distribution of the maximum grain size because ice coated grains are significantly less susceptible to fragmentation than their dry counterparts. This in turn has important effects on disk ionization and therefore on

the location of dead zones. In comparison to a simple constant gas-to-dust ratio model for the dust as an example, we find that the new model predicts an outer dead zone edge that moves in by a factor of about 3 at 1 Myr (to 5 AU) and by a factor of about 14 by 3 Myr (to 0.5 AU). We show that the changing position of the dead zone and heat transition traps have important implications for the formation and trapping of planets in protoplanetary disks. Finally, we consider our results in light of recent ALMA observations of HL Tau and TW Hya.

3.1 Introduction

Dust plays a key role in the physics of protoplanetary disks, and hence the physics of planet formation. The largest grains most strongly contribute to the disk's opacity while the smallest grains provide the most surface by mass for the freeze out of volatiles. So understanding the evolution of the grain sizes and dust surface density will have an impact on the abundance of volatiles and free electrons in the disk, and hence our understanding of planet formation and the accretion of planetary atmospheres.

In the absence of small scale instabilities (for example: streaming instability (Youdin & Goodman, 2005; Raettig et al., 2015) and zonal flows (Johansen et al., 2011)) the dust grain sizes and surface density evolve through coagulation (Dullemond & Dominik, 2005), fragmentation (Blum & Wurm, 2000), and radial drift (Whipple, 1973; Weidenschilling, 1977).

These are competing processes, with rates that depend on the size of the grain and the density of the surrounding gas. It has been shown (eg. in Birnstiel et al. (2012)) that these processes can be modeled by simple analytic functions, and their relative relevance can be determined by comparing their physical timescales. This has been implemented in the 'two-population dust' model of Birnstiel et al. (2012) and used to reproduce the observed properties of protoplanetary disks (ie Birnstiel et al. (2015)).

The purpose of this work is to combine an evolving astrochemical model of protoplanetary disks with a model for an evolving dust mass distribution. We show that a more complete model of dust physics which includes coagulation, fragmentation and radial drift, produces an ionization structure which evolves in a different manner than in a fiducial dust model with a constant dust-to-gas ratio. This new ionization structure has implications on the size and evolution of the disk's dead zone and ultimately on the formation history of planets forming within the disk. For instance in determining the radial migration rate of a forming planet, the net torque acting on the planet depends on its

location relative to the edge of the dead zone.

The relevant background information is presented in §3.2. In §3.3 the 'two-population dust' (Two-pop-dust) model of Birnstiel et al. (2012) (or see Birnstiel (2016)) and the astrochemical disk model from Cridland et al. (2016) are presented. In §3.4 we will demonstrate that the ice line causes an amplification of dust surface density within its location and that this new dust surface density distribution changes how the dead zone evolves as the disk ages. We will also compare this new evolution and structure of the dead zone with the structure of the dead zone from the simpler model. In §4.6 we discuss the implications that the new model on planet formation and present our conclusions.

3.2 Background

3.2.1 Dust, ionization, and the impact on planet formation

The grain size and surface density distribution of the dust affects the ionization structure of the disk. In the Rayleigh limit of Mie theory, the efficiency of absorption and scattering of radiation scales as a power law with the size of the dust grain (Tielens, 2005). So the amount of ionizing radiation that penetrates into the disk depends on the rate of dust coagulation versus dust fragmentation. Radial drift plays an important role in the retention of these large grains because the sub-Keplarian orbits that are imposed on the largest grains by gas drag accretes these grains faster than viscous evolution alone (Weidenschilling, 1977; Brauer et al., 2008; Birnstiel et al., 2010). We expect that the radial structure of the disk's ionization will be sensitive to the concentration of large dust grains that are present through the disk, hence on the efficiency of radial drift. Fragmentation impacts this efficiency by limiting the maximum size of the grains at different radii.

Generally there is an inner region of the disk that is dominated by thermal ionization, an intermediate region where the ionization is low, and an outer region of radiation dominated ionization at larger radii (Gammie, 1996; Matsumura & Pudritz, 2003). We assume that disk turbulence is produced through the magnetorotational instability (MRI, Balbus & Hawley (1994)), which relies on a coupling of the disk's magnetic field with the electrons in the gas. This region of low ionization leads to weak MRI driven turbulence and is called the 'dead zone' (Gammie, 1996; Matsumura & Pudritz, 2003; Dutrey et al., 2014). The point where one region transitions to the other - the 'edge' of the dead zone - has important implications on planet formation via the combination of the core

accretion (Ida & Lin, 2004) and 'planet trap' models (Masset et al., 2006; Hasegawa & Pudritz, 2010; Lyra & Mac Low, 2012; Hasegawa & Pudritz, 2013; Cridland et al., 2016).

The planet trap model of planet migration focuses on the fact that there are inhomogeneities in the physical properties of accretion disks (ie. temperature, opacity) that slow the rate of planetary migration via Type I migration (Masset et al., 2006; Hasegawa & Pudritz, 2013). We assume that a planet that is trapped will always be located at the radial location of the planet trap until the planet has grown massive enough to open a gap and begin Type-II migration. The edge of the dead zone acts as one of these planet traps (Matsumura & Pudritz, 2003), so accurately modeling the dust physics has implications on where a growing planet will form.

The number of small grains also impact the ionization structure of the disk because they offer the highest surface area per mass of dust for the freeze out of volatiles, and the capture of electrons. If fragmentation was inefficient, the number of small grains is quickly reduced (Dullemond & Dominik, 2005), eliminating an important sink for electrons. In our work, we assume that the grains are either singly charged, or neutral. A dust grain capturing a single electron is a good assumption for the smallest grains (Akimkin, 2015) but becomes a worse assumption for larger grains because they can efficiently capture multiple electrons (Akimkin et al., 2015). Under this assumption as the average grain size grows, the total surface area available for electron capture is reduced, causing the ionization to increase throughout the disk. It is currently unclear what the effect of multiple electron capture has on the global ionization structure of the disk, and this is beyond the scope of this work.

3.2.2 Limiting the dust grain size

The maximum dust grain size at a given orbital radius is limited by two processes: radial drift (Whipple, 1973; Weidenschilling, 1977) and fragmentation (Blum & Wurm, 2000; Dullemond & Dominik, 2005). The maximum grain size of a population is set by radial drift when the drift rate of a large grain a_{max} is equal to its growth rate from the population of smaller grains. Any grain larger than a_{max} will accrete onto the host star faster than it can be built from the coagulation of smaller grains (Birnstiel et al., 2012). Similarly, the maximum size is limited by fragmentation when the fragmentation rate of a large grain is equal to its growth rate. Globally, the size distribution of the dust in protoplanetary disks is set by these barriers, and their impact has begun to be observed by the Atacama Large Millimeter Array (ALMA) (Pérez et al., 2012; ALMA Partnership et al., 2015; Zhang et al., 2015; Andrews et al., 2016; Tazzari et al., 2016).

The shape of the dust size distribution can be described by a broken power law (see below), whose functional form has been motivated by observations (Mathis et al., 1977) and reproduced by numerical simulations (Dullemond & Dominik, 2005; Brauer et al., 2008; Birnstiel et al., 2012). This power law extends from the smallest grain of approximately 0.1 microns up to a maximum grain size that is set by the physical barriers described above. In protoplanetary disks, it has been shown that fragmentation and coagulation produces a maximum grain that varies with disk radius as a broken power law (Birnstiel et al., 2011).

A difference between the two barriers is how they impact the surface density of the dust. The fragmentation of the largest dust grains does not remove any dust mass from the disk, it simply redistributes the dust surface density from the largest grains to the smaller ones (Dullemond & Dominik, 2005). Conversely radial drift does reduce the surface density of dust, by forcing the largest dust grains into sub-Keplerian orbits which spiral into the host star (Weidenschilling, 1977). This difference can be seen when comparing the evolution of the surface density distribution of the dust in simulations that do not have radial drift (Dullemond & Dominik, 2005) with those that do (Brauer et al., 2008).

The efficiency of grain fragmentation is dependent on the layer of ice that forms on the grain outside the water 'ice line' of the disk (Birnstiel et al., 2009, 2010; Banzatti et al., 2015). The water ice line defines the location in the disk where the water content transitions between being primarily in the vapour phase, to being primarily in the ice phase. At radii outside the location of the ice line the grains will be strengthened by their ice content, while within the ice line the grains are weaker since the water content is in the vapour phase.

The dry grains will generally be weaker and hence susceptible to fragmentation compared with grains outside the ice line, and hence they will radially drift slower. This less efficient radial drift means that there will be an enhancement of dust surface density within the ice line because it will not be cleared out as fast as it would if the fragmentation rate was constant (Birnstiel et al., 2010).

3.2.3 Linking dust grain size and astrochemistry

In what follows, the global structure of the ionization will be shown to depend on the dust, through physical processes like fragmentation, radial drift and coagulation. The effect of grain size on astrochemical networks is through the availability of dust grains on which gas species freeze, as well as the availability of grains to capture electrons; thereby reducing the disk's ionization. Numerically,

its effect is parameterized with a code parameter known as the 'freezing efficiency' which depends on the average size of the dust grains as computed by our dust model. Hence the freezing efficiency will have a radial dependence on the number and size distribution of dust grains.

3.3 Method

Generally, our method is as follows: first we produce the gas surface density and temperature radial distribution based on the analytic model of Chambers (2009). This model assumes that the gas temperature can be described by three power laws depending on the heating source and temperature dependence of the disk's opacity. In the inner region (T > 1380 K) of the disk where the dust sublimates, the disk opacity varies as a power law in temperature. At lower temperatures we assume that the opacity is constant. The disk is heated by two sources: viscous heating caused by the accretion process, and direct irradiation from the host star.

Second we compute the surface density radial distribution of the dust based on either of our two dust models below. The CPA16-dust model assumes that gas and dust are perfectly mixed with a constant gas-to-dust ratio, while the Two-pop-dust model computes the coagulation, fragmentation, and radial drift of dust grains. Both dust models assume that the gas evolves in the same way, set by the gas model presented in Cridland et al. (2016). In principle the gas evolution will depend on the evolution of the dust, however we are primarily interested in how the ionization state of the gas depends on the dust model. And hence we assume that the gas evolution is not affected by changes in the radial and size distribution of the dust grains.

Next we compute the UV and X-ray radiation field in the disk using RADMC3D and the results from the gas and dust models. This Monte Carlo radiative transfer scheme use 10^7 photon packets to compute the radiation field. The flux of this ionizing radiation is sensitive to the choice of opacity tables, we use the optical constants of Draine (2003), and compute the opacity using the on-the-fly method of RADMC3D.

Finally, we compute the chemical distribution with the radiation field, gas and dust volume density and temperature as inputs. The chemical structure is computed over 300 'snapshots' of the disk across 4.1 million years of disk evolution. Each snapshot represents the disk at individual times throughout the disk's life time, evenly space between 0.1 - 4.1 million years. Of particular importance to this work is the distribution of free electrons, as they are responsible for the coupling

to the magnetic field that leads to turbulence.

3.3.1 CPA16-dust Model

In Cridland et al. (2016) (CPA16) we used the analytic disk model of Chambers (2009) and a constant dust-to-gas ratio of 0.01 to describe the radial distribution of the dust. Built into this model (CPA16-dust) is the assumption that the dust surface density perfectly traces the surface density of the gas and the two fluids are fully mixed.

The Chambers (2009) disk model is a self-similar solution to the diffusion equation, which results in a power law for the surface density of gas and dust: $\Sigma \propto R^s$. The value of the exponent s is determined by the heating details, which results in three regions: evaporative, viscous and radiative. At temperatures below the evaporation temperature of silicate grains ($\sim$ 1380 K) we assume that the average opacity is constant in the disk. At higher temperatures, in the evaporative region, the opacity varies with temperature as a power law. The evaporative and viscous regions are heated through the viscous stresses in the gas caused by the disk's mass accretion while the radiative region is heated through the direct illumination from the host star. For a more detailed discussion of our disk model see CPA16 or Alessi et al. (2017).

A constant opacity through the disk is an over simplified assumption considering the dust model below. However more complicated analytic models (ie. Stepinski (1998)), which include a temperature dependence of the opacity show minimal deviations in temperature and surface density profiles when compared to the model presented in CPA16. Additionally, these models ignore the evolution of the size distribution and surface density of dust as the disk ages. A full analytic description of the opacity which includes the effect of dust evolution has yet to be developed, and we require an easily computed disk model to combine the dust evolution, radiative transfer and astrochemistry.

3.3.2 Two-pop-dust Model

To compute the dust evolution with the Two-pop-dust model we modified the algorithm that was developed by Birnstiel et al. (2012) so that the gas component evolved according to the analytic model of Chambers (2009). This allows us to directly compare the resulting ionization structure due to the variations in dust evolution between the two models, rather than the gas evolution.

A key component of the Two-pop-dust model is determining the size distribution of the dust

grains. As mentioned before, the maximum grain size is set by an equilibrium between either fragmentation or radial drift with coagulation. Once the maximum grain size is determined, the size distribution up to the maximum size can be described reasonably well by a power law

$$n(m)dm = Am^{-\alpha}dm, \tag{3.1}$$

where A and α are positive constants (Dohnanyi, 1969; Tanaka et al., 1996; Makino et al., 1998). These constants depend on whether fragmentation and radial drift dominates the evolution of the largest grains (Birnstiel et al., 2011). In the region dominated by fragmentation the maximum grain size is given by (Birnstiel et al., 2012):

$$a_{max} = a_{frag} \propto \frac{\Sigma_g}{\rho_s \alpha} \frac{u_f^2}{c_s^2}, \tag{3.2}$$

where Σ_g is the surface area of the gas, ρ_s is the average density of the dust grains, α is the turbulent parameter (Shakura & Sunyaev, 1973), c_s is the gas sound speed and u_f is the collision speed above which particle collisions lead to fragmentation (Birnstiel et al., 2012).

The second constraint on the maximum size of the grain is the rate of radial drift. Birnstiel et al. (2012) showed that the maximum grain size in the radial drift dominated regime is given by:

$$a_{max} = a_{drift} \propto \frac{\Sigma_d}{\rho_s} \frac{V_k^2}{c_s^2} \gamma^{-1} \tag{3.3}$$

where Σ_d is the surface density of the dust, V_k is the Keplarian velocity and

$$\gamma = \left| \frac{d \ln P}{d \ln r} \right|, \tag{3.4}$$

is the absolute value of the power-law index of the gas pressure profile (Birnstiel et al., 2012).

The Two-pop-dust model has been calibrated to the numerical result of Birnstiel et al. (2010), which included coagulation, fragmentation and radial drift. This simpler model computes the coagulation and fragmentation processes between only two populations of grains, one small (monomer) size and one larger size. Once the total surface density is computed, the size distribution of the grains is reconstructed based on the result of Birnstiel et al. (2015). This model benefits from an increase in computational efficiency because only two sizes are resolved, and well reproduces the dust

surface density evolution.

In choosing a value for u_f we follow the work of Birnstiel et al. (2010). Within the ice line the grains are not covered with ice, and have a fragmentation threshold speed of 1 m/s (Blum & Wurm, 2008b). Outside of the ice line the grains are strengthened by a layer of ice, resulting in a fragmentation threshold speed of 10 m/s (Gundlach & Blum, 2016).

In CPA16 the ice line was defined as the disk radius at which half the water vapour had been converted to water ice. However the ice line is in fact a region of space with a width of a few tenths of AU (see CPA16, their Figure 6). Within this transition region the grains will not be perfectly covered in ice, and we assume that the covered fraction of the grain corresponds with the ratio of water ice at any time to the final water ice abundance. Additionally we assume that the grain is strengthened by an increase in the ice coverage, so that the fragmentation threshold speed varies smoothly with the ice coverage of the grains (see Equation 3.5).

This assumption ignores the effects of sintered grains. Sintering is the process of sticking grain aggregates together at temperatures below the sublimation temperature of specific volatiles. Sintered grains are characterized by frozen 'necks' that connect the aggregates (eg. Sirono (2011)). These necks can actually *weaken* the grains during collisions because they cannot dissipate collisional energy into deformation. Instead, sintered grains will tend to fragment at lower collisional speeds than their unsintered counterparts. It has been suggested that sintering regions around the sublimation point of a few volatiles can explain the dust emission observed in HL Tau (Okuzumi et al., 2016). In their work, there is no difference between the fragmentation threshold speed in the inner regions of the disk and the regions outside of the ice line. Instead, the fragmentation threshold speed is modified within the sintering regions of every major volatile in the disk. Additionally, around the edge of the ice line there is little qualitative difference between the dust distribution in a sintering model and the distribution we will compute in this work.

Our choice of fragmentation threshold speed differs from the work of Okuzumi et al. (2016). In their work the threshold speed is 20 m/s and 50 m/s in the sintered and unsintered regions respectively. The unsintered region would be equivalent to our ice-covered region where $u_f \sim 10$ m/s, while their sintered region would be equivalent to the transition region where u_f is a function of radius. These higher threshold speeds are generally attributed to sub-micron sized grains and are based on the numerical results of Schäfer et al. (2007) and Wada et al. (2009). As the grain grows, lab experiments have shown that the threshold speed decreases with increasing grain size

(Beitz et al., 2011) because the strength and porosity of the grain becomes more important. We follow Birnstiel et al. (2012) in choosing a threshold speed of 10 m/s to act as a global average for the majority of the dust that is covered in ice.

The smooth transition between low and high threshold speeds is modeled with an arctan function of the form:

$$u_f(r) = a + b \arctan\{c \cdot (r - r_0)\}/\pi. \tag{3.5}$$

The parameter r_0 is the center of the arctan function and roughly matches the location of the water ice line as defined in our previous work. The three other constants (a, b and c) are fit so that $u_f(r << r_0) \sim 1$ m/s, $u_f(r >> r_0) \sim 10$ m/s, and the function transitions at the same rate as water transitions between the vapour and ice phases.

We fit Equation 3.5 so that its slope is nearly the same as the slope of the water ice radial distribution from our fiducial disk model in CPA16 and find that the fitting parameters do not vary between the three times. The only parameter that varies in time is the radial location of the middle of the function (r_0). This is not surprising since the location of the ice line evolves as the disk ages, moving inward as the disk cools. We find that the position of r_0 traces a disk temperature of approximately 140 K which is just below the sublimation temperature of water. For this reason we define $r_0 \equiv r(T = 140$ K). For the fiducial disk we find that the fitting constants have average values of $a = 5.47$ m/s, $b = 9.11$ m/s, and $c = 15$. These fitted values result in the limits $u_f(r >> r_0) = 10.025$ m/s and $u_f(r << r_0) = 0.915$ m/s.

3.3.3 Radiation Field

We use RADMC3D (Dullemond, 2012) to compute the local X-ray and UV fields for our astrochemical model. RADMC3D is a Monte Carlo radiative transfer scheme that can handle the presence of multiple dust populations, by computing the wavelength dependent opacities of each grain population on the fly. In the CPA16-dust model we assume that the dust and gas are well mixed so that the scale height of the dust is the same as the gas. For the absorption and scattering opacities we use the pre-computed values from Weingartner & Draine (2001) and Bethell & Bergin (2011a). In the Two-pop-dust model we used the on-the-fly method of calculating the dust opacities using the real and complex indices of refraction computed by Draine (2003) and assumed Mie scattering.

We sampled the dust distribution produced with the Birnstiel et al. (2012) code with 20 different grain sizes equally spaced in log-space. Their surface densities are normalized so that the total dust surface density remained the same after the sampling. We converted the dust surface densities to volume densities (the preferred input of RADMC3D) by assuming an equilibrium between vertical turbulent mixing and gravitational settling. This assumption results in a simple conversion where (Dubrulle et al., 1995; Hasegawa & Pudritz, 2010):

$$\rho_d(a,r,z) = \frac{\Sigma_d(a,r)}{\sqrt{2\pi}H_d(a,r)} \exp\left\{-\frac{z^2}{2H_d^2}\right\}. \tag{3.6}$$

Σ_d is the surface density outputted from the Birnstiel et al. (2012) code as a function of dust radius a and orbital radius r. The scale height of the dust (H_d) also depends on the size of the dust grain and position in the disk:

$$\frac{H_d(a)}{H} = \frac{\bar{H}}{\sqrt{1+\bar{H}}}, \tag{3.7}$$

where H is the scale height of the gas (Hasegawa & Pudritz, 2010). The unitless number $\bar{H}$ is given by:

$$\bar{H} = \left(\frac{1}{1+\gamma_{turb}}\right)^{1/4} \sqrt{\frac{\alpha\Sigma_g}{\sqrt{2\pi}\rho_s a}}, \tag{3.8}$$

where ρ_s is the bulk density of the dust, Σ_g is the surface density of the gas, and γ_{turb} is the exponent in the turbulent energy spectrum: $E(k) \propto k^{-\gamma_{turb}}$ where k is the wavenumber. Generally γ_{turb} has a value of between 5/3 and 3 (Dubrulle et al., 1995), however our results are not sensitive to the choice of γ_{turb} because of how weakly $\bar{H}$ depends on γ_{turb} (see Equation 3.8). We choose a value of 5/3 which is the classic Kolmogorov type of isotropic and incompressible turbulence.

The above solution assumes that the grain stopping time $\tau_s \equiv \rho_s a/\rho c_s$ is vertically constant, and ρ is the midplane gas density: $\rho \equiv \Sigma_g/\sqrt{2\pi}H$. This assumption is most relevant for large grains ($\Omega\tau_s \lesssim 1$) because they occupy the *strong settling limit* $H_d << H$ (Fromang & Nelson, 2009) and variations in τ_s can be neglected. For smaller grains ($\Omega\tau_s << 1$), the assumption breaks down because more grains are vertically extended and hence variations in τ_s become more important. The different vertical distributions do not result in major differences in the midplane ionization because it depends on the total vertical optical depth of the disk which is not affected by settling.

Fromang & Nelson (2009) have demonstrated the breakdown of the above assumption in global MHD simulations of stratified protoplanetary disks. In that work, they showed that the Gaussian shape for the vertical distribution of dust overestimates the amount of dust at $z > 2H$ when compared to their simulated distribution for all grain sizes. However the overestimation was worse for the smaller grains than for the large ones. Fromang & Nelson (2009) suggested that the deviation from Gaussian was due to a break down of the constant stopping time assumption as well as the stratified vertical structure of the gas in their simulations, which resulted in a turbulent diffusion coefficient that varied with height.

The complexities that are afforded by a global MHD simulations are beyond the scope of this work, however we note that an overestimation of the density of dust at $z > 2H$ implies an overestimation of the total opacity at those heights. This would results in a lower flux of ionization radiation at the midplane at large radii, especially early on in the disk lifetime when the dust is most extended. These discrepancies will be less important as the disk evolves and the gas density is reduced and more dust settles to the midplane.

3.3.4 Disk Chemistry and Ionization

To compute the ionization structure we use a non-equilibrium photochemical code as described in Fogel et al. (2011) and CPA16. The code computes the astrochemistry for a disk irradiated by X-ray and UV radiation. Chemistry is primarily driven by ion-neutral reactions in the gas phase and is catalyzed by the presence of dust grains. Additionally, there are two grain surface reactions for the formation of water and molecular hydrogen. As well as catalyzing gas phase reactions, the grains impact the ionization structure by acting as a sink to electrons. Cosmic ray and X-ray ionization drives the chemistry by creating ions and free electrons. These free electrons also couple to the magnetic field which produces turbulence via the MRI.

We use a standard ionization rate of 10^{17} s^{-1} per H_2 for the cosmic rays and an assumed luminosity of 10^{30} erg/s for the X-rays. We model a range of X-ray wavelengths between 1 and 20 keV using a template spectrum for a T Tauri star. Some recent work (ex. Cleeves et al. (2014, 2015)) has suggested that disk observations are consistant with lower cosmic ray ionization rates, which could lead to a larger dead zone. While we do not explore this effect we do find that the dead zone location is sensitive to the size and density distribution of the dust, which suggests that the X-ray radiation field is having a significant impact on the gas ionization.

We compute an average dust grain size, weighted by the freezing efficiency parameter of the chemical code. The freezing efficiency parameter has the form: $fe(a) = (a/0.1\mu\text{m})^{-3/2}$ and the average freezing efficiency is:

$$\bar{fe}(r) = \frac{\int_{a_{min}}^{a_{max}} n(a, r, z = 0) fe(a) da}{\int_{a_{min}}^{a_{max}} n(a, r, z = 0) da} \tag{3.9}$$

where $n(a, r, z = 0)$ is the number density distribution at the midplane. Hence the size of the average grain is:

$$\bar{a}(r) = 0.1\mu\text{m} \cdot \bar{fe}(r)^{-2/3} \tag{3.10}$$

In past works (eg. Fogel et al. (2011)) the freezing efficiency is assumed to be a global property of the disk, and variations in height and radii are ignored. Here we allow the freezing efficiency to vary as a function of radius while ignoring variations above the midplane. This underestimates the freezing efficiency of the grains at $z \gtrsim H$ which are smaller on average than at the midplane and could result in higher ionization at $z \gtrsim H$ because the efficiency of electron capture onto the grains is underestimated.

This average grain size and its freezing efficiency represent the average effect of the full size distribution in an attempt to minimize computational complexity. Every additional grain size added to the chemical model would require its own set of freezing, and grain surface reactions. For this reason, simply doubling the number of grains in the chemical model (two sizes instead of one) would nearly double the number of chemical reactions in the model. This larger set of reactions would require longer computation times to determine the final solution.

We have made no changes to the chemical code of Fogel et al. (2011), and have tested our implementation with RADMC3D against some general astrochemical properties like condensation fronts (CPA16). Our method is to compute the dust surface density profiles for grain sizes between 0.1 μm to 200 cm in 100 bins that are spaced equally in logspace. We then interpolate the surface densities down to 20 bins, normalizing so that the total surface density is the same as before. On this smaller binned sample we compute the radiation field using RADMC3D. We use the results of the dust calculation to estimate the average grain size that is used by the chemical code.

The Ohmic Elsasser number is a unitless parameter that traces the level of ionization and is

used to infer the location and extent of the dead zone (Fromang, 2013). It is defined as the ratio between the dissipation timescale and the growth timescale of the most unstable MRI mode. The critical value of this ratio which denotes the transition between turbulently dead and turbulently active regions is 1. This value is physically motivated as it represents an equilibrium between the growth and dissipation of turbulent energy (Gammie, 1996). It has also been shown in numerical simulations that an Ohmic Elsasser number of 1 represents a transition point between strong MRI driven turbulence and either weak or decaying turbulent solutions (Turner et al., 2007).

We connect the level of ionization from the results of the astrochemical code to the location of the dead zone using the Ohmic Elsasser number. It has the form of:

$$\Lambda_O \equiv \frac{\tau_{diss}}{\tau_{grow}} = \frac{v_{A,z}^2}{\eta\Omega}. \tag{3.11}$$

In this expression the Alfvén speed in the z-direction is $v_{A,z} \equiv B_z/\sqrt{4\pi\rho}$, where ρ is the gas density, Ω is the orbital frequency, η is the Ohmic resistivity and B_z is the local magnetic field in the z-direction (Gressel et al., 2015; Cridland et al., 2016). It has been shown (Bai & Stone, 2011) that at equipartition in a protoplanetary disk the ratio of the gas pressure to the magnetic pressure (the 'plasma beta', β) is related to the turbulent parameter α through: $\beta \sim 1/2\alpha$. Using this relation, we relate the local magnetic field to measurable fluid quantities

$$\begin{aligned} \beta \equiv \frac{P_{gas}}{P_{mag}} &\sim \frac{1}{2\alpha} \\ \frac{2 \cdot 4\pi\rho c_s^2}{B^2} &\sim \frac{1}{2\alpha} \\ B^2 &\sim 4 \cdot 4\pi\alpha\rho c_s^2 \end{aligned} \tag{3.12}$$

where we assume that the magnetic field energy is dominated by the z-component of the field. This has been observed to within a factor of order unity in simulations of MRI (Bai & Stone, 2011). This factor does not drastically change the location of the dead zone in our model. Finally the Ohmic Elsasser number is:

$$\Lambda_O = \frac{v_{A,z}^2}{\eta\Omega} = \frac{4c_s^2}{\eta\Omega} \tag{3.13}$$

The Ohmic resistivity is connected to the disk's ionization through (Kunz & Balbus, 2004):

$$\eta = \frac{234 T^{1/2}}{x_e} cm^2 s^{-1}, \tag{3.14}$$

where T is the temperature and x_e is the electron fraction - the ratio of electrons to hydrogen atoms. We assume that a dead zone exists in regions of the disk where $\Lambda_O < \Lambda_{O,crit} \equiv 1$. In computing the Ohmic Elsasser number in Equation 3.11 we assume that the turbulent parameter is constant throughout the disk. Reducing α at radii where $\Lambda_O < \Lambda_{0,crit}$ does not change our inference of where the dead zone edge is located.

In discussing a varying turbulent α it should be pointed out that there is a difference between the *turbulent* α and the *effective viscosity* (EV) α , which we assume is constant. The turbulent α describes the rate of angular momentum transfer due to turbulence. While the EV α describes the angular momentum transport through the disk, which can be caused by turbulence, disk winds, and spiral density waves.

A constant EV α is a current limitation of our disk model, and hence we assume that $\alpha_{EV} \equiv \alpha_{turb} + \alpha_{wind} =$ constant. This assumption corresponds to a constant (in radius) mass accretion rate throughout the disk.

3.4 Results

To demonstrate the impact of the dust distribution on the ionization structure we compute the radiation field, astrochemistry, and ionization in the CPA16-dust and Two-pop-dust models at 0.1, 1.3 and 3.7 Myr for the fiducial gas disk model from Cridland et al. (2016) (see Table 5.2 for disk

Table 3.1: CPA16 disk model parameters

Parameter	Value	Notes
$M_{disk}(t=0)$	0.1 $M_\odot$	Initial disk mass
$s_{disk}(t=0)$	66 AU	Initial disk outer radius
M_{star}	1.0 $M_\odot$	Stellar mass
R_{star}	3.0 $R_\odot$	Stellar radius
T_{star}	4200 K	Stellar effective temperature
α	0.001	Turbulent parameter
t_{life}	4.10 Myr	Disk lifetime
L_{xray}	10^{30} erg/s	Total X-ray luminosity

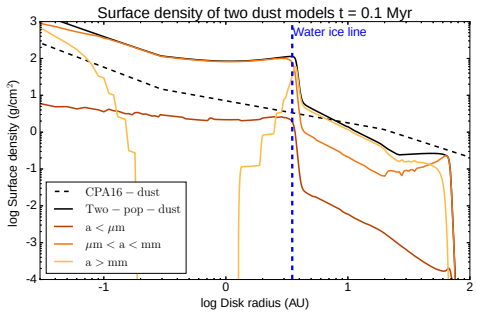

(a) t = 0.1 Myr

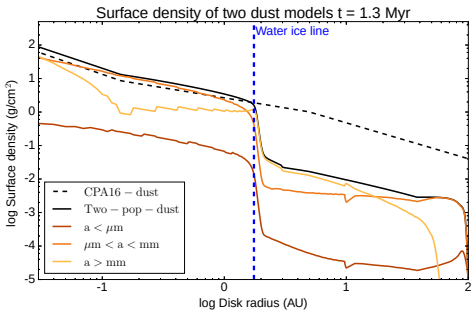

(b) t = 1.3 Myr

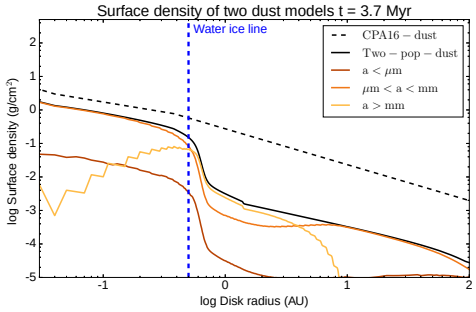

(c) t = 3.7 Myr

Figure 3.1: Total surface density (solid and dashed black lines) for the two dust models that were investigated. The coloured lines represent the total surface density of binned dust grain sizes that has been estimated by the Two-pop-dust model. The blue dashed line denotes the location of the water ice line. The largest grains show a depletion within the ice line where fragmentation becomes more efficient.

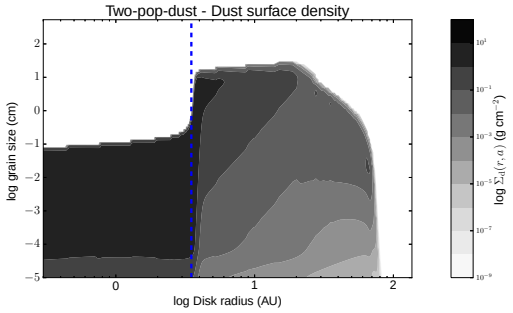

(a) t = 0.1 Myr

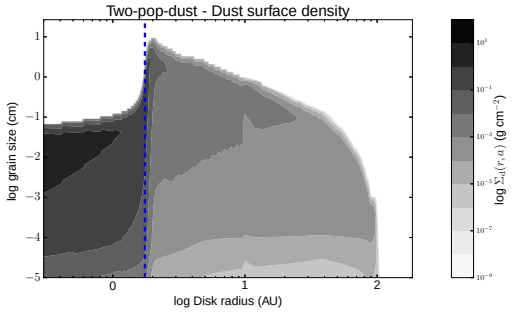

(b) t = 1.3 Myr

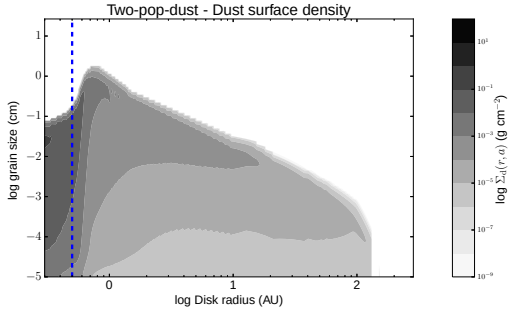

(c) t = 3.7 Myr

Figure 3.2: 2D representation of the estimated dust surface density for the different grain sizes in the Two-pop-dust model as a function of radius. We can clearly see a drop in the maximum grain size of over two orders of magnitude at the ice line (denoted by the blue dashed line).

model parameters). These times are meant to represent the disk at its early, middle and late ages.

3.4.1 Dust Surface Density Radial Distribution

In Figures 3.1(a), 3.1(b) and 3.1(c) we show the radial dependence of the total surface density of the dust in both models. We find the same qualitative behaviour as previous works where the surface density is enhanced at the ice line (denoted by the blue dotted line) by more than an order of magnitude. This enhancement is caused by a lower maximum grain size within the ice line because the fragmentation threshold speeds have dropped by an order of magnitude. The enhancement of the dust surface density and the retention of the dust is important for planet formation as it results in higher accretion rates during the early stages of solid accretion which will impact the final mass and evolution of forming planets. We will explore this particular facet of this problem in a later paper.

Figures 3.1(a), 3.1(b) and 3.1(c) also show the radial distribution of different grain sizes that are inferred by the Two-pop-model by reconstructing the size distribution based on the results of Birnstiel et al. (2015). In the figure, the grain sizes have been binned into sub-micron, micron to sub-millimeter and greater than millimeter. We find that the large grains are depleted within the ice line due to fragmentation and radial drift, while they tend to dominate the surface density at large radii and early times. As the disk ages these large grains radially drift inwards, depleting the solid density at the most distant radii. This depletion moves large grains to smaller radii, within the ice line, where they replenish the surface density of the large grains. Within the ice line the solid mass is dominated by micron to millimeter sized grains at all times. This size range also dominates the dust mass at large radii and late times.

In Figures 3.2(a), 3.2(b) and 3.2(c) we show the dust surface density (gray scale) as a function of grain size and disk radius. On the gray scale, white denotes the region of the plot where a grain size is not populated by any surface density. We see that the maximum grain size that is populated by surface density drops by up to two orders of magnitude across the water ice line (blue dashed line). The radial dependence of the maximum grain is set by Equations 3.2 and 3.3 and depends on which process limits the maximum grain. This drop in grain size is the important aspect that leads to the longer retention of dust in protoplanetary disks. Birnstiel et al. (2012) showed that the radial drift timescale $\tau_{drift} = r/u_D \sim 1/a$, which implies that a drop in the maximum grain size of two orders of magnitude leads to an increase in the radial drift timescale of two orders of magnitude. This increase in the radial drift timescale is a feature of the dust physics that can lead to the longer

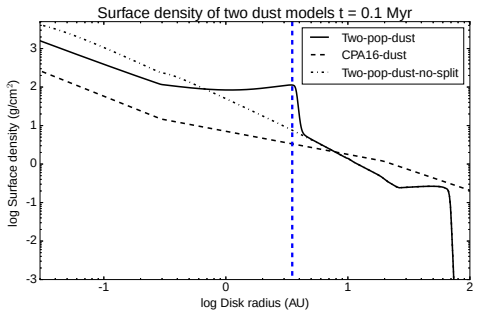

(a) t = 0.1 Myr

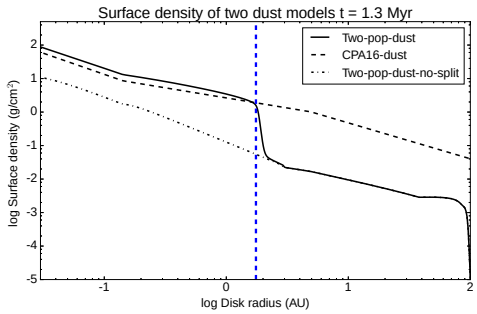

(b) t = 1.3 Myr

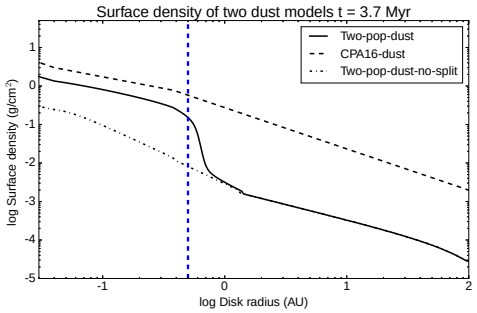

(c) t = 3.7 Myr

Figure 3.3: Radial dependence of total dust surface density in the CPA16-dust (dashed), Two-pop-dust (solid), and Two-pop-dust-no-split (dotted) models at 0.1, 1.3, and 3.7 Myr. The Two-pop-dust-no-split model is the same as the Two-pop-dust model except that we have not changed the fragmentation threshold speed at the ice line. Instead, it is kept constant at 10 m/s.

retention of the dust in protoplanetary disks, which impacts the amount of material available for planetary accretion.

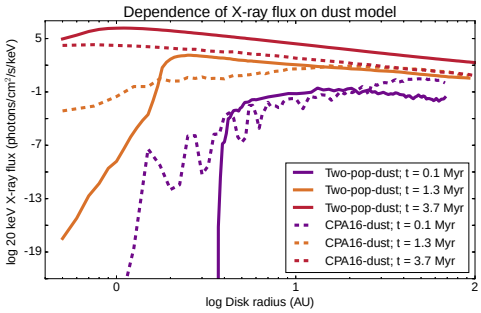

Figure 3.4: Radial distribution of the 20 keV X-ray photons at the midplane of the disk for the two dust models at 0.1, 1.3, and 3.7 Myr. The at earlier times Two-pop-dust model has higher surface density at lower radii and generally truncates the radiation field at larger radii than in the CPA16-dust model. Later on the dust in the Two-pop-dust model has cleared out due to radial drift, which results in a higher flux of X-rays.

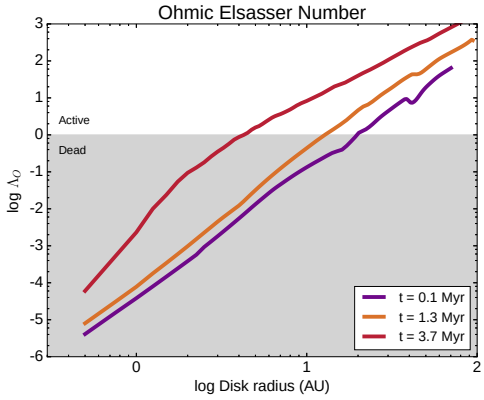

(a) In the CPA16-dust model the disk is well shielded for its entire history. The dead zone begins large and does not shrink far as the disk ages.

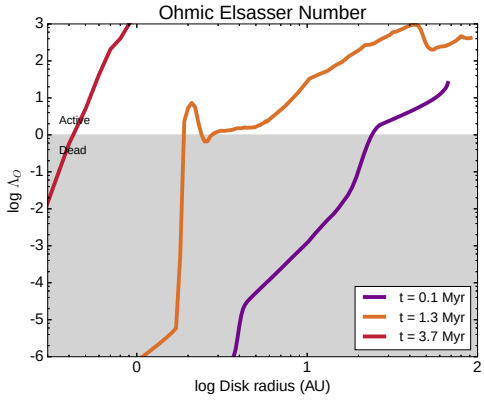

(b) In the Two-pop-dust model the dust is evacuated by radial drift much faster than by viscous stresses. This results in a higher ionization on the midplane and a smaller dead zone at later times.

Figure 3.5: Evolution of the Ohmic Elsasser number for the two dust models. The gray region shows the range of Ohmic Elsasser numbers where we expect the viscosity parameter due to turbulence is lower by two order of magnitudes than in the case of the white region.

3.4.2 Dust Retention

To demonstrate that the ice line is indeed causing a higher retention of the dust, we ran the Two-pop-dust model without changing the threshold speed at the ice line (Two-pop-dust-no-split model).

We show the results of this test in Figures 3.3(a)-3.3(c). In these figures we plot the surface density of dust as a function of radius for the CPA16-dust (dashed), Two-pop-dust (solid), and Two-pop-dust-no-split (dotted) models. We find that the dust dissipates faster in the Two-pop-dust-no-split model than in CPA16-dust. This is due to the radial drift dominating the dust evolution, causing rapid inward migration of the largest dust grains. This impacts the viability of forming planets through core accretion, as the accretion timescale depends on the amount of dust available to accrete. The maximum grain size dictates how efficiently the dust is cleared out because the larger grains are more susceptible to radial drift. This connection implies a link between the treatment of the fragmentation threshold speed and the viability of forming planets through core accretion. If the dust grains are too large and disappear too quickly there will not be enough material to build the solid cores that lead to Jupiter-mass planets.

We do find that the dust in the outer disk is cleared out very rapidly. Decreasing from $\sim 0.001 M_\odot$ at 0.1 Myr down to $\sim 10^{-7} M_\odot$ by 3.7 Myr. Such a reduction is generally inconsistant with observations which show that disks can remain dust-rich for millions of years (Natta et al., 2007; Ricci et al., 2010). Some methods such as gas pressure maxima (ex. Pinilla et al. (2012)) have been suggested as dust traps at large radii. In principle, the sources of these pressure maxima could be similar to the sources of planet traps (eg. dead zone edge, ice lines of volatile species other than H_2O), however their effects are not included in this work.

3.4.3 Midplane X-ray Flux

In Figure 3.4 we show the radiation field along the midplane for the two dust models at 0.1, 1.3, and 3.7 Myr. In the Two-pop-dust model the dust surface density is higher at 0.1 and 1.3 Myr, truncating the radiation field along the midplane at larger radii than in the CPA16-dust model. Early in the disk life the flux of radiation at the midplane of the Two-pop-dust model is more strongly truncated than in the CPA16-dust model. This truncation is due to the dust enhancement that occurs within the ice line and leads to low levels of ionization in that region of the disk. At 1.3 Myr the dust in the Two-pop-dust model is cleared outside the ice line by radial drift. This results in a radiative flux

that is three orders of magnitude higher near the ice line than in the CPA16-dust model. Finally at the latest time, the dust surface density has been cleared out by radial drift and the resulting flux of X-rays is higher everywhere in the disk.

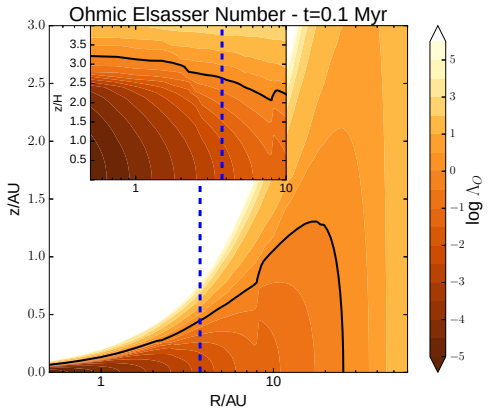

(a) t = 0.1 Myr - CPA16-dust

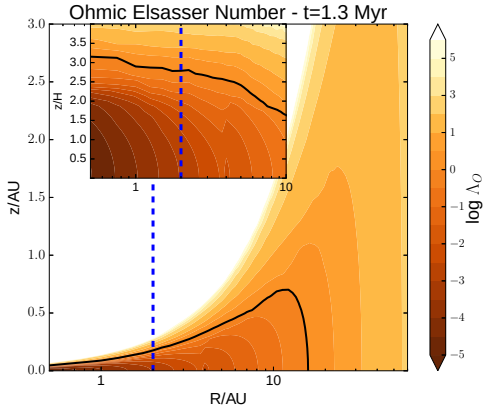

(b) t = 1.3 Myr

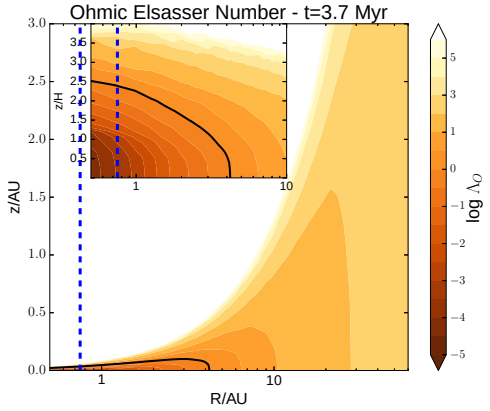

(c) t = 3.7 Myr

Figure 3.6: Radial and height distribution of Ohmic Elsasser number for our CPA16-dust model. The blue dashed line shows the approximate location of the water ice line. The solid black line shows $\Lambda_O = \Lambda_{O,crit} \equiv 1$. The inset scales the height by the gas scale height.

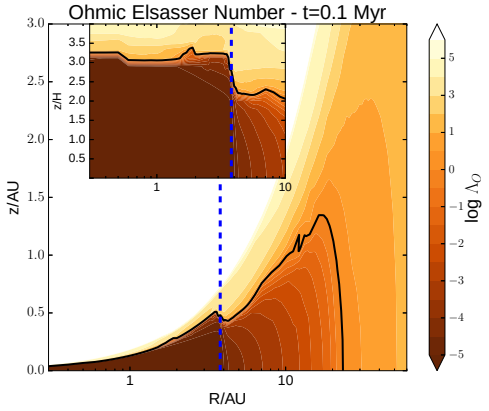

(a) t = 0.1 Myr - Two-pop-dust

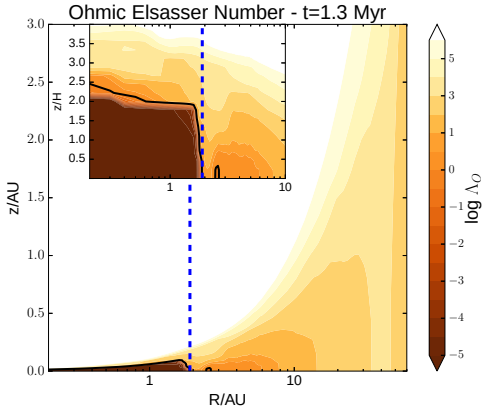

(b) t = 1.3 Myr

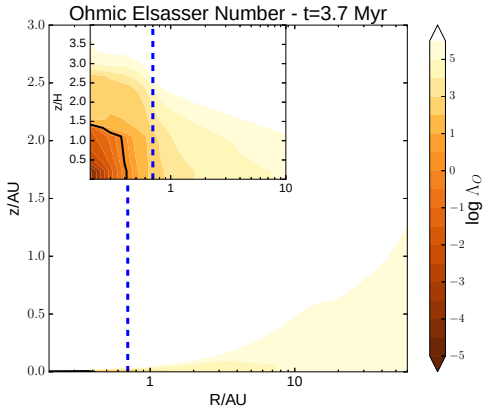

(c) t = 3.7 Myr

Figure 3.7: Same as in Figures 3.6(a)-3.6(c) for our Two-pop-dust model. The location of the ice line is approximately the same, accept within 1 AU because the resolution is higher in this model. The inset scales the height in units of the gas scale height.

3.4.4 Dead Zone Radial Evolution

In Figures 3.5(a) and 3.5(b) we show the evolving radial profile of the Ohmic Elsasser number, computed from the results of our astrochemical code, along the disk midplane for the two dust models. The biggest difference between the two dust models is how quickly the outer edge of the dead zone evolves inward. In the CPA16-dust model the dead zone edge starts at $\sim$ 21 AU and evolves to $\sim$ 4.5 AU by 3.7 Myr. Meanwhile in the Two-pop-dust model the dead zone edge starts at $\sim$ 24 AU and evolves to $\sim$ 0.4 AU by 3.7 Myr. This order of magnitude increase in the rate of inward evolution for the dead zone edge is caused by the more rapid evolution of the dust in the new model. In the CPA16-dust model the dust surface density evolves only through the accretion of material onto the star through viscous stresses. This is generally a slow process, with evolution timescales on the order of a few million years. Conversely, in the Two-pop-dust model the dust evolution is dominated by a much faster radial drift. The dust starts at a higher surface density than in the CPA16-dust model, so the Ohmic Elsasser number (and hence the ionization) does start lower at the smaller radii in the Two-pop-dust model at $t = 0.1$ Myr. The lower ionization is quickly erased as the dust is cleared out through radial drift, and hence near the end of the disk lifetime the height of the dead zone is an order of magnitude lower than in the CPA16-dust model.

Additionally, we find that within the ice line ($R \sim 2$ AU at 1.3 Myr) the ionization significantly drops off. As we have seen, inside the ice line the average grain is smaller than outside the ice line. These smaller grains have more surface area per mass and hence a higher electron capture rate. This directly impacts the ionization because free electrons tend to be much rarer.

3.4.5 2D Structure of the Dead Zone

In Figures 3.6(a)-3.6(c) we show the radial and height dependence of the Ohmic Elsasser number in the CPA16-dust model at three times. The black contour shows edge of the dead zone where $\Lambda_O = 1$ and the blue dotted line shows the location of the water ice line. In the inset, we have focused on the the inner 10 AU of the disk and changed the units of the y-axis into gas scale heights. The purpose of this change in units is to illustrate the effect of dust settling, which is absent in the CPA16-dust model but present in the Two-pop-dust model. In the CPA16-dust model the edge of the dead zone moves to lower radii, while the height of the dead zone is nearly constant at lower radii.

Figures 3.7(a)-3.7(c) are the same as in Figures 3.6(a)-3.6(c) but plot the results for the Two-

pop-dust model. In this case the dead zone not only evolves radially faster than in the CPA16-dust model, but it also tends to shrink towards the midplane faster. From the earlier to later snapshots of the disk the height of the dead zone reduces from 3 scale heights down to 1 scale height within the ice line. This shrinking contrasts the CPA16-dust model where the height of the dead zone does not change significantly. These results are connected to the settling of the largest dust grains which reduces the opacity of the disk higher in its atmosphere. This dependence on the dust settling also means that the ice line impacts the vertical structure of the disk ionization.

At the ice line (denoted by the blue dashed lines in the figures) we find that the height of the dead zone drops by at least a gas scale height when the disk surface density is high (Figure 3.7(a)) and by more when the dust density has dropped (ie. Figure 3.7(b)). At smaller radii than the orbital radius of the ice line the dust is, on average, smaller than the dust at larger radii. These smaller grains are less settled, leaving more dust mass at $z > 1 - 3H$. This results in a more opaque disk at these heights, and lower ionization higher up in the disk.

We emphasize that the black contours outlining the height of the dead zone assumes that the Ohmic resistivity is the only restricting factor to the growth of the MRI modes. This non-ideal effect should dominate the highest densities of the disk and hence will most accurately model the location of the dead zone close to the midplane. In less dense regions of the disk, the MRI is sensitive to other non-ideal MHD effects. These non-ideal effects are ambipolar diffusion, which dominates in the most diffuse parts of the disk, and the Hall effect which should dominate somewhere between the other two (Bai & Stone, 2013). Because of our interest in planet formation, we focus on Ohmic resistivity as we expect the majority of planet formation to occur on along the midplane of the disk. The reader is cautioned that a more realistic dead zone likely extends to a higher disk height than is shown here when ambipolar diffusion and the Hall effect are included.

3.5 Discussion and Conclusions

3.5.1 Implications for Planet Formation

We have demonstrated that the radial evolution of the dead zone is sped up by an order of magnitude when more complicated dust physics is included. The evolution of the dead zone impacts the location of the forming planet that is trapped at its edge. A planet trapped at the dead zone in the Two-pop-dust model will form in regions of the disk that are higher in density than the planet that formed

in the CPA16-dust model. In CPA16-dust model, the dead zone planet failed to form a Jovian mass planet because its accretion rate was too low over the entire 4.1 Myr of evolution. We expect that the planet forming in the dead zone trap in the Two-pop-dust model will achieve a higher mass because it will sample regions of the disk with a higher density of gas and dust, however we leave this calculation to an upcoming paper.

A second effect of the new dead zone evolution is on the saturation of the co-rotation torque, and the trapping power of the heat transition planet trap. This trap is located at the transition point where the primary heating mechanism changes from viscous stresses to direct irradiation (CPA16). This trap starts at 19.5 AU in the fiducial model of CPA16 and remains within the dead zone for the entire lifetime of the disk. Because it is within the dead zone, the planet forming in the heat transition trap saturates after 1.1 Myr and ends up as a Hot Jupiter, very close to its host star.

In Figures 3.8(a) and 3.8(b) we show the radial evolution of the three planet traps from our planet formation model. The location of the heat transition trap is defined by our gas disk model, and is the same in both dust models. The water ice line also shows little difference between the two models, which confirms the validity of using the results of CPA16 to parameterize the location of the ice line for the Two-pop-dust model. The evolution of the dead zone location shows the biggest change, confirming the results of the previous section. Because of the rapidly evolving dust, the dead zone edge shrinks toward the location of the ice line within 1.5 Myr. The rapid decrease at $t \sim 1.5$ Myr is linked to the radial structure of the midplane Ohmic Elsasser number at $r \sim 2$ AU at 1.3 Myr in Figure 4.7(b). This feature is characterized by a peak near the location of the ice line, followed by a valley at larger radii, then a steadily increasing Ohmic Elsasser number with radius. As the disk ages, and the ionization increases, the location of the dead zone trap 'hops' from the outside edge of the valley to its inner edge.

The heat transition trap and dead zone cross very early in the simulation, hence the saturation of the co-rotation torque will not occur at the same time as it did in the results of CPA16. This will keep the planet forming in the heat transition trap farther out in the disk, which slows its growth due to the lower density of material and changes the chemical content of its accreted atmosphere - if it has enough time to accrete an atmosphere.

This known evolution of the dead zone edge location is also important to the evolution of the dust grains because of the dependence of properties like fragmentation and settling on the amount of turbulence in the gas. While not explicitly stated in the methods section, we assumed a constant

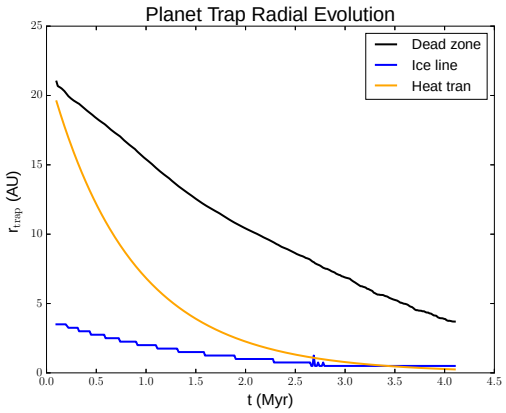

(a) CPA16-dust trap evolution

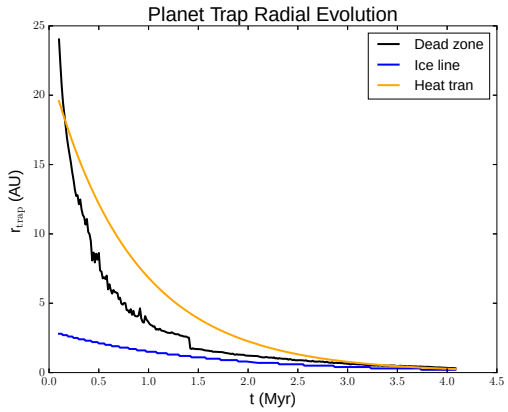

(b) Two-pop-dust trap evolution

Figure 3.8: Temporal evolution of the orbital radius of the three planet trap in our planet formation model. The heat transition trap evolves the same in both models because it is tied to the disk model. The ice line is nearly the same, while the dead zone evolution changes drastically. The step function evolution of the ice line is dependent on the resolution of the chemistry calculation, which is higher in the case of the Two-pop-dust model.

turbulent parameter throughout the disk that modelled a turbulently active fluid ($\alpha = 10^{-3}$). In the Appendix we fit the location of the dead zone as a function of time from Figure 3.8(b) to model the temporal evolution of the radial dependence of the turbulent parameter. We find that the evolving turbulent parameter does not drastically change the resulting location of the dead zone at 0.1 Myr (see Appendix).

3.5.2 Implications for structure seen in ALMA observations of disks

The increase in water vapour and reduction of maximum grain size at radii inside the location of the ice line should have an observable effect on the continuum emission as observed by ALMA (Banzatti et al., 2015). It has been suggested (ie. in Andrews et al. (2016)) that continuum emission gaps in the observations of the protoplanetary disk with ALMA could be explained by the presence of an ice line. In this scenario the increase in water vapour at lower radii than the location of the ice line modifies the opacity which affects the continuum emission.

The effects of the ice line have recently been directly observed with ALMA in the V883 Ori system (Cieza et al., 2016). In that system the protostar is undergoing a burst of accretion which results in an increased stellar intensity, moving the water ice line far out in the disk (~ 42 AU). This discovery is the first of its kind, where the change of the optical depth of the disk has been directly observed. The water ice line is typically at radii less than ~ 5 AU and hence within the resolution limit of our current telescopes. The V883 Ori system is an interesting case study because of its accretion history. As has been discussed, the location and evolution of planet traps (like the ice line) shape the migration and accretion history of protoplanets, as well as impact the radial structure and evolution of the dust. The implications of a stochastic accretion history is beyond the scope of this work.

Andrews et al. (2016) points out that the effect of the water ice line should be universal as we expect that every protoplanetary disk will have an ice line. While this is true, we note that this effect evolves in time, and will look different in systems that have drastically different ages. Conveniently, the two protoplanetary disks that have been observed at the highest resolution: HL Tau (ALMA Partnership et al., 2015) and TW Hya (Andrews et al., 2016) represent systems at either end of the disk evolution. HL Tau is a young (~ 1 Myr) system while TW Hya is an old (~ 10 Myr) one. The closest dark band in HL Tau is at 13.2 AU, while the inner gap in TW Hya is at approximately 1 AU. The location of the dark band in HL Tau has been linked to the water ice line (ie. Zhang et al.

(2015)), while Andrews et al. (2016) notes that their estimated ice line is within the location of the edge of the TW Hya gap. In Figures 3.1(a)-3.1(c) and 3.2(a)-3.2(c) we see that the water ice line in our model evolves from $\sim$ 3.5 AU down to $\sim$ 0.4 AU which is consistent with the estimates of Andrews et al. (2016). At the very late stages of disk evolution ($>$ 4 Myr), the disk is primarily heated through direct irradiation from the host star, which produces a temperature profile that does not evolve in time. Hence the location of the ice line will also cease to evolve.

3.5.3 Conclusions

In this work we have shown that the dust distribution impacts the ionization in the disk. We analyzed the results from two different models of dust evolution: a constant gas-to-dust ratio and well mixed dust model (CPA16-dust) which sets the dust surface density to be proportional to the gas surface density. And a numerical model of dust evolution (Two-pop-dust) where coagulation, fragmentation and radial drift sets the total surface density and size distribution of the dust.

- Radial drift in the Two-pop-dust clears the dust faster than in the CPA16-dust model causing a higher ionization
- In the Two-pop-dust the dead zone edge reduces its physical scale by an order of magnitude when compared to the CPA16-dust model
  - Two-pop-dust: $R_{dz}(t = 0.1 \text{ Myr}) \sim 24$ AU, $R_{dz}(t = 3.7 \text{ Myr}) \sim 0.4$ AU
  - CPA16-dust: $R_{dz}(t = 0.1 \text{ Myr}) \sim 21$ AU, $R_{dz}(t = 3.7 \text{ Myr}) \sim 4.5$ AU

A faster evolving dead zone changes the location of the forming protoplanet that is trapped at its edge

- The relative location of traps with respect to the location of the dead zone impacts whether the planet trap will actually trap a planet.
- In the Two-pop-dust model, while the dead zone begins at a higher radii than the heat transition it rapidly evolves within the location of the heat transition trap
- A planet forming in the heat transition trap will remain trapped over its entire formation in this model

The link between the disk chemical structure and dust physics impacts the retention of the dust

- Within the ice line, dust grains are weaker and the maximum grain size is reduced by two orders of magnitude
- Smaller grains are less susceptible to radial drift and an enhancement of dust forms within the ice line

On top of the rapid radial evolution, the height of the dead zone evolves from $\sim$ 3H down to $\sim$ 1H near the inner edge of the disk over 3.7 Myr of evolution in the Two-pop-model, while it evolves from $\sim$ 3H down to $\sim$ 2.5H at the same radial position over the same time in the CPA16-dust model.

- Dust settling is less efficient within the ice line, hence the dead zone extends higher within the dead zone, by 2 gas scale heights

In a future paper we will connect this model of dust evolution with a full core accretion model of planet formation. This will allow us to directly observe the impact on planet formation caused by this more complicated treatment of dust evolution.

Chapter 4

Composition of Early Planetary Atmospheres II: Coupled Dust and Chemical Evolution in Protoplanetary Disks

What follows has been published in Monthly Notices of the Royal Astronomical Society (MNRAS). See: Cridland, Pudritz, Birnstiel, Cleeves & Bergin 2017. MNRAS

Abstract

We present the next step in a series of papers devoted to connecting the composition of the atmospheres of forming planets with the chemistry of their natal evolving protoplanetary disks. The model presented here computes the coupled chemical and dust evolution of the disk and the formation of three planets per disk model. Our three canonical planet traps produce a Jupiter near 1 AU, a Hot Jupiter and a Super-Earth. We study the dependency of the final orbital radius, mass, and atmospheric chemistry of planets forming in disk models with initial disk masses that vary by 0.02 $M_\odot$ above and below our fiducial model ($M_{disk,0} = 0.1\ M_\odot$). We compute C/O and C/N for

the atmospheres formed in our 3 models and find that $C/O_{planet} \sim C/O_{disk}$, which does not vary strongly between different planets formed in our model. The nitrogen content of atmospheres can vary in planets that grow in different disk models. These differences are related to the formation history of the planet, the time and location that the planet accretes its atmosphere, and are encoded in the bulk abundance of NH_3. These results suggest that future observations of atmospheric NH_3 and an estimation of the planetary C/O and C/N can inform the formation history of particular planetary systems.

4.1 Introduction

What physical processes set the observable chemical abundances in exoplanetary atmospheres? The bulk abundance of the atmosphere will ultimately depend on the chemical structure of the gas that is present in the planet's natal protoplanetary disk (Öberg & Bergin, 2016; Madhusudhan et al., 2014b, 2016a; Mordasini et al., 2016). The disk astrochemistry depends on the physical state of the disk, which includes the temperature, density, and ionization of the gas, and radiative flux of high energy photons (Fogel et al., 2011; Helling et al., 2014). In this and past works (Alessi et al., 2017; Cridland et al., 2016, 2017a) we present a model of an evolving astrochemical disk which when combined with the core accretion model for planetary formation (Ida & Lin, 2004) can predict the bulk chemical abundance of planetary atmospheres.

An 'early' planetary atmosphere is a young ($t_{age} \lesssim 10$ Myr) atmosphere that has not had enough time to physically or chemically evolve to change its observable chemical signature. As such, we do not compute the physical or chemical structure of the atmosphere as it accretes its gas. Instead our work focuses on computing the bulk chemical abundance of the atmosphere that arise from the chemical abundance of the disk's gas that the planet accretes.

The available observational data from secondary eclipse spectroscopy (ie. Line et al. (2014b), Lee et al. (2012), Moses et al. (2013)) and transit spectroscopy (ie. Ranjan et al. (2014), Sing et al. (2015), Wakeford & Sing (2015)) have begun to characterize the chemical composition of exoplanetary atmospheres, detecting species like H_2O, CO_2, CO, CH_4, K, and Na for about a dozen planets. Early connections between theoretical work and observations identified the carbon-to-oxygen elemental ratio (C/O) as an excellent candidate for linking the planet formation process and the resulting atmospheric chemistry (Öberg et al., 2011; Madhusudhan et al., 2014a; Thiabaud et al., 2015). This

ratio varies with disk radius as volatiles are either frozen out or sublimated into the gas phase. Hence C/O of a planet's atmosphere will depend on where that planet accreted its gas, relative to the ice line of volatiles like H_2O, CO_2, and CO (Öberg et al., 2011).

A recent synthetic model that calculated the links between the formation and migration of hot Jupters in evolving disks, to the construction and composition of their atmospheres used simplified models of the composition of planetesimals (Mordasini et al., 2016). The resulting C/O ratios in this analysis were subsolar because of the O rich nature of the accreting solid materials.

In this paper we introduce a new method of computing the coupled chemical and dust evolution of the disk, in order to give a first combined treatment of these two critical aspects of disk evolution and early planetary formation. We use this approach to then address key problems in linking planet formation with the resulting composition of planetary atmospheres. One application of this approach is to demonstrate that the famous C/O and the carbon-to-nitrogen ratio (C/N) may only weakly dependent on the formation history of planets. And that the particular abundance of nitrogen carrying molecules trace details in the planet's formation history like the timing of the planet's gas accretion (Cridland et al., 2016).

Of particular interest to our work is whether the bulk chemical compositions of these 'early' planetary atmospheres can model the bulk compositions that are inferred by emission and transmission spectra of observed planets. In doing so we might learn from where the diversity of atmospheric chemistry is inherited.

The paper is structured as follows: in Section §4.2 we present background information from our previous works, and in Section §4.3 we outline our physical model including our determination of the location of the dead zone. In Section §4.4 we show how the different dust models change the distribution of gas species in the disk, while in §4.5 we report the results of the planet formation in the fiducial model of Cridland et al. (2017a) (CPB17) and compare the results to those of Cridland et al. (2016) (CPA16). In Section §4.5.2 we report the results of the two supplementary disks and compare their resulting planets to the fiducial model. In Section §4.6 we discuss the implications of our results, particularly how a population synthesis model will improve our understanding of variations in atmospheric chemical abundances. We finish with concluding remarks in Section §4.7.

4.2 Background

Our model involves the combination of accretion disk physics, dust physics (coagulation, fragmentation, radial drift and settling), radiative transfer, astrochemsitry (photochemistry, gas phase, and grain surface) and planet formation theory (core accretion and migration). A particularly important aspect of the planet formation model is the use of 'planet traps' to set the location of the protoplanet and limit its rate of migration. Planet traps are inhomogeneities in disk properties where the net torque vanishes, so that migration occurs at the much slower rate of disk evolution. Introduced by Masset et al. (2006) to investigate planetary dynamics at the inner edge of a disk dead zone, planet traps have been generalized and used in population synthesis models to replicate the number of planets observed in different regions of the mass-semi-major axis diagram (for ex. Hasegawa & Pudritz (2011, 2012, 2013)).

A planet trap works because of the relative strength of the Lindblad and co-rotation torques (Masset et al., 2006). The Lindblad torque is caused by the gravitational pull of material that is perturbed from Lindblad resonances near the planet back upon the planet (Ward, 1997). The two nearest resonances are at radial positions with orbital frequencies that are twice the planet's (outer resonance) and half the planet's (inner resonance) orbital frequency. Generally the outer resonance is stronger than the inner resonance and the planet migrates to smaller orbital radii.

The co-rotation torque is caused by gas with orbital frequencies that are close the planet's. The gas enters into horseshoe orbits where they oscillate between orbital radii that are smaller than the planet's to orbital radii that are larger. At the turn of each horseshoe orbit the gas exchanges angular momentum with the planet (Paardekooper et al., 2010). If each turn is symmetrical the co-rotation torque does not exert a net torque on the planet - this is called saturation. With enough turbulence the gas mixes with gas on the opposite side of the horseshoe orbit which causes an asymmetry in the two turns and a net torque which generally causes outward migration (Seager, 2010; Paardekooper et al., 2010). Outside of planet traps, the co-rotation torque is generally weaker than the Lindblad torque.

In our work we are interested in three planet traps: the water 'ice line', the heat transition and the dead zone. The water ice line depends on the chemical state of the gas and is located where the water content of the disk transitions from being primarily in the vapour phase to being in the ice phase. The heat transition traces the location where the disk's heating mechanism transitions from

being primarily due to viscous stresses to direct irradiation from the host star. Finally the dead zone is located at the transition point between a low ionization state where the disk turbulence is weak ('dead'), to a high ionization state where the turbulence is active (Matsumura et al., 2009).

Our fiducial model (CPA16) includes all of the above effects, but assumed a constant dust to gas ratio at all times throughout the disk. In that work we show that the chemical abundance of planetary atmospheres depends on both *where* and *when* the planet accretes its gas. We observe that C/O and C/N ratio encode information regarding the formation history of the planet. Atmosphere C/O ratios that were nearly the same as the disk's initial C/O ratio were found for planets that formed within the water condensation front (ice line) of the disk. We expect that higher C/O ratios (C/O ~ 1, compared to solar: 0.54 and our initial disk: 0.288) will be found in planets that accrete their atmosphere outside the ice line, however this was not demonstrated in that previous paper. The sub-solar C/O of our initial disk was due to our choice of the initial molecular species that are inherited by the disk. Our initial abundances are based on the work of Fogel et al. (2011) and Aikawa & Herbst (1999) and represents the chemical state of a dense molecular cloud.

The C/N ratio is encoded *when* the planet accretes its atmosphere. Atmospheres that were accreted early ($t \lesssim 1$ Myr) have higher C/N ratio by almost a factor of 5 over planets that accrete their atmosphere later ($t > 1$ Myr). The temperature of the disk's gas during accretion is what leads to the large change in C/N between the early and late accretors. Early on, the inner disk ($r \lesssim 5$ AU) is warmer due to viscous heating and the nitrogen content is primarily as NH_3 and HCN which leads to higher C/N than later when the disk is cooler and nitrogen is found primarily as N_2.

We incorporated the effects of dust coagulation, fragmentation, and radial drift to our model in CPB17 and demonstrated that the gas disk became more ionized when compared to the simpler dust model of CPA16 because the radial drift and growth of the grains reduced the disk's opacity to high energy radiation. The ionization structure of the disk is important to our work because it sets the location of one of the planet traps: the dead zone. We assume that the source of turbulence in the disk is driven by the magnetorotational instability (MRI) which is caused by a coupling of the disk's magnetic field to free electrons in the gas (for ex. Balbus & Hawley (1991b)). The growth of turbulence due to the MRI is counteracted by the diffusion of the magnetic field. We assume that the primary source of diffusion on the midplane of the disk is Ohmic resistivity (Bai & Stone, 2013; Gressel et al., 2015). This assumption ignores other non-ideal effects like ambipolar diffusion (Bai & Stone, 2013; Gressel et al., 2015) and the Hall effect (Bai & Stone, 2017). The impact of these

other sources of diffusion are more complicated to estimate and are part of an ongoing discussion regarding the turbulent structure of protoplanetary disks.

In this paper, we compute the formation of the three planets and the chemical structure of their atmospheres in the resulting disk model from CPB17. We will compare the results of our work to the results of CPA16 where we use the same disk parameters, but change the way that the dust physics is handled. Importantly, the more complicated dust physics shows that the disk's dead zone evolved radially much faster than in the disk model with a constant dust to gas ratio without grain coagulation or fragmentation. The faster evolution causes the planet forming in the dead zone trap to have a different formation history, and potentially a different atmospheric composition. In CPA16 the dead zone planet failed to accrete an atmosphere in the 4.1 Myr disk lifetime.

With the need for turbulence to maintain an unsaturated co-rotation torque, the relative location of the dead zone edge and other planet traps dictate whether the planet remains trapped over its formation lifetime. Within the dead zone, we assume that the turbulent α drops by two orders of magnitude when compare to the active region. This reduction leads to a lengthened eddy turnover time, and a saturated corotation torque if the eddy turnover time exceeds the libration time of the horseshoe orbit (see for example CPA16). In CPA16 we found that the planet forming in the heat transition trap saturated 1.1 Myr into formation, causing the planet to quickly migrate and become a Hot Jupiter. In CPB17 we showed that the dead zone was located at smaller radii than the heat transition trap by 1.3 Myr. If the dead zone crosses the heat transition trap's location the co-rotation will remain unsaturated and the planet will remain trapped for its entire formation history. This will produce a different planet than the one reported in CPA16.

Finally it was pointed out in CPA16 that to fully understand the connection between the atmospheric abundance predictions and our model, we would require a statistically significant sampling of possible disk parameters like initial mass and lifetime. In Alessi et al. (2017) it was shown that both of these disk parameters impact the formation history of planets in our formation model. In particular the initial mass of the disk changes the location and evolution of the planet traps, hence the location of the forming planet. Ideally, a full population synthesis model (ie. Ida & Lin (2004); Hasegawa & Pudritz (2013); Alessi & Pudritz (in prep.)), with values drawn from distributions of a few parameters, would be applied in our evolving astrochemical disk. In preparation for a future complete population synthesis study, we report results from two additional disk models where we have varied the initial disk mass by 0.02 $M_\odot$ above and below our fiducial disk of 0.1 $M_\odot$.

4.3 Physical Model

Our evolving astrochemical model as well as our method of identifying the planet trap locations is outlined in detail in Cridland, Pudritz & Alessi (2016). Our dust model is outlined in Cridland, Pudritz, Birnstiel (2017) and was based on the model of Birnstiel et al. (2012). Here we outline the important aspect of each of these models.

Generally we compute the temperature and surface density radial distribution of the gas with an analytic solution of the gas diffusion equation (see Chambers (2009), CPA16). This self-similar model for disk structure and evolution assumes that the heating of the gas is dominated by either viscous evolution or direct irradiation of the host star. Furthermore, as a computation constraint we assume that the disk's opacity and α-parameter (ie. in Shakura & Sunyaev (1973), due to the presence of disk winds and/or turbulence) are constant in space and time, and that the mass accretion rate is constant in space but evolves with time (see Alessi et al. (2017) and CPA16 for details).

This gas model is combined with a model for the evolution of the dust surface density (Birnstiel et al., 2012). The particle size distribution is then reconstructed with the semi analytical treatment of Birnstiel et al. (2015). The dust and gas distributions are computed over many 'snapshots' over a disk lifetime of 4.1 Myr.

In each snapshot we compute the flux of UV and X-ray photons with RADMC3D, a Monte Carlo radiative transfer scheme (Dullemond, 2012). The wavelength dependent disk opacity is computed by the on-the-fly method in RADMC3D and depends on the dust surface density and size distribution using optical constants from Draine (2003). We compute the flux of 4 UV and 3 X-ray test wavelengths, then extrapolate their results for the wavelengths: 930 - 2000 angstroms for UV and 1 - 20 keV for X-ray using sample T Tauri UV (Fogel et al., 2011; Bethell & Bergin, 2011b) and X-ray (Kastner et al., 1999, 2002; Cleeves et al., 2015) spectra as guides.

We note that relying solely on dust as our source of disk opacity does ignore the X-ray cross section of the gas. Over our range of wavelengths dust does dominate the X-ray cross section (Bethell & Bergin, 2011b), however we will likely underestimate the disk's opacity late in it's evolution as the dust surface density drops. At these late times, the gas will begin to dominate the cross section and set a floor to the disk's opacity.

Next we compute the astrochemistry using a chemical kinetic code (ie. Fogel et al. (2011); Cleeves et al. (2014), CPA16) in each snapshot using the gas, dust, and radiation as inputs. This process

produces an evolving astrochemical disk in which we computed the formation of a planet using the core accretion model and the migration of the forming planet with a planet trap model. Some specific features of this theoretical framework are discussed below.

4.3.1 Evolving Astrochemical Model

An important feature in our astrochemical model is the fact that the temperature and density profiles evolve with time as the disk ages. The chemistry is handled with a non-equilibrium code from Fogel et al. (2011) and Cleeves et al. (2014). This astrochemical code includes, among others, ion-driven gas phase reactions, the freeze out of volatiles, photo-desorption, and the production of water through grain surface reactions. In the chemical model we compute an average grain size based on the results of our dust model (see below), and allow the average grain size to vary at different disk radii and evolve in time.

We combined this chemical model with an analytic disk model from Chambers (2009) which models a disk that evolves due to mass accretion caused by viscous stresses. This analytic model produces temperature and surface density profiles that scale as:

$$T \propto R^{\beta}; \quad \Sigma \propto R^{s}, \tag{4.1}$$

where the exponents β and s are determined by the source of heating. Viscous heating and direct irradiation are the primary heating sources. Viscous heating is caused by gravitational energy being released as material accretes through the disk. This heating scales with the mass accretion rate $\dot{M}$ which is reduced as time passes. Because of this dependence, the region of the disk that is viscously heated will cool as the disk ages. At larger radii the densities are lower and the heating is dominated by the direct irradiation of the disk from the host star. We assume that the stellar properties of the host star do not change, so the temperature profile of the disk is also static. This assumption ignores the effect of excess high energy photons due to the accretion shock on the heating of the disk. In doing so we have likely underestimated the temperature of the disk in the irradiated region at the earliest times. However, as the disk ages and the accretion rate drops the heating from the accretion shock is drastically reduced. In a future work we will explore the impact of both the temperature structure and chemistry of an evolving stellar emission spectrum.

Viscous heating dominates at smaller radii where the densities are the highest, but as the disk

accretes its density and mass accretion rate both drop. As the mass accretion rate drops, the region of the disk where viscous heating dominates shrinks and the point where the temperature from viscous heating is the same as the temperature from irradiation (the heat transition trap) moves to smaller radii.

The evolving viscously heated region of the disk also has important implications to the chemistry in the disk. Features like the water ice line, which closely depends on the temperature of the gas, will evolve to lower radii as the disk cools. Additionally the main molecular carrier of some elements, like nitrogen, can change depending on the temperature of the gas. In hotter disks the nitrogen will generally be found in NH_3 and HCN, while in cooler disks it is mostly found in N_2 (CPA16). This change in elemental carrier will be imprinted in the bulk chemical abundance of the planetary atmosphere based on *where* and *when* the planet accretes its gas.

Just as the temperature profile evolves, the surface density profile of both the gas and dust also changes with time. The gas density drops as mass is accreted onto the host star due to turbulent viscous stresses and magnetocentrifugal winds. Likewise the dust also accretes onto the host star through viscous stresses, however the it is also susceptible to a faster source of evolution: radial drift. Radial drift involves the sub-Keplarian orbit of dust grains caused by a gas drag which scales with the surface area of the grain. As a result the largest grains are most affected by radial drift, which when combined with coagulation causes a faster reduction in surface density than viscous evolution alone. The dependency of the radial drift rate with grain surface area extends up to a point where the grain's inertia becomes too great for gas drag to have a large impact on the grain's orbit. Our size distribution extends up to a few tens of cm, and so we do not simulate the dust evolution up to this cut off. The growth and drift of dust grains lead to an overall reduction in the disk's opacity to high energy photons, and an increase in the ionization of the gas (CPB17). While we do evolve the radial drift of dust grains (see below), we ignore the transport of frozen volatiles on the grains as they migrate inwards. In principle, grains will bring volatiles from the outer disk to smaller radii as they drift which could enhance the abundance of volatiles in the planet-forming regions of the disk ($r \lesssim 10$ AU). We leave an investigation into this effect to future work.

Ions drive chemical reactions because of their lower activation barrier when compared to neutral-neutral gas reactions. As mentioned above they also cause turbulence through the MRI when coupled to the disk's magnetic field. Because the chemical and physical state of the gas is sensitive to the flux of ionizing photons, an accurate description of disk opacity and evolution of the dust is an important

Table 4.1: Initial abundances relative to the number of H atoms. Included is the initial ratio of carbon atoms to oxygen atoms (C/O) and the initial ratio of carbon atmos to nitrogen (C/N).

Species	Abundance	Species	Abundance
H_2	0.5	H_2O	2.5×10^{-4}
He	0.14	N	2.25×10^{-5}
CN	6.0×10^{-8}	H_3^+	1.0×10^{-8}
CS	4.0×10^{-9}	SO	5.0×10^{-9}
Si^+	1.0×10^{-11}	S^+	1.0×10^{-11}
Mg^+	1.0×10^{-11}	Fe^+	1.0×10^{-11}
C^+	1.0×10^{-9}	GRAIN	6.0×10^{-12}
CO	1.0×10^{-4}	N_2	1.0×10^{-6}
C	7.0×10^{-7}	NH_3	8.0×10^{-8}
HCN	2.0×10^{-8}	HCO^+	9.0×10^{-9}
C_2H	8.0×10^{-9}	C/O	0.288
		C/N	4.09

feature of our model.

We use the same initial chemical abundances as in CPA16, derived from Fogel et al. (2011) and (Aikawa & Herbst, 1999), see Table 4.1.

4.3.2 Dust Model

Our evolving dust model was presented in CPB17 and is based on the Two-population model presented in Birnstiel et al. (2012). This model involves estimating the size and density distribution of the dust grains by computing the evolution of two sample dust populations, one representing the smallest grains (monomers) and one representing the large population. The size distribution is assumed to be a power law with a monomer size of 0.1 microns and a maximum size set by either fragmentation or radial drift depending on which physical process has the lower timescale.

This simplified dust model has been tested against full coagulation simulations, reproducing the general trends from those more complicated models (Birnstiel et al., 2012). A benefit of the Two-population model is how quickly the evolution can be computed. Depending on the treatment of the fragmentation, standard dust evolution codes scale $O(N^2)$ where N is the number of grain sizes used in the simulation. So the Two-population model, which computes the coagulation, fragmentation and radial drift of only two populations can be run much faster than a standard coagulation simulations that is resolved with at least 100 different sizes.

Our dust model includes the effect of a changing fragmentation threshold speed across the water ice line, as first discussed in Birnstiel et al. (2010). The fragmentation threshold speed is the minimum

relative collision speed that results in the fragmentation of the grains. This threshold speed depends on the chemical nature of the dust grain, its porosity, and the amount of ice coverage. For simplicity we assume a threshold speed of 10 m/s outside the water ice line because the grain is fully covered, and hence strengthened by a layer of ice (Wada et al., 2009; Gundlach & Blum, 2015). Within the ice line the layer of ice is gone and the threshold speed is reduced to 1 m/s. We used the chemical results of our fiducial model (CPA16) to fit the location and evolution of the water ice line as a function of time. Using this fit we allowed the location of the water ice line to evolve throughout the evolution of the dust.

The impact of this changing fragmentation threshold speed leads to a reduction in the size of the largest grain by about two orders of magnitude within the water ice line (CPB17, or see Figure 4.7 below). These smaller grains radially drift slower than larger ones, with a drift time scale of the form (Birnstiel et al., 2010):

$$\tau_{drift} = \frac{rV_k}{Stc_s^2}\gamma^{-1} \tag{4.2}$$

at the radial position r. The Kepler speed (V_k) and gas sound speed (c_s) are evaluated at the position r. The Stokes number scales linearly with the size of the grain and encodes the coupling between the grain and the gas. Longer drift time scales within the ice line lead to an enhancement of the dust surface density of an order of magnitude within the water ice line. This enhancement has two important affects on planet formation: first it shields the inner disk from high energy photons, reducing the level of ionization early on in the disk lifetime. Secondly, the enhancement will increase the growth rate of the forming planet because there is more material available during oligarchic growth.

4.3.3 Planet Formation Model

Our planet formation model relies on the Core Accretion model as seen in Ida & Lin (2004) to compute the rate of mass accretion onto the planet. This core accretion model is used in conjunction with the planet trap model that was outlined above. The combination of these two models has been used in population synthesis models to reproduce the population statistics that have been observed in the exoplanetary data (Hasegawa & Pudritz (2013); Alessi & Pudritz (in prep.)).

Core Accretion Model

The Core Accretion model contains three important phases of accretion. The first is known as oligarchic growth, where a single core accretes solid material from a sea of 10-100 km sized planetesimals. We do not model the growth of these planetesimals from micron sized dust grains up to their assumed sizes, instead we assume that all of the available solid material is in planetesimals. In doing this, we neglect the reduction in the disk's opacity caused by the rapid agglomeration of dust particles caused by the streaming instability (see for ex. Schäfer et al. (2017)). The growing planet will impact the surface density of the surrounding gas and dust, and as a result will locally change the temperature and ionization of the gas. These effects are beyond the scope of this work.

The rate of accretion is fast, with timescales $O(10^5)$ yr. The solid accretion rate has the form (Ida & Lin (2004), their equations 5 and 6):

$$\begin{aligned}\frac{dM_c}{dt} =& \frac{M_c}{\tau_{c,acc}} \\ \simeq& \frac{M_c}{1.2\times10^5}\left(\frac{\Sigma_d}{10\mathrm{gcm}^{-2}}\right)\left(\frac{a}{1\mathrm{AU}}\right)^{-1/2} \\ &\times\left(\frac{M_c}{M_\oplus}\right)^{-1/3}\left(\frac{M_s}{M_\oplus}\right)^{1/6} \\ &\times\left[\left(\frac{\Sigma_g}{2.4\times10^3\mathrm{gcm}^{-2}}\right)^{-1/5}\left(\frac{a}{1\mathrm{AU}}\right)^{1/20}\left(\frac{m}{10^{18}\mathrm{g}}\right)^{1/15}\right]^{-2} \\ &\mathrm{g\ yr}^{-1}. \end{aligned} \tag{4.3}$$

The growing core quickly accretes all of the solid material in its immediate vicinity. At this point it has reached its 'isolation mass' (Ida & Lin, 2004), which represents the maximum available material to the planet if the planet does not migrate. Once it has reached its isolation mass the rate of planetesimal accretion drops, allowing for gas accretion to take place.

We assume that the gas accretion rate is limited only by the Kelvin-Helmholtz timescale which we model with

$$\tau_{KH} \simeq 10^c\left(\frac{M_{plnt}}{M_\oplus}\right)^{-d}\ \mathrm{yr}, \tag{4.4}$$

so that the mass of the planet grows as

$$\frac{dM_{plnt}}{dt} = \frac{M_{plnt}}{\tau_{KH}}, \tag{4.5}$$

for further details see Alessi et al. (2017). The form of equation 4.4 has been demonstrated by numerical simulations, and the constants c and d have been shown to have values between 8-10 and 2-4 respectively (Ida & Lin, 2004). We follow Ida & Lin (2004) in choosing $c = 9$ and $d = 3$. This choice was also used in Hasegawa & Pudritz (2013) to recreate the distribution of planets on the mass semi-major axis diagram derived from observations.

While in practice the gas surface density is locally reduced by the accreting planet (see for example Ormel et al. (2015)), we do not update the disk gas density and temperature while the planet draws down its atmosphere.

Planetary Migration

As it forms, the protoplanet and its natal accretion disk exchange angular momentum through the Lindblad and co-rotation torques (Paardekooper, 2014) which generally results in a loss of angular momentum for the protoplanet. This loss causes the planet to 'migrate' to smaller orbital radii in a process called Type-I migration.

As was previously stated, Type-I migration is limited by discontinuities in disk properties known as 'planet traps' (Masset et al., 2006). Here we assume that a trapped planet will exactly follow the radial location of the its planet trap. If the Ice line and Heat transition traps are found within the Dead zone, we check at every timestep whether the co-rotation torque saturates by comparing the eddy turnover time of the gas to the gas libration time. If the libration time is shorter than the eddy turnover time then the co-rotation torque saturates.

When the co-rotation torque saturates, the planet breaks free of the trap, and we compute its radial evolution due to the Lindblad torques along (Seager, 2010),

$$\Gamma = C_\Gamma \Sigma_p \Omega_p^2 a^4 \left(\frac{M_p}{M_s}\right)^2 \left(\frac{a}{|\Delta r|}\right)^2, \tag{4.6}$$

where Ω_p, a, and M_p are the optical frequency, radius, and mass of the planet, M_s is the mass of the host star, and Σ_p is the gas surface density at the planet's location. The constant $C_\Gamma =$

$-(2.34-0.10s)$ (Paardekooper et al., 2010) has been determined through numerical simulations. The minimum length scale $|\Delta r|$ below which the gas does not contribute to Lindblad torques depends on the relative impact of the planet's gravity to the gas pressure on the dynamics of the gas. Below the Hill radius (R_H) gas particles become bound to the planet, while below the gas scale height (H_p) the gravitational effects of the gas are smoothed out. Therefore we set $|\Delta r| = max(H_p, R_H)$.

We evolve the orbital radius of the planet through $\dot{a}/a = \Gamma/J_p$ where $J_p = M_p a^2 \Omega_p$ is the orbital angular momentum of the planet. As such the planet's orbital radius evolves as,

$$\frac{1}{a}\frac{da}{dt} = \frac{C_T \Sigma \Omega_p a^2}{M_p} \left(\frac{M_p}{M_s}\right)^2 \left(\frac{a}{max(H_p, R_H)}\right)^2 \tag{4.7}$$

when the co-rotation torque saturates.

In what follows, when discussing the properties of our forming planets we will refer to the planet by the trap where it originated.

4.3.4 Importance of Opacity for Gas Accretion

The ability of a planet to accrete its atmosphere is limited by the cooling rate of the gas as it shreds its gravitational energy. This cooling rate depends on the gas opacity which measures the cross section of photon absorption or scatter per unit mass of gas.

As the planet accretes gas it forms an envelope around the planet core that then slowly contracts onto the planet. This process is modeled by two physical properties: the gas accretion rate which depends on the planet mass and Kelvin-Helmholtz timescale, and the critical planet mass above which the gas envelope can contract onto the core.

In previous population synthesis models (ie. Hasegawa & Pudritz (2013)) and in our previous work (CPA16) the Kelvin-Helmholtz timescale and critical mass are individually parameterized so that they have the form of Equation 4.4 and

$$M_{crit} = 10 \cdot f_{crit} \left(\frac{\dot{M}_{core}}{10^{-6} M_\oplus \mathrm{yr}^{-1}}\right)^q M_\oplus, \tag{4.8}$$

respectively. Ikoma et al. (2000) showed that the parameters c and f_{crit} depend on the opacity, while the parameters d and q depend on the choice of opacity table (Ida & Lin, 2004).

The equivalent form of Equations 4.4 and 4.8 from Ikoma et al. (2000) have the form:

$$\tau_{env} = 3 \times 10^8 \left(\frac{M_{core}}{M_\oplus} \right)^{1-1/q} \left(\frac{\kappa}{\mathrm{cm^2 g^{-1}}} \right)^{s/q} \mathrm{yr}, \tag{4.9}$$

where $s/q \simeq 1$, κ is the dust opacity, and

$$M_{crit} = 7 \left(\frac{\dot{M}_{core}}{10^{-7} M_\oplus \mathrm{yr}^{-1}} \right)^q \left(\frac{\kappa}{\mathrm{cm^2 g^{-1}}} \right)^s M_\oplus. \tag{4.10}$$

The parameters s and q are within the range of 0.2-0.3 (Ikoma et al., 2000), and based on our choice of parameters for Equation 4.4 imply that $s = q = 0.25$. In our normalization of Equation 4.4 we assume that $\kappa \sim 3.33$ cm^{2}g^{-1} which is consistent with the Rosseland mean opacity for a sub-mm grain computed by our opacity table.

With our assumed opacity we find that $f_{crit} \simeq 1.6$ while in CPA16 we assumed $f_{crit} = 0.2$ based on results from population synthesis models (Hasegawa & Pudritz, 2012). When f_{crit} is higher, gas accretion begins later in the planet's formation history which changes the radial location and timing of the atmosphere formation.

A smaller f_{crit} assumes that the envelope opacity is lower, which would imply some grain growth within the envelope. Because the dust physics is not well constrained in the envelope of accreting planets we will show the results for $f_{crit} = 0.2$, which matches the parameters used in CPA16. In the Appendix we include the results for $f_{crit} = 1.6$ for the fiducial disk mass, connecting Equations 4.9 and 4.10 with an assumed constant envelope opacity of 3.33 cm^{2}g^{-1}.

4.4 Results: Disk Astrochemistry

The main purpose of this work is to assess the effect of different dust models on disk astrochemistry and the resulting atmospheric abundances. To that end we first compare the chemical results of the CPA16 disk model to the disk chemistry that is computed here, and based on the dust model presented in CPB17.

4.4.1 Comparison of the Distribution of Gas Species

In Figures 4.1 and 4.2 we present the radial distribution of the midplane chemical abundances for a few chemical species in the CPA16 chemical model (solid line) and the chemical results from the

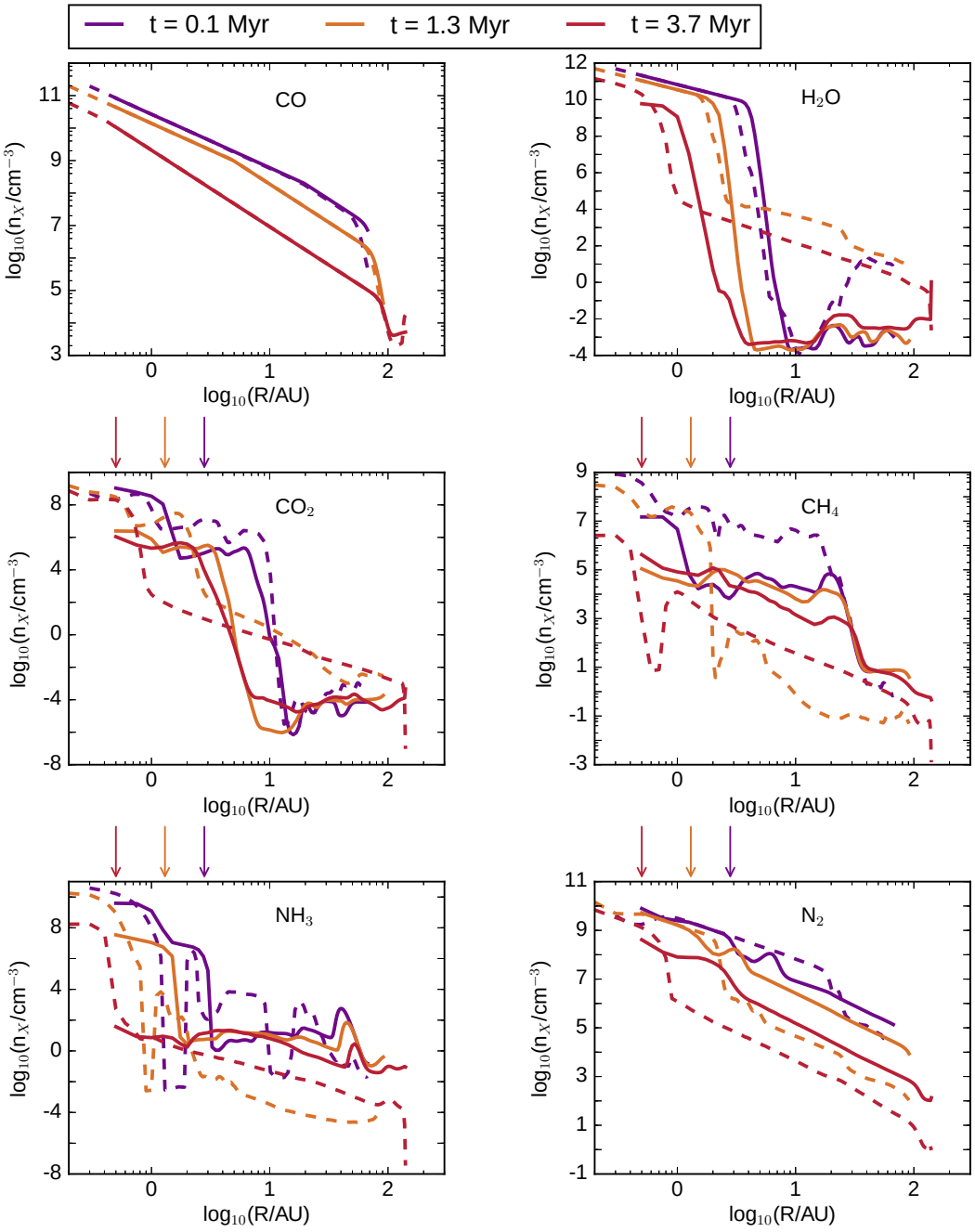

Figure 4.1: Radial distribution of the chemical species that are important to the observations of exoplanetary atmospheres for the CPA16 disk model (solid lines) and for the results of the CPB17 dust model presented in this work (dashed lines). The coloured arrows denote the approximate location of the water ice line in the CPB17 model, defined as the point where the water vapour abundance has dropped by half.

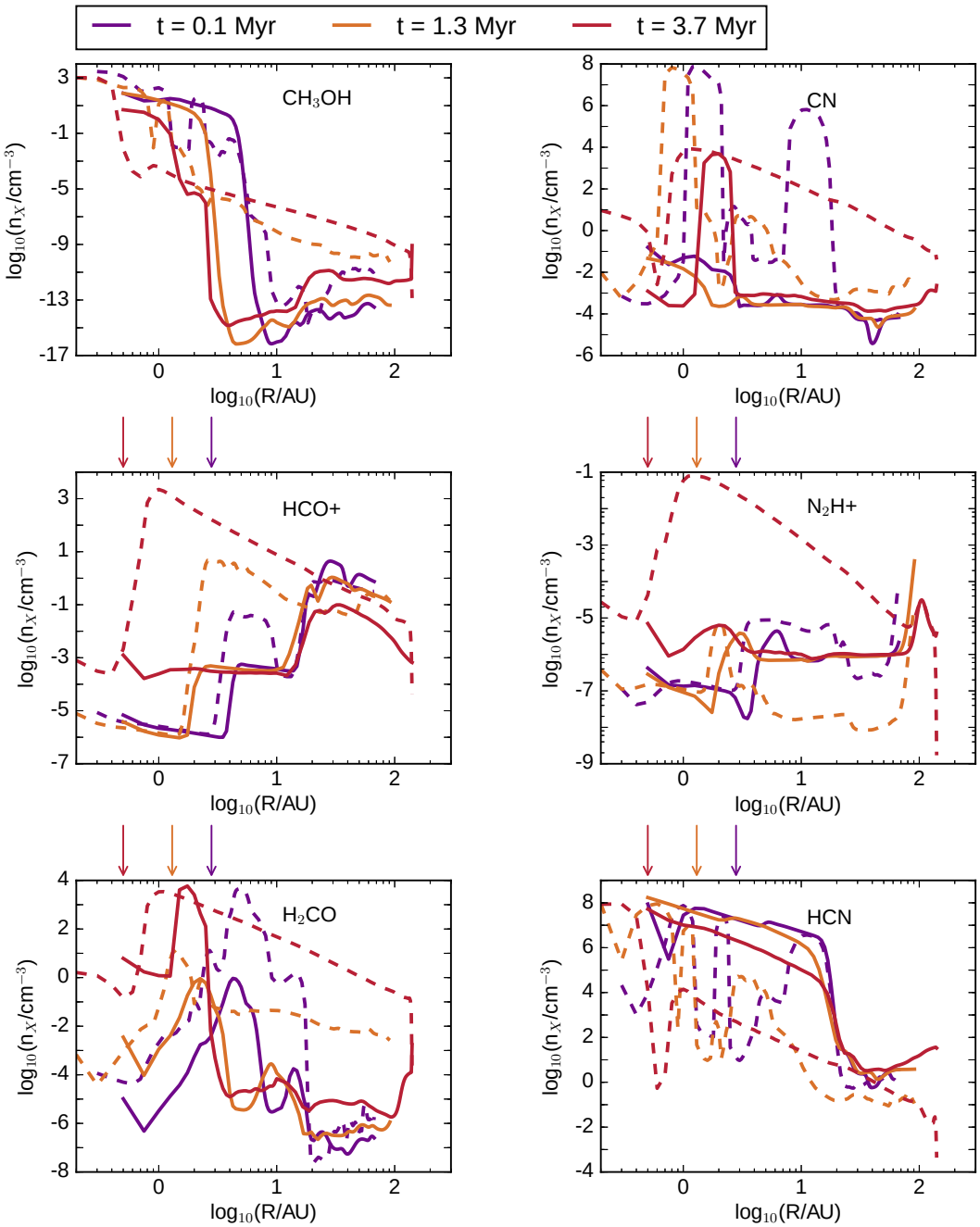

Figure 4.2: Same as in Figure 4.1 but for other chemical species that have been observed in protoplanetary disks, and are used as tracers of photochemical processes.

disk model presented in CPB17 (dashed line). In Figure 4.1 we show the important chemical species to the observations of exoplanetary atmospheres, while in Figure 4.2 we show other molecules that have been observed or used as tracers in protoplanetary disks.

Primary Carbon and Oxygen Carriers

In the top 4 panels of Figure 4.1 we compare the primary carbon and oxygen carriers in this disk midplane. An important difference between the chemical distributions that resulted from the CPA16 (solid line) and CPB17 (dashed line) dust models is the abundance of volatiles like H_2O and CO_2 at larger radii. For the results of this work, based on the dust model in CPB17, there is a higher abundance of volatiles farther out in the disk, where one would expect the ice component of the above species would dominate. The retention in the CPB17 dust model is connected to the fact that the largest dust grains are more rapidly depleted than in the CPA16 dust model. As a result the amount of dust available for volatile freeze out is reduced in the CPB17 dust model. In addition to the reduction of available surface onto which volatiles can freeze, a reduction of the disk opacity to UV photons can also lead to an enhancement of gas abundance through the photodesorption of frozen species.

At smaller radii than the water ice line there is an enhancement of dust surface density fueled by the inward radial drift of dust grains. This enhancement shifts the location of the water ice line inward by ~ 0.5 AU in the new dust model. We additionally find that the ice lines of CO and CO_2 are also shifted from their position in the CPA16 model. These changes are linked to the increase of photodesorption at larger radii than the water ice line that results from the reduced dust opacity in the outer disk, and higher radiative flux along the midplane.

Primary Nitrogen Carriers

In the bottom 2 panels of Figure 4.1 we compare the abundances of N_2 and NH_3. As mentioned before (or see Figure 4.7 below), there is a higher dust surface density within the water ice line of the CPB17 model when compared to the CPA16 model. This enhancement leads to higher abundance of nitrogen carriers within the water ice line because of the electron capture and subsequent dissociation of ions like N_2H^+ and NH_4^+ (Herbst & Klemperer, 1973) are catalyzed by the presence of dust. Similarly with a higher dust surface density at smaller radii, the gas is shielded from destructive high energy radiation. This dust enhancement is not seen in the CPA16 dust model because of the simpler

treatment of dust physics and as a result we find that NH_3 is destroyed as the disk ages.

An important caveat to our derived NH_3 abundances is that we currently ignore the formation of NH_3 ice through successive capture of atomic hydrogen by atomic nitrogen on the surface of grains (see for ex. Watson & Salpeter (1972)). This process is analogous to the formation of water ice on dust grains, which is included in our chemical model. The extra NH_3 ice could then contribute to its gas abundance through photodesorption and thermal desorption. This possible extra source of NH_3 formation implies that our presented abundances here may represent a lower bound of possible observed abundances.

Photochemical Tracers

In the middle panels of Figure 4.2 we show the enhancement of chemical tracers of disk ionization (HCO^+ and N_2H^+) relative to the chemical model presented in CPA16. This enhancement confirms the high ionization rate that is present in the CPB17 disk model. In the bottom right panel of Figure 4.2 we show the abundance of HCN while in top right panel of Figure 4.2 we show the abundance of CN. Observationally, the relative abundance of these species has often been used as a proxy for UV flux. In this work we see a reduction in the abundance of HCN relative to the results of CPA16, and the corresponding enhancement of CN which suggests that UV photolysis is more prevalent in the CPB17 disk model than in our previous model. This prevalence is simply due to the reduced disk opacity and increased UV flux along the midplane. We will elaborate on the link between the flux of high energy and the abundances of HCN and CN in more detail in the following subsection.

At late times in the CPB17 disk model (red dotted line) tracers that are formed from photochemical processes (CN, HCO^+, N_2H^+, and H_2CO) follow similar radial distributions: low abundances within the water ice line and high abundance outside. At late times photochemistry dominates the productions of these chemical species, and hence their abundance is directly linked to the flux of high energy photons on the midplane. This fact can most easily be seen in HCO^+ which shows a dramatic increase in its abundance outside the water ice line, where high energy photons can first penetrate down to the midplane. N_2H^+ is largely kept under-abundant by destructive reactions with gaseous CO (Qi et al., 2013, 2015). At the largest radii, outside of the CO ice line, N_2H^+ is recovered in all models when the CO gas freezes out.

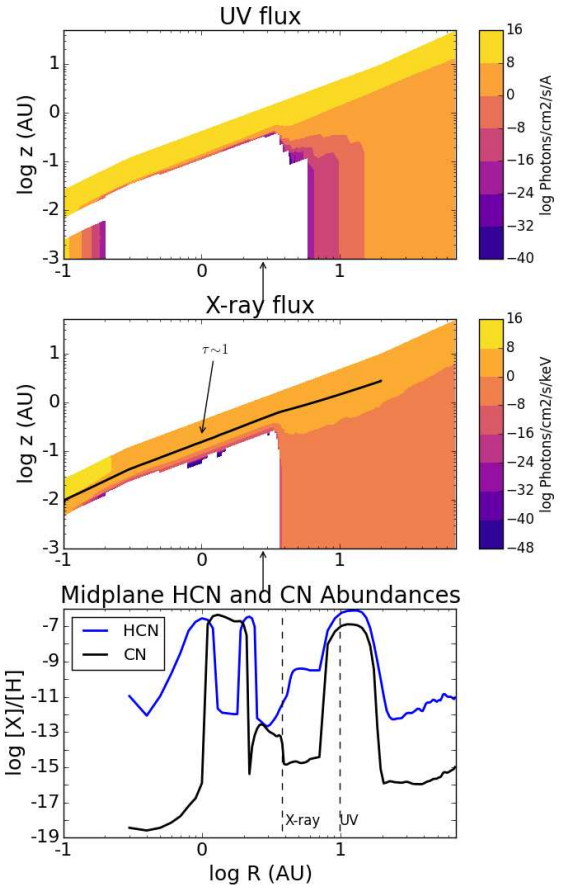

Figure 4.3: The radiative flux of the highest energy bands of UV (top panel) and X-ray (middle panel) along with the midplane abundances of HCN and CN at $\log_{10} t/yr = 5.0$. On the middle panel, we plot an estimate of the height where an incoming X-ray photon reaches an optical depth of one. On the bottom panel, the dotted lines show the midplane location of the 10^{-8} contours of the UV and X-ray flux. The location of the water ice line is denoted with the black arrow on the top and middle panels. On the contour plots, regions of white space denote zero flux.

4.4.2 HCN/CN as a Tracer of Dust Physics and Radiative Flux

As an example of the subtle link between dust physics, radiative transfer, and chemistry we discuss the changes in the abundance of HCN and CN at different disk radii. The relative abundance of HCN and CN is often used as an observational tracer of UV flux in protoplanetary disks (for ex. Kastner et al. (1997)) because of the chemical pathway that produces CN through the photodissocation of HCN (Willacy & Langer, 2000).

In Figure 4.3 we relate the midplane abundance of HCN and CN to the flux of high energy photons through the disk. Within the water ice line (denoted by the black arrows) the large abundance of dust grains shields the gas from high energy photons allowing ion chemistry, catalyzed by the presence of dust, to dominate the production and destruction of HCN and CN. The ions responsible for these reactions are the residual ions from our initial chemical state (Table 4.1). Crossing the water ice line results in a strong reduction of dust surface density, and a subsequent reduction in the abundances of both HCN and CN.

The radiative flux of both UV and X-ray photons show similar features in our disk models. There is a layer of highly ionized (electron fraction $\sim 10^{-2}$) gas far above the midplane of the disk. This layer is denoted by the brightest contours in Figure 4.3. In the middle panel of Figure 4.3 we plot an estimate of the height where photons reach an optical depth of one. Lower than this height the flux of photons coming directly from the source (ie. ignoring scattering) is attenuated, reaching zero in the white regions of the figure. The high optical depth of the disk's dust within the water ice line creates a shadowing outside the ice line which is eventually filled in through scattering. As the disk ages and the dust surface density is reduced, the shadowing shrinks and its edge moves to lower radii. X-ray photons scatter most efficiently, so their flux recovers very quickly just outside the location of the water ice line. By contrast, the lower energy UV photons take longer to recover along the midplane. We note the difference in the radial location of the 10^{-8} contour as dotted lines on the bottom panel of Figure 4.3.

Moving outward from the water ice line, the abundance of HCN and CN initially drops because of the reduced surface density of dust, but HCN begins to recover when the flux of X-rays along the midplane suddenly increases. The abundance of CN remains low until the flux of UV photons begins to rise, at which point it is produced by the photodissociation of HCN. While HCN is destroyed by photodissociation, it is efficiently produced through ion chemistry, maintaining its abundance until

the gas is sufficiently cold to allow HCN to freeze out. Finally at the largest radii we reach the HCN ice line, where it begins to freeze out onto dust grains. This freeze out also strongly reduces the abundance of CN since there is less HCN in the gas phase to photodissociate.

4.4.3 Summary of Key Chemical Results

- We find minimal changes to the location of the water and CO ice line between the two disk models from CPA16 and CPB17
- The CO_2 ice line shows larger variation between disk models, caused by the increased flux of UV at the midplane
- Volatiles are more abundant in the outer disk of the CPB17 disk model, caused by a radial drift induced reduction of dust surface density in the outer disk and less efficient freeze out
- An enhancement of NH_3 and N_2 is found within the water ice line of the CPB17 disk model because of the higher dust surface density within the water ice line
- The abundance of photochemical tracers (HCO^+, HCN, and CN) are indicative of higher UV and X-ray flux on the midplane of the CPB17 disk model, outside of the water ice line
- Strong variation in chemical abundances can be linked to gradients in dust surface density, and radiative flux of high energy photons

Table 4.2: Final planetary properties at $t = t_{life}$ from the CPA16 and CPB17 dust models

CPA16	M_{plnt} ($M_\oplus$)	a_{final} (AU)
Dead zone	0.95	3.7
Ice line	753.2	0.11
Heat transition	454.5	0.15
CPB17	M_{plnt} ($M_\oplus$)	a_{final} (AU)
Dead zone	197.2	0.12
Ice line	1090.2	0.25
Heat transition	4.24	0.27

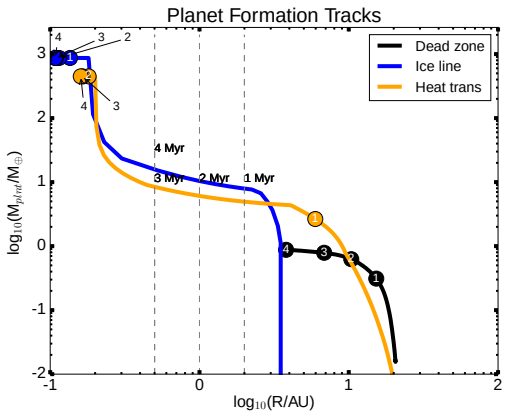

(a) Planetary formation tracks from CPA16.

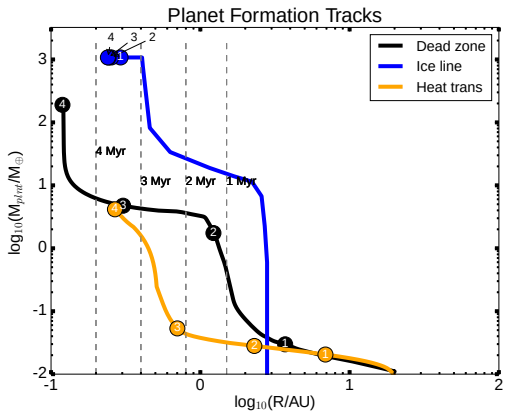

(b) Planetary formation tracks for this work based on the CPB17 dust model.

Figure 4.4: Planet formation tracks for the two different disk models presented in CPA16 and CPB17. Each model had the same disk mass, size, gas evolution and planet formation model. The only difference is in the choice of dust model. The grey dashed lines shows the location of the water ice line for the two disk models at 1,2,3 and 4 Myr. The annotated numbers shows where on the mass and semi-major axis diagram the planet is at 1,2,3 and 4 Myr. In the CPB17 dust model, the chemical abundance of the disk was computed at a higher resolution than in CPA16. Hence why the water ice line appears to evolve to smaller radii in the right panel.

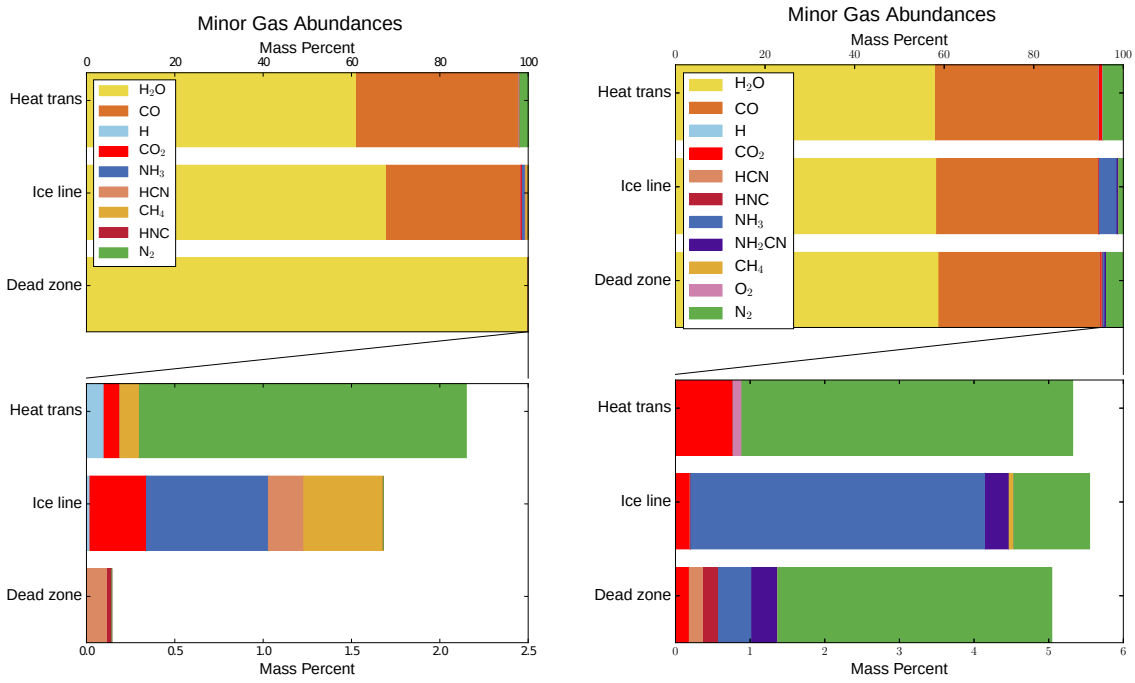

(a) Atmospheric results presented in CPA16.

(b) Atmospheric results of this work, based on the dust model presented in CPB17.

Figure 4.5: Atmospheric abundances for most abundant gases other than hydrogen and helium. The bottom panels of both plots are the most abundant gases after water and CO are also removed. Note that in the bottom panel of Figure 4.5(b) the scale is a factor of 5 larger than in the bottom panel of Figure 4.5(a).

4.5 Results: Planetary Atmospheres

In the CPB17 disk model, the evolution of the chemical state of the disk changes the formation history of dynamically trapped planets. Here we compare the planetary atmosphere results from CPA16 model and the chemical model presented in this work.

4.5.1 Comparing Planetary Formation and Atmospheric Composition for Different Dust Models

In Figures 4.4(a) and 4.4(b) we show the evolution of the forming planets through the mass and semi-major axis diagram for the model presented in CPA16 (4.4(a)) and the model presented in CPB17 (4.4(b)). We find a significant difference in the planet formation histories between these two disk models.

At the water ice line, the dust density is enhanced in the new dust model. This enhancement can increase the dust-to-gas ratio up to 1-to-4 from the standard 1-to-100 that is used in CPA16, which drastically increases the rate of solid accretion in the new dust model. Because of the enhancement the planet forming at the water ice line builds a larger core and rapidly draws down an atmosphere, faster than in the CPA16 model. Formation happening quicker implies that the planet will not migrate inwards as far in the CPB17 dust model which results in the larger final semi-major axis for the planet in the water ice line.

The planet forming at the dead zone edge in the CPA16 model did not accrete an atmosphere because it spent its whole formation history far out in the disk. This is in contrast to the CPB17 model where the dead zone edge rapidly evolves inward, bringing its forming planet with it. In the CPB17 model the dead zone planet results in a mass of approximately 2 Saturn masses at ~ 0.12 AU.

The heat transition planet in the CPB17 model results in a super Earth sized planet very close to its host star. The mass of this planet is significantly smaller than its counterpart in the CPA16 model planet which is approximately 1.4 Jupiter masses. The difference between these two models is due to the evolution of the dead zone edge which crosses the position of the heat transition trap very early in the CPB17 model. In this model, the dead zone spends most of its time at smaller radii than the orbital radius of the heat transition trap. As a result the planet remains trapped at the heat transition trap location for its entire formation history, staying at larger radii than its

Table 4.3: Carbon-to-Oxygen (C/O) and Carbon-to-Nitrogen (C/N) ratios for the planets from CPA16 and this work based on the dust model from CPB17.

CPA16	C/O	C/N
Dead zone	N/A	N/A
Ice line	0.23	47
Heat transition	0.28	10
THIS PAPER	C/O	C/N
Dead zone	0.29	4.12
Ice line	0.29	4.08
Heat transition	0.29	4.17

counterpart in the CPA16 model. At larger radii, the surface density of gas and dust is lower and hence the planet has less material on which to feed.

In Figure 4.5(a) we show the resulting chemical abundances of all minor gases (most abundant gases other than H_2 and He) produced in the CPA16 model. Comparatively in Figure 4.5(b) we show the resulting chemical abundances for the planets formed in the CPB17 model. Since the planet at the dead zone edge did not accrete an atmosphere in the CPA16 model, we instead plot the abundance of ice species that were accreted and assumed 100% out-gassing. We do not believe this is an appropriate assumption for the production of an atmosphere around this planet and hence will limit our discussion to planets that directly accreted their atmosphere from the disk gas.

In our new dust model the water and CO abundances are similar because all planets accreted their atmospheric gas near or within the water ice line. As the disk ages and cools the three planet traps converge at small radii and since the heat transition and dead zone planets accrete their gas later in the disk lifetime, all planets accrete gas with similar chemical abundances.

The less dominant species show some variation between the two dust models. The heat transition planet accretes its gas at a very late time at a colder region of the disk. This results in a negligible amounts of methane and elemental hydrogen, but a small quantity of oxygen gas being accreted. The ice line planet accreted its atmosphere in less than 1 Myr in both models, however it accreted its solid core faster in the CPB17 model, and did not migrate as close to the host star as it did in the CPA16 model. Because of the slower migration the CPB17 ice line planet accreted its gas in a slightly cooler position of the disk compared to its CPA16 counterpart which resulted in less methane, but more nitrogen gas being accreted.

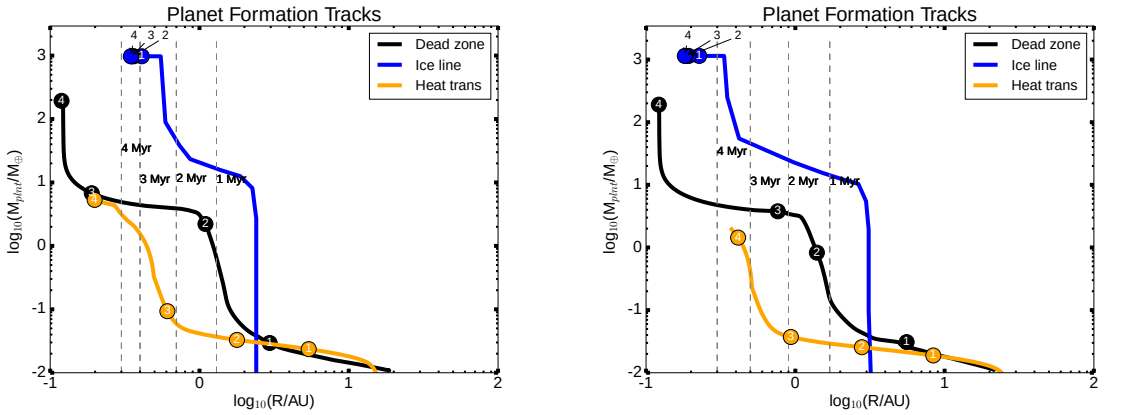

(a) Planetary formation tracks for $M_{disk,0} = 0.08 M_{\oplus}$ (b) Planetary formation tracks for $M_{disk,0} = 0.12 M_{\oplus}$

Figure 4.6: Planet formation tracks for the two additional disk models (see §4.5.2), annotated in the same as in Figures 4.4(a) and 4.4(b).

C/O and C/N Elemental Ratios

Two important tracers of planet formation history are shown in Table 4.3. The elemental ratios of carbon, nitrogen and oxygen trace *when* and *where* the planetary atmosphere was accreted. The carbon-to-oxygen ratio (C/O) indicates whether a planet accretes its atmosphere at smaller orbital radii than the water ice line, or a larger radii. Both the CPA16 and CPB17 models result in planets that accrete their atmosphere close to the water ice line in the disk, and hence they all have similar C/O which is similar to the disk's C/O (0.288). This sub-solar C/O results from our choice of initial chemical abundances which we chose to replicate the chemical state of molecular clouds (ie. Aikawa & Herbst (1999)). In doing so we assume that the chemical abundance of the gas is not reset during the disk formation process - an effect that can significantly alter the chemical state of the disk (see for ex. Eistrup et al. (2016)).

The carbon-to-nitrogen ratio is also sensitive to the location of the planet when it accreted its atmosphere relative to the ice lines of nitrogen volatiles. While the abundance of nitrogen carriers (NH_3, HCN, N_2) is dependent on when the planet accretes its gas, C/N is more dependent on our choice of disk model. In the CPB17 disk model, more nitrogen (by mass) is accreted which reduces C/N by a factor of between 2.5 and 10 relative to the results of the CPA16 model.

Table 4.4: Final planetary parameters for the models of higher and lower initial disk masses.

$M_{disk,0} = 0.08 M_\oplus$	M_{plnt} ($M_\oplus$)	a_{final} (AU)
Dead zone	197.4	0.12
Ice line	1095.0	0.98
Heat transition	6.0	0.19
$M_{disk,0} = 0.12 M_\oplus$	M_{plnt} ($M_\oplus$)	a_{final} (AU)
Dead zone	203.5	0.13
Ice line	1194.0	0.23
Heat transition	1.9	0.37

4.5.2 Varying Initial Disk Mass

As a prelude to a full population synthesis model, we present the results of two additional disk models with a higher (0.12 $M_\odot$) a lower (0.08 $M_\odot$) initial disk mass than our fiducial model (0.1 $M_\odot$).

The initial disk mass sets the normalization for the initial gas surface density profile for a given initial disk size. Because of its dependence on gas surface density, the initial mass accretion rate is also set by the choice of initial disk mass. In our disk model, the temperature of the inner ($r \lesssim 20$ AU) disk is dependent on viscous heating, and hence is also dependent on the initial disk mass. All of these dependencies conspire to change the initial location of each of the planet traps, and the formation history for the planets forming within the traps.

In Figures 4.6(a) and 4.6(b) we show the planet formation tracks for the disk models with initial mass $0.08 M_\oplus$ and $0.12 M_\oplus$ respectively. In the lower mass disk, the heat transition and dead zone planets begin at smaller orbital radii than the planets in the high mass disk. As a result the planets in the lower mass disk accrete their material in a region of the disk with higher gas and dust surface density, building the core of the planet faster. In the case of the planet trapped at the heat transition trap, because its core is built faster in the lower mass disk it has time to accrete an atmosphere. While in the higher mass disk model the heat transition planet did not. The ice line planet also accretes its core faster in the low mass disk model, the reason for this is discussed below.

The final masses and semi-major axes are shown in Table 4.4. The planet forming at the dead zone trap accretes a similar mass and ends its evolution at a similar semi-major axis in all three models. This feature is related to the strength of the dust surface density enhancement that occurs at the ice line, and the tendency of the dead zone to evolve towards this enhancement. This tendency strongly ties the evolution of both traps at the latest times in the disk, and since the planet in the

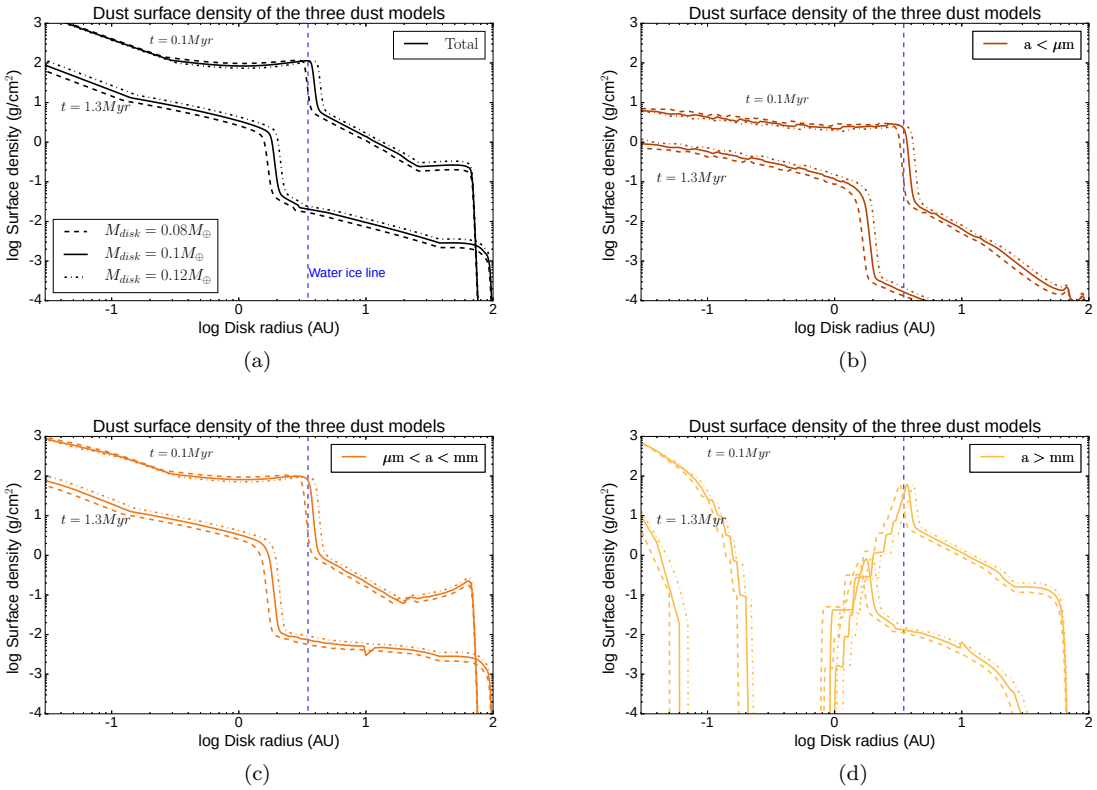

Figure 4.7: Dust surface density for the three presented models. Along with the total surface density (in black) the densities are binned into separate sizes: sub-micron, sub-millimeter and sizes greater than a millimeter. These dust surface densities are shown for two snapshots of our disk model, with 0.1 Myr represented by the top line in all figures, and 1.3 Myr represented by the bottom lines. Dust is cleared between the two snapshots because of radial drift and viscous evolution. This clearing is particularly effective on the largest grains (Figure 4.7(d)), which shows a truncation in the disk at larger radii.

dead zone trap never accretes enough material to open a gap, it is bound to the radial evolution of its trap.

At late times the viscous regime shrinks and eventually disappears completely, resulting in a disk that is heated solely by direct irradiation from its host star. The resulting temperature structure does not evolve in time and hence the location of the ice line and dead zone evolve to nearly the same radius in every disk model before ceasing its radial evolution.

Variation in Dust Surface Density Distribution

In Figure 4.7 we show the dust surface density for the three disk models shown at 0.1 Myr and 1.3 Myr. In the figures we denote the location of the water ice line for the fiducial disk model. The water ice line for the two other models is initially located at smaller orbital radii for the lower mass disk and a larger radii in the higher mass disk. In the outer disk ($r > r_{iceline}$) the dust surface density scales with the total initial disk mass with higher initial disk masses leading to higher dust surface densities, while in the inner disk ($r < r_{iceline}$) the reverse is true.

This inversion is related to the location of the ice line in each of the disk models. The radial dependence of the dust surface density is dependent on the location of the water ice line, because of its impact on the fragmentation threshold speed of the grains. Hence the radial offset between dust models is partly due to the radial offset of the water ice line. On top of the radial offset, radial drift is more efficient in the lower mass disk because of the reduced gas surface density.

The radial drift speed scales roughly linearly with the Stokes number (St, when St < 1), which describes the aerodynamically properties of the dust grain and hence the coupling to the gas. The dependency of the Stokes number on disk surface density and temperature is contingent on which physical process sets the maximum grain size. When the radial drift dominates the maximum size of the grains (ie. grains drift faster than they fragment) the Stokes number is inversely proportional to the gas surface density. However, when fragmentation dominates, the Stokes number depends only on the gas temperature (Birnstiel et al., 2012). Hence at large radii where the radial drift dominates, the lower gas surface density of the low initial mass disk results in larger Stokes numbers and more efficient radial drift. This faster radial drift brings more material to the inner disk, producing higher dust surface densities in the inner disk than the higher initial disk mass models.

The higher dust surface density in the low mass disk is what leads to the faster evolution of the ice line planet shown in Figure 4.6(a). The planet starts its gas accretion with a heavier core and hence undergoes a shorter period of slow gas accretion. Because this slow gas accretion phase is responsible for the majority of semi-major axis evolution for forming planets, the resulting gas giant does not evolve far from its initial position.

Also shown in the figure is the temporal evolution of the dust surface density distributions from the earliest time (0.1 Myr) to an intermediate time (1.3 Myr) through the lifetime of the disk. As the disk ages, radial drift and viscous evolution causes the surface density of the dust to drop at all

radii. Interestingly, the outer edge of the large dust grain disk (see Figure 4.7(d)) shrinks, while the outer edge of the intermediate sized grains ($\mu m < a < mm$, see Figure 4.7(c)) grows.

Resulting Atmospheric Chemical Abundances

In Figures 4.8(a) and 4.8(b) we show the resulting bulk chemical composition of the minor gases in each planet's atmospheres, and in Table 4.5 we show the elemental ratios. The water and CO abundances (by mass) of each of the planets are nearly equal, attributed to the fact that each planet accreted its gas near the ice line, or at smaller radii. Within the radius of the water ice line the relative abundance of water vapour and CO gas is constant.

The abundances of the nitrogen carriers do vary between the planets, in a similar manor as in the fiducial model. As in the fiducial model, in the high mass disk model the ice line planet accretes its solid core rapidly, accreting an atmosphere before 1 Myr. Early in the disk's evolution it is warmer and the nitrogen content is generally in NH_3. In the lower mass disk model the initial mass accretion rate is lower and hence the gas begins cooler. Because of its initially cooler state, nitrogen is primarily in molecular gas (N_2) rather than NH_3. This difference is then reflected in the bulk chemical composition of the water ice line planet. Additionally in the lower mass disk model the water ice line planet does not migrate very far before accreting an atmosphere, and hence it accretes its gas in a cooler region of the disk than the water ice line planets in the two other disk models.

In Figure 4.9 which is one of the key results of this paper, we show the mixing ratio of H_2O, CO_2, CO, CH_4 for our predicted atmospheres. Additionally, we show the range of mixing ratios that are inferred by retrieval studies (Madhusudhan & Seager, 2009, 2010; Miguel & Kaltenegger, 2014; Lee et al., 2012; Line et al., 2011, 2014b) of atmospheric emission spectra. We see that the H_2O and CO content in our predicted atmospheres does not vary across our three disk models. The reason for this

Table 4.5: Elemental ratios at $t = t_{life}$ from the low and high initial mass dust models

$M_{disk,0} = 0.08$	C/O	C/N
Dead zone	0.288	4.12
Ice line	0.288	4.14
Heat transition	0.289	4.13
$M_{disk,0} = 0.12$	C/O	C/N
Dead zone	0.288	4.12
Ice line	0.288	4.09
Heat transition	N/A	N/A

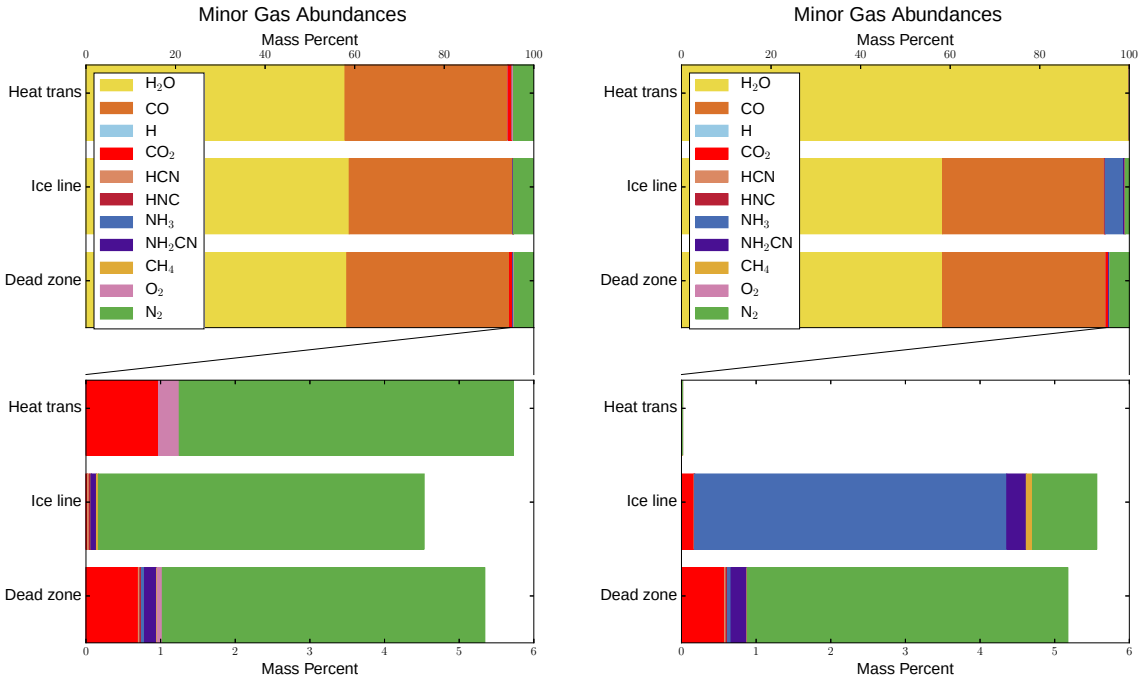

(a) Final bulk composition for $M_{disk,0} = 0.08 M_{\oplus}$

(b) Final bulk composition for $M_{disk,0} = 0.12 M_{\oplus}$

Figure 4.8: Resulting bulk compositions of minor gases for the low and high mass disk models. The atmospheres of each of the planets formed in these models had similar abundances (by mass) of water and CO because they accreted their atmospheres at similar positions relative to the water ice line. The nitrogen content shows some variation based on the timing of atmosphere accretion and the global temperature structure of their natal disks.

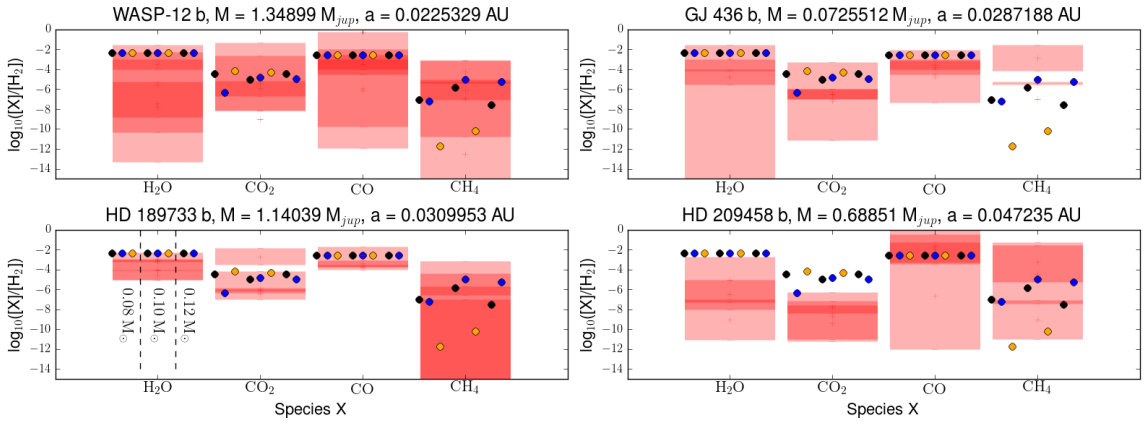

Figure 4.9: A comparison between the mixing ratios of molecules inferred by observations (red bars) with our theoretically derived planetary atmospheres. The three disk models with varying initial disk mass are shown, with the left three points represent the low disk mass, the middle three representing the fiducial mass disk and the right two points showing the high mass disk results. The colour of the points denote the planets formed in the dead zone (black), the water ice line (blue), and heat transition (orange) traps. The observational data comes from Madhusudhan & Seager (2009, 2010); Miguel & Kaltenegger (2014); Lee et al. (2012); Line et al. (2011, 2014b).

similarity is because each disk model is initialized by the same chemical abundance, and each planet accreted its atmosphere within the water ice line of their respective disks. These results suggest that as an observing tool, if the atmospheric mixing ratios of H_2O an CO are similar to the host star then this would suggest that the planet accreted its gas within the water ice line. Within the water ice line, most of the carbon and oxygen carriers are found in the gas phase (Öberg et al., 2011). Since there is little to no freeze out of carbon and oxygen carrying molecules, the chemical composition of the gas is similar to the initial conditions of the disk. This result could change if the majority of carbon and oxygen come from the late accretion of planetesimals or pebbles (for eg. Mordasini et al. (2016)). This late stage of accretion occurs after the evaporation of the gas disk and is not explored in this work.

Even with the same initial chemical abundances in each disk model we find small variations in the mixing ratio of CO_2, and large variation in the mixing ratios of CH_4. These variations are directly linked to the different formation histories, and are sensitive to *when* and *where* the planet accretes its gas. These variations do depend both on the initial mass of the protoplanetary disk and when the planet accreted its gas, which complicates future interpretation of observed chemical abundances in exoplanetary atmospheres.

4.6 Discussion

The dust component of a protoplanetary disk has important observational and theoretical effects on the structure of the disk. We have seen that the dust component of our disk models impacts the ionization structure and hence the formation history and size of planets forming in planet traps. In the context of exoplanetary atmospheres, different formation histories lead to different bulk compositions in the atmospheres of exoplanets. Understanding how differences in these bulk compositions arise could lead to a method of broadly interpreting the formation history of an exoplanet based on the observation of its atmospheric chemical content.

These interpretations are complicated by the chemical and physical evolution of the atmosphere as the planet ages, and it remains to be seen by how much these global mixing ratios are changed when the atmosphere is allowed to evolve. Of particular importance could be the interaction between the atmosphere and the core. Heavy elements in the atmosphere could be injected by out-gassing or through the erosion of the core (for ex. Ali-Dib (2017)). We leave these calculations to future work.

The fact that we form Jupiter sized planets very early ($t < 1$ Myr) in the disk lifetime has important implications on observed protoplanetary disks like HL Tau which has features that are consistent with a planet-induced gap in the dust (Jin et al., 2016). Because of its young age ($\lesssim 1$ Myr), other work has suggested that the gaps are more consistent with a change in average grain size at condensation fronts (eg. Zhang et al. (2015); Okuzumi et al. (2016)). While the condensation front interpretation of disk gaps like in HL Tau may be more consistent with reality than a planet gap, we note that the concept of a Jupiter massed planet cannot, at this stage, be disregarded as it appears to be easily produced at a water ice line that is fed a substantial amount of dust by radial drift.

4.6.1 Ubiquity of H_2O and CO mixing ratios?

For our three models presented here we find that each of the planets show similar ratios of H_2O and CO regardless of the disk model, and their C/O are similar to the ratio in the initial chemical conditions of the disk. This appears to be caused by the fact that each of the planets presented here either accreted their gas close to the location of the water ice line or at smaller radius than the location of the water ice line. The convergence of the planet traps is a feature of the particular disk models presented here, however it is not clear whether this result will stand until an exploration

through parameter space can be made.

These results contrast with some observations that suggest that planets have C/O higher than their host stars Brewer et al. (2017). If we assume that the stellar photosphere represents the chemical state of the protoplanetary disk that the planets formed from, then these observations suggest that most Hot Jupiters accreted their gas beyond the water ice line. Our work suggests that the opposite is true for the case of planet formation in the presence of planet traps. Since all of our planets either accreted their gas within or very near to the water ice line, thereby accreting 'pristine' gas - with the same C/O as their disk and host star. We note that a recent retrieval survey for eight hot Jupiters reports upper limits of C/O < 0.9 (Benneke, 2015). These results are more consistent with ours because they imply that Hot Jupiter atmospheres tend to be oxygen rich, however their atmospheric C/O is never compared to the C/O of the host star.

A method of altering the atmosphere's C/O post-formation is through the accretion of icy planetesimals (Mordasini et al., 2016). Chemically similar to comets, these planetesimals would deliver additional carbon and oxygen to the planet's atmosphere. To what extent this process would alter the observable C/O will depend on the quantity of accreted planetesimals, their chemical composition, and how deeply they travel before disintegrating (Mordasini et al., 2015). Generally, oxygen is more abundant than carbon in the frozen content of comets, which would drive C/O lower than would be accreted directly from the gas disk. This would drive C/O below unity for planets which accrete gas beyond the water ice line, and below the C/O of their host star for planets which accrete their gas within the water ice line.

The tendency of planet traps to converge to the same radius in these particular runs at late times is caused by the rapid depletion of dust in the outer disk ($r > r_{iceline}$). This latter feature of our model is inconsistent with sub-millimeter observations of protoplanetary disks, which have observed dust out to hundreds of AU. Such an issue as raised in CPB17 where we find that radial drift clears out a substantial amount of dust quickly in the outer disk. A potential fix for such a rapid clearing of material is dust trapping at pressure maxima (Pinilla et al., 2012). Indeed in our planet formation model we assume that planet traps act as these dust traps, and we enhance the density of solids accordingly. However in our model of dust evolution these traps are not implemented. A possible outcome of these traps that more solid material is maintained in the outer disk, thereby increasing the initial formation rate of planetary cores for the planets trapped at the dead zone and heat transition.

Additionally, the location and evolution of the dead zone may have an important impact on the evolution of the dust size and density distributions. As was shown in CPB17 the dead zone suppresses fragmentation and enhanced dust settling, increasing the density of large grains and reducing the density of sub-micron grains along the midplane of the disk. In a future work we will explore a model of co-evolving gas and dust to incorporate the effects of an evolving dead zone over then entire disk lifetime.

4.6.2 Variation in CH_4 as a tracer of formation history?

The carbon-carrying molecule that showed the greatest level of variation between each of our modeled planets was CH_4. Generally, we find that the planets which accreted their atmosphere in the colder parts of the disk showed the smallest mixing ratios for this molecule. This implies that an observation of a small CH_4 mixing ratio could imply that the planet formed near or outside the water ice line. We note, however that CH_4 tells you very little about *when* a planet accretes its atmosphere. As an example in the disk with initial mass of 0.08 $M_\oplus$ the ice line and dead zone planets accreted at very different times, but resulted with nearly identical CH_4 mixing ratios.

These conclusions will become complicated by the equilibrium chemistry that occurs in exoplanetary atmospheres. In equilibrium chemistry, there is a sharp transition at a temperature of ~ 750 K above which CH_4 is converted into CO (see for ex. Pignatale et al. (2011)). This transition will greatly impact our ability to observe CH_4 in Hot Jupiters because their equilibrium temperatures can exceed 1000 K (Wakeford et al., 2017).

4.6.3 Nitrogen carriers as a tracer of formation history?

With the James Webb Space Telescope (JWST) launch in 2018 we will have a new tracer of formation history, NH_3. The camera JWST-MIRI will study the mid-infrared which gives us the first chance to directly detect features caused by the presence of NH_3 in the emission spectra of atmospheres. The first possible detection of nitrogen chemistry has been recently reported by MacDonald & Madhusudhan (2017). In that work, the authors report a new retrieval technique (known as POSEIDON) which they apply to the spectra of HD 209458b. MacDonald & Madhusudhan (2017) report a range of mixing ratios for NH_3 between 0.01 - 2.7 ppm relative to the abundance of hydrogen atoms, depending on their choice of atmospheric model. Across all of our disk models presented here, we find

mixing ratios as low as 2×10^{-6} ppm, and as high as 52 ppm. These results results suggest that with current HST observations and advanced retrieval algorthims (eg. Lavie et al. (2016); MacDonald & Madhusudhan (2017)) we can begin to constrain the formation histories of observed planets with high abundances of NH_3.

As was pointed out in CPA16, the detection of NH_3 in an atmosphere might be indicative of a planet that accreted its gas early ($t < 1$ Myr) in the lifetime of the disk. A non-detection of NH_3 does not necessarily indicate a planet that accreted gas later, because some atmospheric evolution could have removed the molecule from the upper atmosphere.

4.7 Conclusions

In this work we have demonstrated that complex dust physical models can drastically change the formation history of planets forming in planet traps. With the changing formation history comes a change in *when* and *where* the planet accretes its atmosphere and hence a change in the bulk atmospheric abundances of the gas.

Changing the surface density of dust grains throughout the disk impacts the freezing efficiency of volatiles and their formation pathways which are dependent on the presence of dust. This has lead to:

- A retention of volatile H_2O and CO_2 when compared to the CPA16 (constant dust-to-gas ratio) chemical model at $r > r_{iceline}$
- An enhancement of nitrogen carriers N_2 and NH_3 are found at $r < r_{iceline}$ due to formation reactions that are catalyzed by the presence of dust

The radial drift of dust results in a rapid depletion of dust in the outer parts of the disk, and a higher ionization fraction at larger radii ($r > r_{iceline}$). These higher ionization fractions change the formation history of planets forming in our model producing:

- Hot Saturns that form at the dead zone edge
- Earth and Super-Earth sized planets at the heat transition trap
- Hot Jupiters and 1 AU Jupiters from the water ice line trap

We have begun to explore the available parameter space of disk initial masses in order to understand what range of molecular abundances could exist in an 'early' exoplanetary atmosphere. This early study has suggested that:

- The mixing ratio of H_2O and CO appear to be constant across planets that formed within the water ice line, and produce C/O that are the same as the ratio of the protoplanetary disk
- CH_4 shows a large variation between different formation histories and is tied to the planet's proximity to the disk's water ice line
- NH_3 could act as a measure of *when* the planet accretes it's gas
  - Earlier on, the disk is warmer and NH_3 dominates the nitrogen carriers
  - Later the disk cools and the nitrogen is found predominately in molecular nitrogen gas

Understanding the differences in the abundance of elemental carriers is important as next generation of telescopes come online and begin to observe the emission spectra of exoplanetary atmospheres. As the library of detectable chemical species grow our models can evolve to understand where the observable diversity of chemical species arise.

Chapter 5

Application of Planet Formation to the HL Tau System

In the following chapter we present some preliminary work applying our theoretical model to a real, well studied system - HL Tau. What follows represents a version of an upcoming paper that is still in preparation.

5.1 Introduction

Can the existence of planets explain the features observed in the disk around HL Tau? This question was soon asked after the release of the exquisite, high resolution image of the circumstellar (also known as protoplanetary) disk by the Atacama Large Millimeter Array (ALMA) (ALMA Partnership et al., 2015). The ALMA image shows that the disk has an approximate radius of 100 AU and has uncovered 5 gaps in the disk which have yet to be fully explained. If each of the 5 gaps in the disk contained a planet, Tamayo et al. (2015) analyzed the dynamical stability of a possible planetary system within these gaps and placed upper limits of about a Saturn mass for the three outer planets. Left out of their analysis was the formation process which would lead to the existence of these planets, especially given that the HL Tau system is young ($t_{age} \sim 1$ Myr).

In this chapter we study the formation of planets that are dynamically trapped at 'planet traps' in the HL Tau disk. We ask the questions: what planetary masses could form within the predicted

age of the HL Tau system? And can the gaps in HL Tau be explained by the presence of new planetary embryos in the process of forming? We posit that a planet embryo can form at the ice line of abundant volatiles due to the efficient growth of dust grains covered in an ice mantle (see e.g. Ros & Johansen (2013)). These embryos would perturb the gas creating pressure maxima towards which the dust will flow, creating the gaps (Dipierro et al., 2015). We investigate whether a planet can form in the planet formation model that was have developed in Cridland et al. (2016, 2017a,b) which combines the planetesimal accretion model (Kokubo & Ida, 2002; Ida & Lin, 2004) with a planet trap model to limit the inward migration rate of the proto-planet (Masset et al., 2006; Hasegawa & Pudritz, 2013).

We have combined this formation model with an evolving astrochemical model to study astrochemical properties of the disk in which the planet forms, and track the chemical abundance of the gas that is accreted onto the planet. The general conclusion of our past work is that the chemical composition of the atmosphere will depend on *where* and *when* a planet accretes its gas. These details depend on the formation history of the planet, and as a result depends on the physical properties of its disk.

In this work we confront our model with the HL Tau system by tuning our initial conditions to match the observed properties (system age, total gas mass) of the HL Tau disk. The purpose of this work is to: 1) explore the possible existence of planets in the HL Tau system and their role in shaping the structure of the disk, 2) report the correspondence between our derived ice line radii and the observed gaps, and 3) predict the chemical composition of their atmospheres.

The correspondence between the gaps in the HL Tau disk and volatile condensation fronts have been studied previously by Zhang et al. (2015). They used a temperature profile derived from a 2D radiative transfer model and placed ice lines at the radii where the gas reached the sublimation temperature of a number of abundant volatiles. Here we derive the radial locations of ice lines by computing the astrochemistry of our evolving analytic disk model that prescribes the gas temperature and density profile throughout the lifetime of the disk. We will compare our work to the results of Zhang et al. (2015).

The paper is organized as follows: in §5.2 we outline background information relevant to this paper and outline the disk parameters. In §5.3 we report the planets that are formed in our disk models, while in §5.4 we report the resulting chemical composition of the planets' atmospheres. In §5.3.1 we compare the radial location of the ice lines in the disk to the locations of the dust gaps

observed by ALMA. In §5.5 we discuss the relevance of our results and outline future works.

5.2 Model Background

Generally speaking our theoretical framework is an 'end-to-end' analysis that links an analytic gas disk model, a numerical dust physics code, a Monte Carlo radiative transfer scheme, a non-equilibrium astrochemical code, and a planet formation model (for technical details see Cridland et al. (2016) and Cridland et al. (2017a)). A similar, but more extensive, method has been developed by Mordasini et al. (2016), which they call a 'chain' model, in which they also included the equilibrium structure and chemistry of the resulting planetary atmosphere. In this framework, physical and chemical models are computed in succession - like links in a chain - such that the results of one model can impact the results of the next. The ordering of our model is: *gas disk model* $\rightarrow$ *dust model* $\rightarrow$ *UV / X-Ray radiative transfer* $\rightarrow$ *non-equilibrium chemistry* $\rightarrow$ *core accretion planet formation*. Each link in the chain depends on the links before it, but can not impact the results of any following links. In doing this we can successively model complicated interactions like the impact of the dust on the radiative transfer of high energy radiation. However, we must ignore other interactions like the complicated structure of the turbulence (like the existence of dead zones) on the physics of the dust.

The details of our model are outlined in Cridland et al. (2016), Cridland et al. (2017a), and Alessi et al. (2017), here we will discuss some of its important features. The gas disk model is a self-similar, analytic model as seen in Chambers (2009). It computes the co-evolving radial structure of the gas surface density and temperature as mass viscously accretes through the disk. The radial structure follows a power law of the form:

$$\Sigma(r,t) \propto \Sigma_0(t) r^{-s} \quad T(r,t) \propto T_0(t) r^{-\beta}, \tag{5.1}$$

where the exponents s and β are determined by the heating source and the time dependent functions Σ_0 and T_0 depend on the mass accretion rate. There are two primary heating sources in an accretion disk, viscous evolution and direct irradiation. The latter is caused by the loss of gravitational energy as the gas accretes through the disk, while the former is caused by the absorption and re-emission of stellar radiation by the upper atmosphere of the disk. Generally speaking, viscous heating dominates

the inner region of the disk, while direct irradiation becomes important at larger radii. There is a radius at which the heating from direct irradiation becomes more important than the heating from viscous evolution. We call this radius the heat transition (r_t), so generally the surface density and temperature of the gas is given by:

$$\frac{\Sigma}{\Sigma_0}(r) \propto \begin{cases} r^{-s} & r < r_t \\ r^{-s'} & r > r_t \end{cases} \tag{5.2}$$

$$\frac{T}{T_0}(r) \propto \begin{cases} r^{-\beta} & r < r_t \\ r^{-\beta'} & r > r_t \end{cases}, \tag{5.3}$$

where $s = 3/5$, $\beta = 9/10$, $s' = 15/14$, and $\beta' = 3/7$. As the mass accretion rate drops, viscous heating becomes less important, and eventually the temperature structure is dominated by direct irradiation.

The dust is allowed to evolve separately from the gas, and its evolution depends on the level of coupling between a dust grain and the gas. The parameter which describes this coupling is known as the Stokes number - the ratio of the grain stopping time to eddy turnover time:

$$St = \frac{a\rho_s}{\Sigma}\frac{\pi}{2}, \tag{5.4}$$

where a is the radius of the grain, ρ_s is the internal density of the grain, and Σ is the gas surface density. When $St < 1$ the grain is well coupled to the gas and will primarily evolve viscously. While when $St > 1$ the dust will decouple from the gas and orbit the host star in Keplarian orbits. Because the gas is pressure supported and orbits at sub-Keplarian the most important consequence of the grains decoupling is that they will feel a head wind as they pass through the gas. This head wind drains angular momentum and forces the grain to lower orbits. This process is known as radial drift, and proceeds on a time scale of:

$$\tau_{drift} = \frac{rV_k}{Stc_s^2}\gamma^{-1}, \tag{5.5}$$

where V_k is the Kepler speed, c_s is the gas sound speed, and γ is the adiabatic index. Radial drift plays an important role in our model because it impacts both the radial structure of the dust, which

changes the flux of high energy radiation, and provides ample solid material for the formation of planetary cores at small radii (Cridland et al., 2017a). It does, however, clear out the solid material at large radii, and makes planet formation through the accretion of planetesimals more difficult far out in the disk.

We compute the transfer of UV and X-Ray radiation because of its importance on the astrochemistry in protoplanetary disks (Fogel et al., 2011). We use the Monte Carlo radiative transfer scheme *RADMC3D* (Dullemond, 2012) to compute the flux of photons through out the disk. To properly model the flux from a T Tauri star we compute the radiative transfer for four wavelengths within a range of 930-2000 Å for UV and 1-20 keV for X-Rays. We then extrapolate the remaining wavelengths within the above ranges using a sample spectrum as seen in Fogel et al. (2011) and Bethell & Bergin (2011a). These sample spectra have been normalized to match the total flux from TW Hya, and can be scaled if needed.

The astrochemistry is computed with a non-equilibrium gas chemistry code as featured in Fogel et al. (2011), Cleeves et al. (2014), and Cridland et al. (2016). Generally it computes the reaction rates of many ($\sim$ 5900) chemical reactions including gas phase, grain surface, and photo-chemistry. We allow for the chemical structure of the disk to evolve with time by selecting a number of 'snapshots' of the gas surface density and temperature. Each snapshot is spaced out in time by $\sim$ 17000 yr, and includes gas density and temperature profiles, a dust density profile, and the UV and X-Ray radiation fields. Each of these profiles change from one snapshot to the next, so we compute the chemistry from the same initial condition to a steady-state solution in each snapshot. This method allows the chemistry to be computed in parallel over many snapshots simultaneously, which dramatically reduces the required computing time.

The reaction rates that are used to compute the adsorption and desorption of volatiles are based on lab measurements of ice binding strengths, and hence have associated uncertainties. We have not propagated these uncertainties through our calculation of the ice lines radial location (see below), and hence we can not estimate the uncertainties in the radial location of the ice lines. Additionally we assume that all ice is pure when it desorpts - which ignores the desorption of clathrate hydrates (as explored by Zhang et al. (2015)), mixes of water ice with trapped gaseous molecules. These species of water ice generally have lower sublimation temperatures than pure water ice, and hence could produce additional ice lines or shift the location of the ice lines that are computed below.

Our planet formation model follows the standard core accretion model (Kokubo & Ida, 2002;

Ida & Lin, 2004), and includes dynamical trapping of the forming planets in 'planet traps'. Planet traps slow the Type-I migration rate of proto-planets because of a combination of the Lindblad and co-rotation torques (Masset et al., 2006; Hasegawa & Pudritz, 2013). Specifically, planet traps are discontinuities in the physical properties of the disk which causes the direction of the net torque acting on the planet to reverse direction. The three planet traps which we focus on are the water ice line, the heat transition, and the outer edge of the dead zone. The discontinuities associated with these traps are in the dust opacity, gas temperature profile, and gas turbulence respectively. Importantly, because this process occurs late in the chain model, we note that some of these discontinuities are not accounted for in computing the radial structure of the gas and dust. In our model we assume that the planet is trapped at each planet trap, and migrates along with the evolving location of the planet trap as long as the co-rotation torque remains unsaturated (Paardekooper et al., 2010; Hasegawa & Pudritz, 2013; Coleman & Nelson, 2016). The saturation of the co-rotation torque depends on the strength of the gas turbulence, and so at each snapshot we check the saturation of the co-rotation torque if the planet trap is found within the dead zone (see Cridland et al. (2016) for details).

If the co-rotation torque saturates, the proto-planet migrations at the standard Type-I rate (Seager, 2010):

$$\frac{1}{r_p}\frac{dr_p}{dt} = \frac{C_T \Sigma \Omega_p r_p^2}{M_p}\left(\frac{M_p}{M_*}\right)^2\left(\frac{r_p}{max(H, R_H)}\right)^2, \tag{5.6}$$

where r_p, Ω_p, and M_p is the radial position, Keplar frequency, and mass of the planet, H is the scale height of the gas, and R_H is the Hill radius of the planet. The numerical constant C_T is related to the strength of the net torques on the planet (ie. see Paardekooper et al. (2010)).

When the planet is sufficiently massive, its gravitational tug on the surrounding gas and dust will overpower the viscous torques and open a gap in the disk. At this point Type-I migration is suppressed and the planet begins Type-II migrating. In this regime, the planet migrations inward on the viscous timescale, as it acts as an intermediary to angular momentum transport throughout the disk. In this case the orbital radii of the planet evolves as:

$$\frac{1}{r_p}\frac{dr_p}{dt} = \frac{\nu}{r_p^2}, \tag{5.7}$$

where ν is the gas viscosity. Because we assume that the disk is a standard 'α-disk' (Shakura &

Sunyaev, 1973), $\nu = \alpha c_s H$.

5.2.1 Planet Formation in HL Tau

For our purpose of testing the feasibility of planet formation in the HL Tau system, we wish to match the properties of our disk model as close as possible to the observed properties of the HL Tau disk. Generally the most important disk parameter in our model is the initial mass of the disk. Unfortunately this is impossible to constrain observationally for any individual system. Instead we pick initial masses that result in the observed gas mass range of the HL Tau disk at a disk age of ~ 1 Myr. We used the stellar parameters outlined by White & Hillenbrand (2004), and a total dust mass of (1-3)$\times 10^{-3}$ $M_\odot$ (Carrasco-González et al., 2016) to estimate a total gas mass of 0.1-0.3 $M_\odot$ assuming a global gas-to-dust ratio of 100. Assuming that the disk is 1 Myr old then its initial gas mass must have been 0.25-0.63 $M_\odot$ according to our gas disk model. To account for the range of disk masses, we run three models with initial mass of 0.25 $M_\odot$, 0.44 $M_\odot$, and 0.63 $M_\odot$, that we define as the 'low-mass', 'mid-mass', and 'high-mass' models respectively.

Each of these initial masses are larger than any of our previously tested models. And hence, we checked the initial gravitational stability of each of these models. Based on the standard Toomre Q stability analysis we found that initially the low, mid, and high mass models are gravitionally stable within radii of 38, 32, 26 AU respectively. Outside of these radii the disks are gravitionally unstable and will produce mass accretion rates that are larger than are computed by our disk model. These higher accretion rates will raise the temperature of gas which will shift the location of the ice lines outwards from where our disk model will predict. At 1 Myr, the low and mid-mass models are both fully stable, while the high-mass disk model is stable within 46 AU.

The observed UV flux of HL Tau (Bitner et al., 2008) is approximately 100$\times$ the observed flux from TW Hya (Yang et al., 2012). So we scale the UV spectrum by a factor of 100 in our radiative transfer scheme. To facilitate comparison to our past work, where we assumed the total UV flux was the same as TW Hya, we ran a second high-mass model where we do not scale the UV spectrum. We summarize the varied parameters in Table 5.2.1.

Table 5.1: Varied model parameters between the four models

Name	Initial Gas Mass ($M_\odot$)	UV Luminosity ($L_{UV,TW\ Hya}$)
low-mass	0.25	100
mid-mass	0.44	100
high-mass	0.63	100
low-flux	0.63	1

5.3 Results: Planet Formation in the HL Tau System

We run each of our models over 2 Myr to account for any possible discrepancy in the observed age of the HL Tau system and report the final mass and semi-major axes at both 1 and 2 Myr in Table 5.2. A lifetime of 2 Myr is half of the lifetime that we assumed in our past work, and as a result we found that only one planet trap in each disk model produces a planet with any appreciable size. In each model the planet trap which resulted in a planet with $M > 1\ M_\oplus$ at 2 Myr is the dead zone trap. Each of the other traps would have required more time to form a large planet.

In Figure 5.1 we show the 'planet tracks' for the forming planets - the evolution through the mass-semi-major axis diagram. Generally speaking the lower disk mass models had smaller dead zones, because their gas surface densities are lower, resulting in a higher flux of radiation at the disk midplane. This is seen in the figure since planets forming in the lower mass disk begin their evolution at smaller radii than the larger mass models. The high-mass and low-flux model began their formation at the same radii, but because the high-mass model had higher UV flux, the disk tended to be more ionized throughout the evolution of the proto-planets. As a result the dead zone moved inward faster in the high-mass model, producing a larger massed planet at 1 Myr than the low-flux model.

We note the location on the formation tracks of the planets at the current age of HL Tau (1 Myr). We find that the mid-mass model could produce a large ($M \sim 5.2\ M_{Jup}$) planet at a radius of about 2 AU. This planet is well within the resolution of the VLA and ALMA and does not coincide with the orbital radii of the gaps observed by ALMA Partnership et al. (2015). Tamayo et al. (2015)

Table 5.2: Planet orbital properties at 1 and 2 Myr

Name	$M_{t=1Myr}$ ($M_\oplus$)	$r_{t=1Myr}$ (AU)	$M_{t=2Myr}$ ($M_\oplus$)	$r_{t=2Myr}$ (AU)
low-mass	0.36	2.2	1.67	1.3
mid-mass	1658	2.0	1658	1.5
high-mass	44.9	2.1	1919	1.3
low-flux	8.7	2.2	1500	1.1

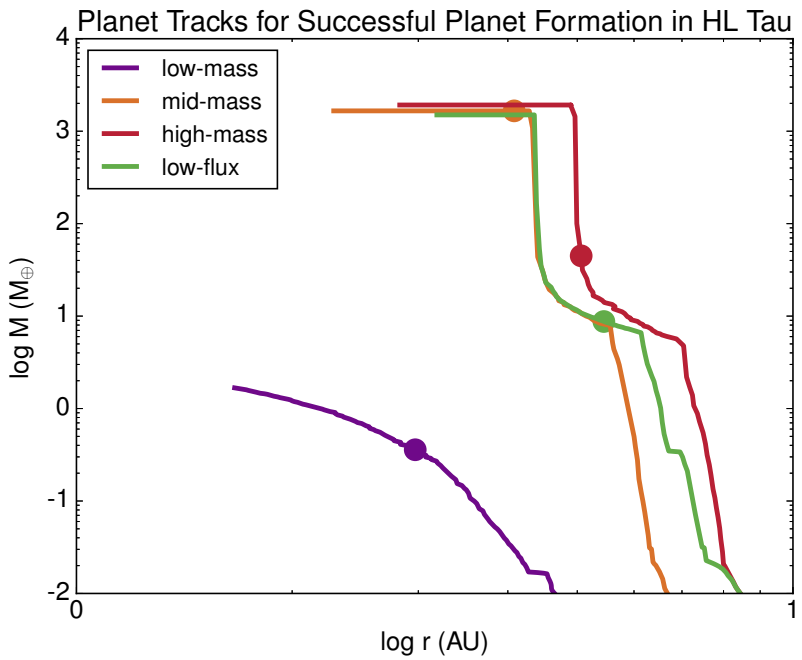

Figure 5.1: Planet formation tracks for the planets formed in the four disk models. The full tracks evolve for 2 Myr, and we note the location of the planet along each track at 1 Myr with a point.

estimated the radii of the main gaps to be: 13.6, 33.3, 65.1, 77.3, 93.0 AU. None of these gaps could be inhabited by a planet in our model, because the densities are too low at these radii in the disk for a planet to have formed through the accretion of planetesimals in only 1 Myr. Pebble accretion could lead to the formation of planets at large radii (Bitsch et al., 2015) within the lifetime of HL Tau, however we do not investigate their formation model here.

5.3.1 Dust Gaps in HL Tau

We investigated the possibility that the dust gaps are caused by the presence of embryos trapped in mean motion resonances with the unseen planet formed in our mid-mass model. We can rule this out as a possibility because no low order resonances were found to coincide with the location of any gap (see section 5.6).

A more viable explanation for the gaps is a presence of a planetary embryo located at the condensation fronts (ice line) of abundant volatiles. It has been demonstrated that dust grain growth can be very efficient around condensation fronts, driven by the formation of ice mantles on

dust grains (Ros & Johansen, 2013; Stammler et al., 2017). The growth of these grains would then be enhanced by the streaming instability, rapidly producing planetary embryos (Schäfer et al., 2017) and possibly planets (Hasegawa & Pudritz, 2013; Ali-Dib et al., 2014; Cridland et al., 2016; Alessi et al., 2017).

The coincidence of the dust gaps and condensation fronts has been previously discussed in Zhang et al. (2015) who used the temperature profile $665(r/\mathrm{AU})^{-0.6}$ K to determine the radial location of the ice lines. This profile was determined through a 2D radiative transfer model designed to model the observed SED of the HL Tau system (Men'shchikov et al., 1999).

By comparison at 1 Myr the temperature profile in our high-mass disk model is $630(r/\mathrm{AU})^{-0.9}$ K when $r < r_t$ and $24(r/40\mathrm{AU})^{-0.42}$ K when $r > r_t$. We see that in our model the temperature profile is cooler at all nearly all radii with a steeper, then shallower temperature profile in the viscously and irradiatively heated regions respectively. In this way our temperature profile is nearly always cooler than the profile used in Zhang et al. (2015), other than very near ($r < 0.8$ AU) and very far ($r > 25000$ AU) from the host star.

Zhang et al. (2015) report that the location of the inner two gaps correspond to the water and hydrated NH_3 ice lines respectively. They report the start of a large outer gap at the CO_2 ice line and is centered on the sublimation temperature of a combination of CO and N_2 on a water ice mantle. This large gap spans the radii between the third and fourth gap from Tamayo et al. (2015). The fifth gap is not represented in Zhang et al. (2015). An important distinction between the results of Zhang et al. (2015) and our own work is that they considered the freeze out of hydrated species of volatiles, as well as the freeze out of volatiles on already established icy mantles - resulting in sublimation temperatures that are higher than pure volatile freeze out.

In Figure 5.2 we compare the radii of the condensation fronts for abundant volatiles in our chemical model and heat transition radius to the locations of the dust gaps in HL Tau for each of the 4 initial disk models. Generally we find that the CO_2 is located closest to the inner gap, rather than the water ice line. This is attributed to our disk models consistently being cooler than the disk model assumed in Zhang et al. (2015) outside of 1 AU. In the high-mass and low-flux models the CO_2 ice line is more coincident to the inner gap than the two lower mass models. Again this is attributed to the cooler temperatures in these models. The second gap lies closest to the NH_3 ice line in each model, while in the high-mass and low-flux models the CH_4 ice line also lies close to the second gap.

The freeze out of pure CO occurs at the same radius ($\sim$ 73 AU) in each of our models, and is located near the fourth gap. Based on the surface brightness profile that is reported by Zhang et al. (2015) and the fact that the three outer gaps are only near the CO ice line it is unlikely there gaps are caused by planets. Interestingly, N_2 never produces a traditional 'ice line' - where the frozen phase is more abundant than the gas phase. However its ice phase reaches a maximum at $\sim$ 90 AU in each of the models. Because its sublimation temperature is generally slightly lower than CO, its clear that non-equilibrium effects like photo-desorption are pushing the N_2 ice line far from the host star. Recall that the high-mass model is gravitationally unstable outside of 46 AU which would cause a higher accretion rate, and gas temperature, possibly shifting the CO ice line outward, closer to the fourth gap.

In figure 5.3 we show the time evolution of the ice line location and how they relate to the location of the gaps in the HL Tau disk. In showing their temporal evolution, we look for an epoch when the ice lines best agree with the location of gaps in the disk. Both the high-mass (and low-flux) and mid-mass models show an instance when the ice lines best agree with the gaps at ages $\sim$ 0.8 Myr and $\sim$ 0.4 Myr respectively. Because its predicted age lies closest to the observationally determined age of the HL Tau system ($\sim$ 1 Myr) the results of our high-mass model is the most likely. Interestingly, more ice lines are coincident with disk gaps in the mid-mass model, however its predicted age is less than half of the assumed age of the HL Tau system. Clearly there is a degeneracy when comparing the locations of ice lines between different disk models between the system's age and the initial gas mass.

The heat transition acts as a dynamical trap for Type-I migration, and a site of planet formation. In the low-mass model the heat transition is located at the same radius as the inner gap (at 1 Myr), while in the high-mass and low-flux models the heat transition is located near the second gap.

The process of planet trapping at ice lines is determined by an opacity transition which locally changes the power law index of the temperature and gas density profiles. To sufficiently change the opacity across an ice line, one would expect that the volatile must be abundant in the disk gas. Water is the standard ice line trap, because of its abundance, and can effectively change the total opacity of the dust (see Miyake & Nakagawa (1993)). A primary parameter in the Miyake & Nakagawa (1993) opacity model is the mass fraction of ice in the ice-grain mixture. Across the ice line, the mass fraction of the ice changes, and so we can compute the total opacity of the ice-grain mixture as a function of radius across the ice line. With this radially varying opacity one can then compute

the temperature and gas surface density profiles in a similar manner as was done in our disk model. Using these new temperature and surface density profile the total torques can be computed using the work of Paardekooper et al. (2011) and Coleman & Nelson (2014). We will leave this analysis to future work.

Because of its dependence on the mass fraction of ice, only abundant volatiles should produce planet traps at their ice lines. Hence the CO ice line could in principle also act as a planet trap, and indeed it has been proposed to be the sight of formation for Uranus and Neptune in our own solar system (Ali-Dib et al., 2014), however we will leave this to future work. Lower abundance volatiles, however, are less likely to act as planet traps because their freeze out will not dramatically change the total opacity of the solids.

While the inner two gaps lie near to the location of the CO_2 and CH_4 ice lines, the low abundance of each of these volatiles imply that those features are likely not the result of trapped planets. The third and fourth gaps surround the location of the CO ice line, and could be caused by the presence of a planet near the CO ice line trap. Recently its been demonstrate through numerical simulations that a single planet can be produce two observable gaps in their protoplanetary disk (Dong et al., 2017).

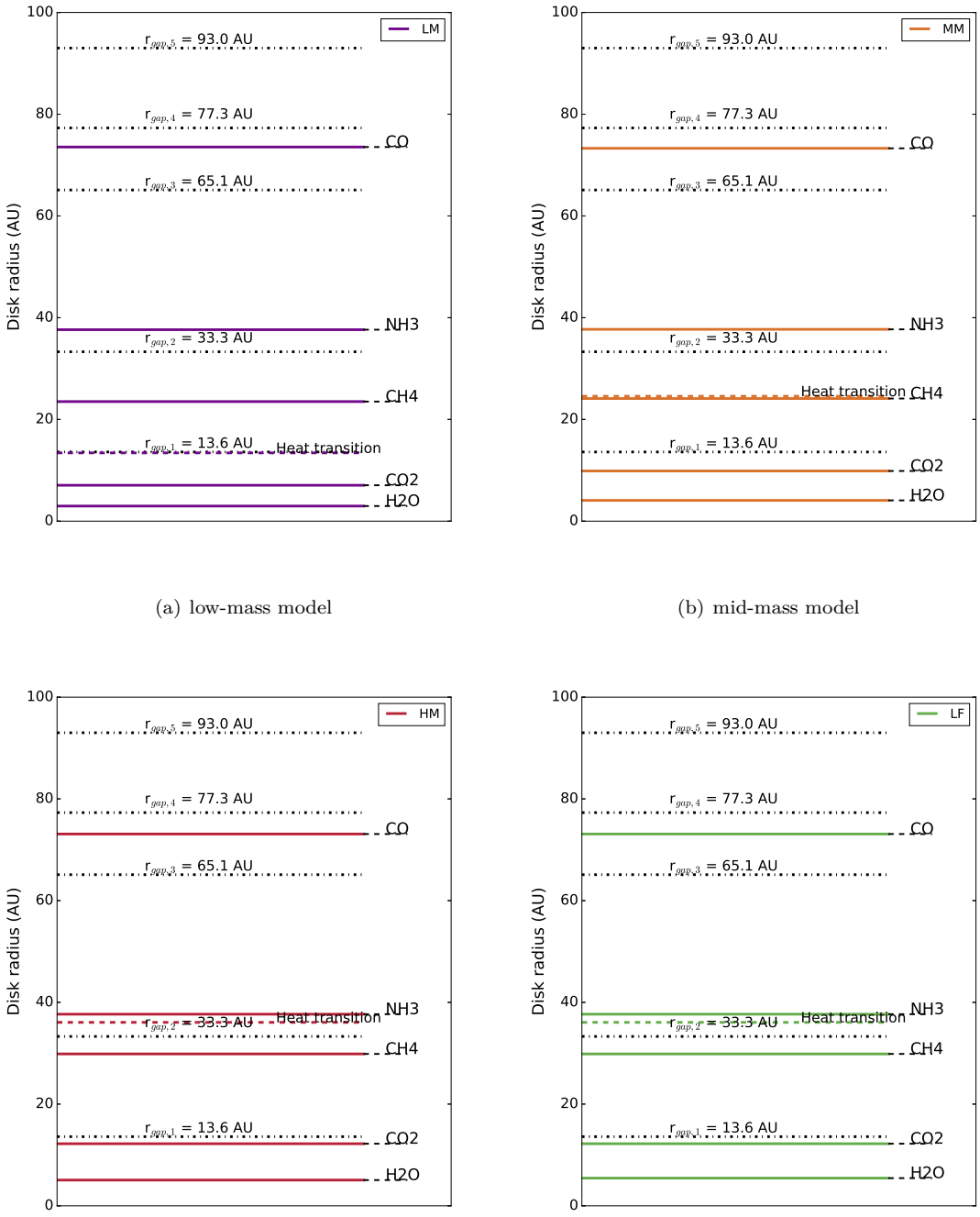

(a) low-mass model

(b) mid-mass model

(c) high-mass model

(d) low-flux model

Figure 5.2: Radial locations of the condensation fronts of abundant volatiles (coloured solid) and heat transition (colour dotted) for each of our models at 1 Myr, along with the location of the dust gaps (dotted black) in HL Tau.

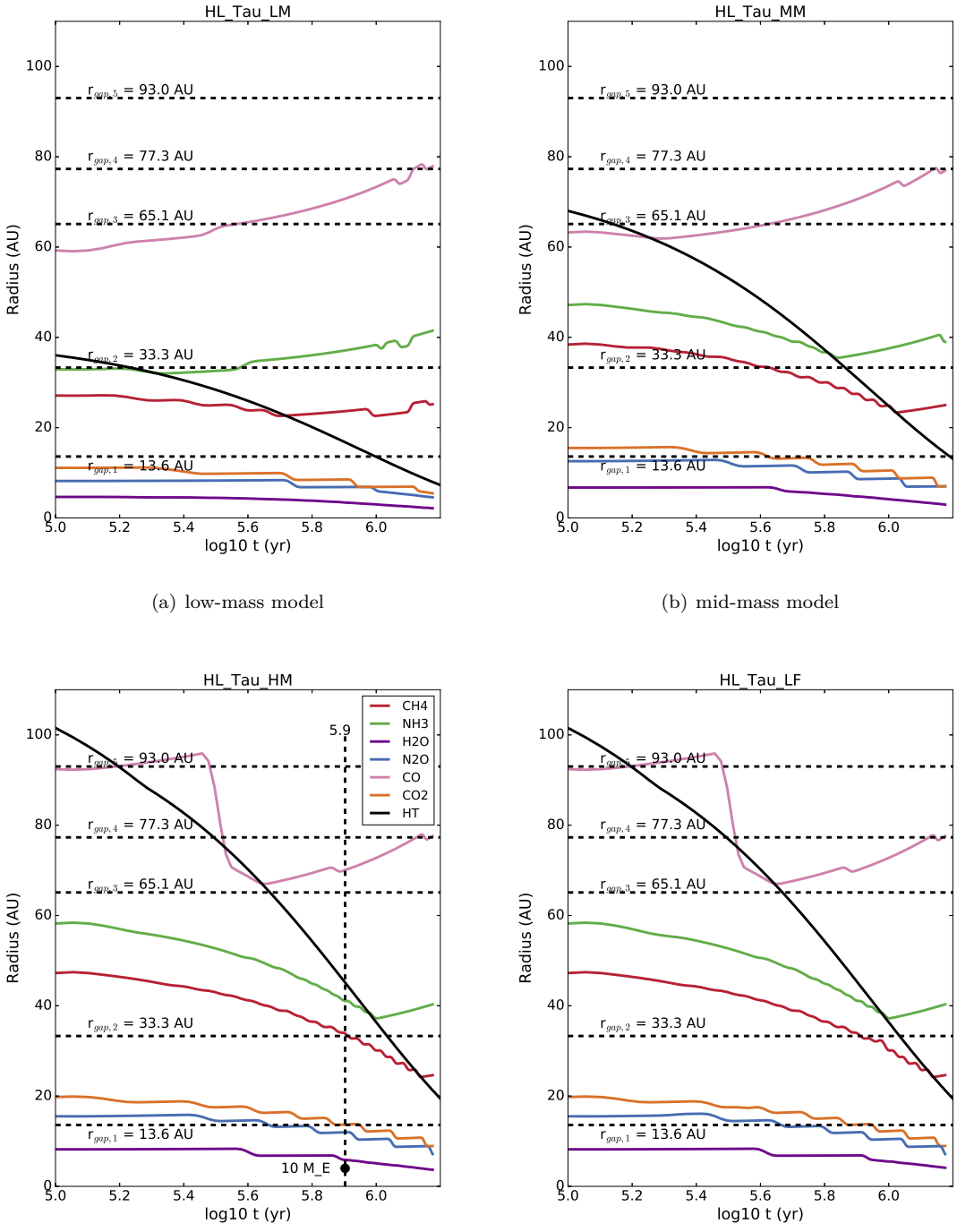

(a) low-mass model

(b) mid-mass model

(c) high-mass model

(d) low-flux model

Figure 5.3: Temporal evolution of the ice line location in each of the presented disk models. We find that in the high-mass model there is a coincidence between the location of the CO_2, CH_4 ice lines with the inner two gaps at a disk age of $\sim$ 0.8 Myr (marked by a vertical dashed line). A similar coincidence is found in the mid-mass model at an age of ~ 0.4 Myr.

5.4 Results: Atmospheric Chemical Composition

Of the four models that we tested, 3 of the models produced planets which were large enough to accrete gas, the low-mass model did not. In both the mid-mass and high-mass models the disk's initial C/O and C/N was 0.4 and 4 respectively. While in the low-flux model we used the same chemical initial conditions as in our previous work: C/O = 0.29, C/N = 4.

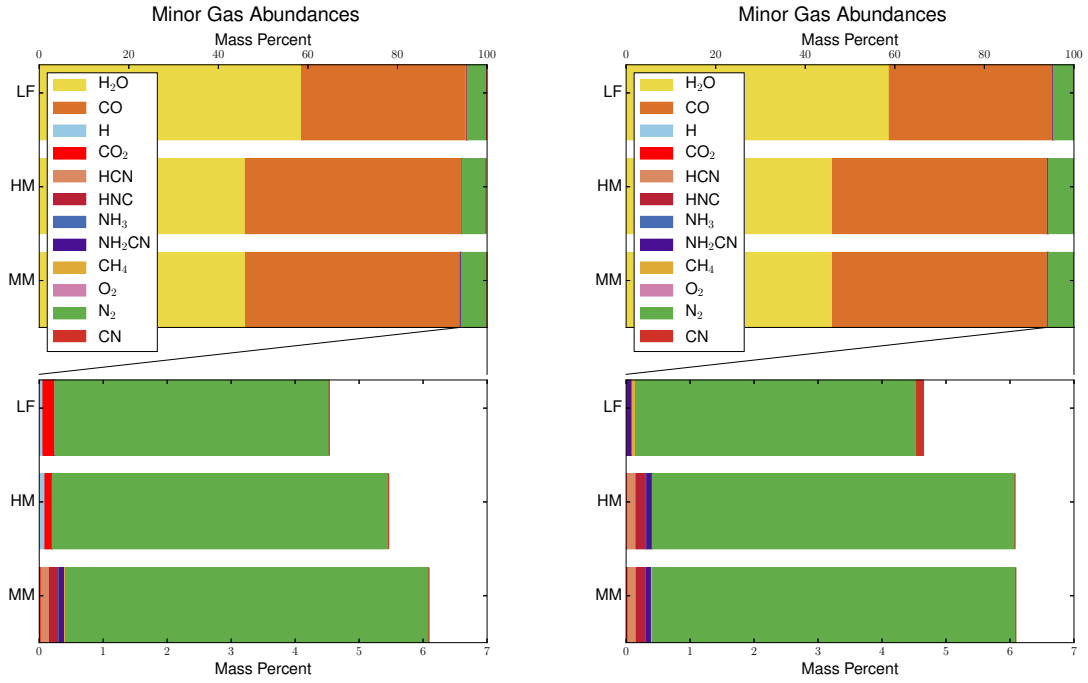

(a) t = 1 Myr (b) t = 2 Myr

Figure 5.4: Mass abundances of minor gases in each of the planets which formed in the mid-mass (MM), high-mass (HM), and low-flux (LF) models. In the top panel we show all of the other gases other than H_2 and He. In the lower panels we remove H_2O and CO to see the mass abundance of the least abundant gas species. We show the chemical composition of each planet at the lifetime of HL Tau (1 Myr, left) as well as at the end of the simulation (right).

In Figure 5.4 we show the mass abundance of all gas species that are the most abundant in the atmosphere other than H_2 and He at the age of HL Tau, and the end of the simulation. We call these gases the minor gases, which make up approximately 0.5% of the total gas mass. The most abundant of these minor gases have mass abundances of at least 0.01% of the minor gas mass in order to appear on the figure. We find that $C/O_{planet} = C/O_{disk}$ and $C/N_{planet} = C/N_{disk}$ for all three planets. This result is consistent with our previous work (Cridland et al., 2017b) and is caused

by the dead zone trap crossing inward of the water ice line by the time that the planets begin their gas accretion. In doing so, the planet accretes 'pristine' gas that has the same elemental abundances as the disk does initially. We have found a similar result in our past work - all planet traps tend to move inward at different rates, with the water ice line moving the slowest. The statistical significance of this result will only be known after we have run a comprehensive population synthesis suite. The faster migrating dead zone and heat transition traps tend to start farther out ($\gtrsim$ 10 AU) but catch up to the water ice line within 2 Myr, depending on the initial mass of the disk model. At large radii the solid accretion rates are slower, suppressing the initial growth of the planetary core. While a planet may begin its life well outward of the ice line, it does not begin efficiently accreting material until it has moved closer to the water ice line.

We find a small variation in the oxygen and nitrogen baring molecules between 1 and 2 Myr. At 1 Myr the high-mass and low-flux models are at an early stage in their gas accretion, and show a small amount of CO_2 and H in their atmosphere, while accreting almost no additional nitrogen carrying species (other than N_2). The mid-mass model has completely formed by 1 Myr, and shows no sign of CO_2. This implies that CO_2 makes up less than 0.01% (by mass) of the minor gases in the atmosphere. By the end of the simulation the high-mass model planet has accreted nitrogen carriers like HCN, HNC, and NH_2CN. These species are apparently accreted late in the planet formation process because the high-mass and low-flux planet only show the emergence of those nitrogen carriers by the end of the simulation. Furthermore it is evident that a negligible amount of CO_2 and H is accreted late in the planet formation process because by the end of the simulation these chemical species have abundances less than 0.01% (by mass) in the high-mass and low-flux models.

In the low-flux model we see the first evidence of UV-photolysis affecting the chemical compositions of the gas that is accreted by our simulated planets. With the abundance of CN and dearth of HCN and HNC relative to the other models, this planet appears to have accreted some of its gas from a region of the disk that has been chemically altered by the photodissociation of HCN. Given that the low-flux model actually has a *lower* UV flux than the other models presented here, this conclusion is surprising because we would expect the effects of photochemistry to be lower with the lower stellar UV flux. However it does imply that small variations in atmospheric chemistry can result from the complicated connection between astrochemistry and planet formation history.

5.5 Conclusions

In this chapter we have started to apply our theoretical model that is designed to combine the physical processes of planet formation with astrochemical process of accretion disks to the protoplanetary disk system HL Tau. We have applied this model to a small subset of planet formation parameter space, so in the interest of understand what range of atmospheric chemistry might arise from the planet formation process we have begun to explore the range of physical properties of known protoplanetary disks. Because of its most recent extensive study, we began this work by selecting initial disk masses such that the total mass of our computed disks match the range of masses that have been inferred in the HL Tau disk. This study has an additional application in studying the possibility that the observed dust gap structure may be due to mean motion resonance (MMR) interactions between the dusty disk and a yet unseen planet close to the star.

This work focused on answering the following questions:

- Can a planet form in this young ($\sim$ 1 Myr) disk through the accretion of planetesimals?
- Do the radial locations of the dust gaps coincide with features in our disk model?
- How do the atmospheric chemical abundances in these planet fit with our previous results?

We conclude that:

- Planet formation through the accretion of planetesimals produces up to a 5 $M_{Jupiter}$ planet within the 1 Myr predicted age of the HL Tau system in the mid-mass disk model
- The innermost gap in the HL Tau disk lies closest to the CO_2 ice line in all of our disk models
  - The correspondence at 1 Myr is best in the high-mass and low-flux models
  - The inner gap corresponds to the location of the heat transition planet trap in the low-mass model
- The second gap lies closest to the NH_3 and CH_4 ice lines
- The third and fourth gaps surround the location of the CO ice lines in each model, and could represent the effect of a trapped planet at the CO ice line
- The outer most gap is not associated with an chemical feature in our model

- The best correspondence between gap locations and volatile ice lines is found in the high-mass model at a system age of ~ 0.8 Myr
- The planet formed in each of our disk models are chemically similar to the results of our previous work
  - With C/O and C/N that match the initial chemical conditions of the disk
  - This result is best explained by each planet accreting its gas near the water ice line of their disk

5.6 Appendix: Role of Mean Motion Resonance in Sculpting HL Tau

We investigated whether or not the disk gaps could be caused by an embryo trapped at a mean motion resonance (MMR) with the inner planet. This embryo would carve a ring out of the dusty disk as it orbits. MMR trapping of Jupiter and Saturn has been used to explain the structure of our inner solar system (Walsh et al., 2011), and requires converging migration between the inner and outer plants. We assume that the inner planet migrates through Type-II migration while the outer planet migrates through Type-I. The requirement of converging migration sets a minimum mass on the outer planet (Pierens & Nelson, 2008; Batygin, 2015; Xu & Lai, 2017). MMR trapping has been shown to be a robust result of a migrating 3-body system in a gas disk by both numerical (Pierens & Nelson, 2008) and analytical (Batygin, 2015; Xu & Lai, 2017) studies.

We require that the migration of the inner and outer planets converge eventually, which is to say that the migration timescales:

$$t_{mig,I}/t_{mig,II} < 1, \tag{5.8}$$

where the Type-I migration timescale is:

$$t_{mig,I} = \left[\frac{1}{r_e}\frac{dr_e}{dt}_I\right]^{-1} = \frac{M_e}{C_T \Sigma \Omega r_e^2}\left(\frac{M_e}{M_*}\right)^{-2}\left(\frac{r_e}{max(H, R_H)}\right)^{-2}, \tag{5.9}$$

where dr_e/dt_I is the migration rate of Type-I migration (equation 5.6) for the embryo. The timescale

Table 5.3: Minimum mass required for converging migration at each of the dust gaps.

Gap location (AU)	Mass ($M_\oplus$)
13.6	0.48
33.3	0.78
65.1	1.66
77.3	2.02
93.0	2.50

of Type-II migration:

$$t_{mig,II} = \left[\frac{1}{r_p}\frac{dr_p}{dt}_{II}\right]^{-1} = \frac{r_p^2}{\nu}, \tag{5.10}$$

where dr_p/dt_{II} is the migration rate of Type-II migration (equation 5.7) for the inner planet. As an example of the requirement in equation 5.8 in the mid-mass model the minimum mass of the embryo is between 0.48 $M_\oplus$ and 2.5 $M_\oplus$ for the five primary gaps in HL Tau (see Table 5.6).

Building planetary embryos of this size at the gap radii is challenging for standard planetesimal accretion because the surface density of both gas and dust is too low for efficient core growth when $r > 10$ AU. An alternative formation model known as the pebble accretion model - where planet cores grow by the accretion of cm-sized pebbles rather than planetesimals - could be used to explain the presence of planetary embryos at large disk radii (see for example Bitsch et al. (2015)). These embryos would have had to form very recently for their masses to be on the order of an Earth mass.

If this hypothesis is correct, we would expect that the gaps in the HL Tau system would line up near the locations of MMR with the inner planet. In that case the orbital period an object in the gap P_{gap} is related to the orbital period of the planet P_{plnt}, such that:

$$\frac{P_{gap}}{P_{plnt}} \simeq \frac{p+q}{p}, \tag{5.11}$$

where $p \geq 1$ and $q \geq 1$ are integers. The simplest case when $p = 1$ describes a system where the planet makes $1 + q$ orbits in the same time as an object in the gap would make one. Given Kepler's laws, eq. 5.11 is rewritten as:

$$r_{gap} = \left[\frac{p+q}{p}\right]^{2/3} r_{plnt}. \tag{5.12}$$

In Figure 5.5 we plot the radial location of MMR with a planet at 2 AU for different values of

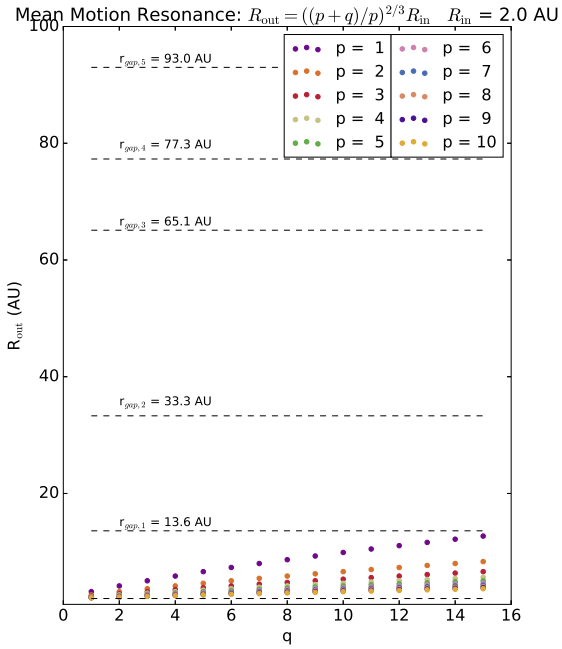

Figure 5.5: Mean motion resonance locations for a planet located at 2 AU. The top 5 dotted black lines denote the radial location of the gaps in HL Tau, the bottom line denotes the location of the inner planet.

p and q. Some of these combinations are redundant, for example (p,q) = (1,1) is dynamically the same as (p,q) = (2,2). It is clear that there are no lower order MMR that can explain any of the dust gaps in the disk. This is because the spacing between MMR radii scales with the radial location of the planet, and hence with the inner planet at 2 AU the radii of MMR can never reach the large radii in the disk. Finally we note that the low order MMR are all within $\sim$ 10 AU which is within the resolution limit of ALMA. As a result, the observations are not sensitive to the dynamical effect of trapping planets at the MMR of our compute planet.

Chapter 6

Conclusions and Future Prospects

In this thesis we have discussed a new method of understanding the chemical composition of exoplanetary atmospheres. This method combines the astrophysics of planet formation with the physics and chemistry of evolving protoplanetary disks to compute the bulk chemical composition of the gas that is accreted onto a forming planet. To achieve this goal we have combined an analytic gas disk model, a numeric dust evolution code, radiative transfer of ionizing radiation, a non-equilibrium chemistry code, the core accretion planet formation model, and the planet trap migration model. This work has examined some important aspects of planet formation theory and protoplanetary disk structure:

1. The chemical composition of an exoplanetary atmosphere will depend on *when* and *where* a planet accretes its gas

2. The particular dust model greatly impacts the size and radial distribution of dust grains, as well as the level of ionization in the gas

3. Set by the gas ionization, the turbulence in the gas dictates the size and evolution of the disk's dead zone

4. Because the dead zone acts as a dynamical trap to Type-I migration, its evolution greatly impacts the planet formation history for the planets trapped at its edge

5. The saturation of the co-rotation torque can occur if a planet trap is within the dead zone of the disk and the mass of trapped planet becomes large

6. If the co-rotation torque saturates in the ice line or heat transition traps, their planets will break free and migrate inward - greatly changing their formation histories

7. Different planet formation histories are encoded in the resulting atmospheric chemical abundances

8. Our computed atmospheric bulk compositions agree well with molecular abundances inferred by emission and transmission spectra observations - our comparisons will be greatly refined by JWST, which will improve both the spectral range and sensitivity of observations.

Throughout this thesis we have stressed the important link between *where* and *when* a planet accretes its gas from the evolving protoplanetary disk in which it forms and the bulk composition of the planet's atmosphere. If a planet migrates within the water ice line before it accretes its gas the C/O of the planet will match the C/O of the disk's gas. This is a typical outcome of our model because:

1. The three dynamic planet traps in our disks evolve to a similar radial location late in the disk lifetime. This result is driven by the overly efficient dust radial drift that rapidly brings the majority of the dust to small radii. Overly efficient radial drift is currently an outstanding issue in the theory of dust physics, and represents an important next step in our understanding of planet formation.

2. The growth of planets which begin in traps beyond the ice line is slow, delaying gas accretion until late in the disk life when it has migrated within / close to the ice line.

As was discussed in chapter 4 this conclusion is consistent within the uncertainties of observations that have compared C/O of a planet to its host star, however is inconsistent with their derived average C/O of exoplanetary atmospheres, where planets tend to be marginally carbon rich (or oxygen depleted) compared to their host star. These observations, along with the work presented here bring us to an important conclusion: studies of atmospheric chemistry *must* be linked to the chemical composition of the host star. Many studies of planetary atmospheres compare the chemical composition of the gas to solar abundances, which is only realistic if the host star is chemically similar to the Sun.

In chapters 2-4 we used initial chemical abundances which matched the results of molecular cloud simulations and compared our results to the chemical composition of observed exoplanets. Based

on our above conclusion, while this tactic is the natural initial assumption to make, it does not necessarily select the chemical abundance which line up with the chemical properties of the host stars. We tried to improve our method of selecting our initial chemical abundances in chapter 5 by modelling a system that has been well studied, both physically and chemically (HL Tau), however there are no known planets in this system with which we may compare our results.

The perfect test bed for our theoretical framework would be a planetary system which included a Hot Jupiter with a well constrained C/O, a host star with a well constrained C/O, and some notion of the original physical conditions of the protoplanetary disk. This last point has not currently been accomplished observationally, because currently all known planetary systems with planets within 10 AU have had their disk evaporated away long ago. Catching a planet in the act of forming is observationally viable with ALMA, and would revolutionize our understanding of this process.

Another approach to testing this theoretical framework is through population synthesis models of planet formation. In these types of models, the important planet formation parameters are randomly selected from preselected probability distributions, and many 1000s of disks are computed. In its current form, running a population synthesis model of our framework would be very computationally expensive, because the evolving astrochemical disk takes $\sim$ month to run when run in parallel on a super computer. Further development is required to speed up the chemical calculations, which would make a population synthesis model more tractable. Assuming that population synthesis is a tractable problem, the primary question that it can solve is: *what is a reasonable range of C/O that can arise in a single disk?* Knowing this would allow us to understand what impact the post formation processes like late planetesimal accretion and physical processing of the atmosphere will have on the observable C/O.

Along with C/O, the nitrogen content and the carbon-to-nitrogen (C/N) have proven to be an interesting avenue of studying the formation histories of planets. Generally we find that the dominate nitrogen-carrying molecule depends on *when* the gas is accreted onto the planet. Early on in the disk's life when the gas is hotter, the nitrogen tends to be in NH_3 while as the disk ages and cool, nitrogen is converted into N_2.

Understanding the nitrogen content in protoplanetary disks is particularity important in the new era of the James Webb Space Telescope (JWST). JWST will give our field improved sensitivity and resolution in the same wavelength bands as the Hubble Space Telescope ($\lesssim 1\mu$m), while also extending our wavelength range towards the mid-infrared ($\sim 10\mu$m). This extended range will result

in the first detection of nitrogen baring species in exoplanetary atmospheres, if NH_3 is common in exoplanetary atmospheres. Determining the nitrogen content of the atmosphere will greatly increase our understanding of planet formation histories.

As our observational understanding of planetary atmospheres improves an important link between our work and the observations will need to be undertaken. That is, the processing of the bulk chemical composition of the gas once it is accreted onto the planet. Currently our method only computes the total chemical abundances of gas species as they accrete, however chemical and physical processes can change these abundances over the billions of years between the formation and observation of a given planet. To what extent the molecular abundance will change is currently beyond the scope of this work, however we do find that our predicted abundances agree will with the abundances that have been inferred through emission and transmission spectra observations of exoplanetary atmospheres by the Hubble Space Telescope.

A second source of volatile delivery that is recently gathering some attention (ie. Mordasini et al. (2016) and Booth et al. (2017)) is the delivery through the accretion of planetesimals or pebbles covered in ices. This is believed to be a method of enhancing the metallicity of giant planets in our own solar system (for example Jupiter is carbon-rich compared to solar abundances), and could be very important for the production of atmospheres around super-earths. In principle we can easily add the effect of accreting ices and grains to our theoretical work because our chemical code keeps track of the ice component for a few 100 chemical species. This small addition could lead to a variation in the C/O in our computed planets because of where they accreted their solids.

Along with these other additions to our model, I will look to improve the computational efficiency of our chemical model, in order to facilitate the use of a full population synthesis model. Additionally our model is generally agnostic to which planet formation theory is used to build planet cores, and can offer a useful tool for testing the chemical composition of planetary atmospheres formed in both pebble accretion and planetesimal accretion models. In this way, we may rely on chemistry to teach us more about the physics of protoplanetary disk evolution and planet formation.

Bibliography

Aikawa Y., Herbst E., 1999, A&A, 351, 233

Akimkin V. V., 2015, Astronomy Reports, 59, 747

Akimkin V. V., Kirsanova M. S., Pavlyuchenkov Y. N., Wiebe D. S., 2015, MNRAS, 449, 440

Alessi M., Pudritz R. E., Cridland A. J., 2017, MNRAS, 464, 428

Alexander R., Pascucci I., Andrews S., Armitage P., Cieza L., 2014, Protostars and Planets VI, 475

Ali-Dib M., 2017, MNRAS, 464, 4282

Ali-Dib M., Mousis O., Petit J.-M., Lunine J. I., 2014, ApJ, 793, 9

Alibert Y., Mordasini C., Benz W., Winisdoerffer C., 2005, A&A, 434, 343

ALMA Partnership et al., 2015, ApJL, 808, L3

Alonso R. et al., 2004, ApJL, 613, L153

Andrews S. M., Rosenfeld K. A., Kraus A. L., Wilner D. J., 2013, ApJ, 771, 129

Andrews S. M. et al., 2016, ApJL, 820, L40

Bai X.-N., Stone J. M., 2011, ApJ, 736, 144

Bai X.-N., Stone J. M., 2013, ApJ, 769, 76

Bai X.-N., Stone J. M., 2017, ApJ, 836, 46

Baillié K., Charnoz S., 2014, ApJ, 786, 35

Baillié K., Charnoz S., Pantin E., 2015, A&A, 577, A65

Balbus S. A., Hawley J. F., 1991a, ApJ, 376, 214

Balbus S. A., Hawley J. F., 1991b, ApJ, 376, 214

Balbus S. A., Hawley J. F., 1994, MNRAS, 266, 769

Banzatti A., Pinilla P., Ricci L., Pontoppidan K. M., Birnstiel T., Ciesla F., 2015, ApJL, 815, L15

Batalha N. M. et al., 2013, ApJS, 204, 24

Batygin K., 2015, MNRAS, 451, 2589

Beckwith S. V. W., Sargent A. I., 1996, Nature, 383, 139

Beitz E., Güttler C., Blum J., Meisner T., Teiser J., Wurm G., 2011, ApJ, 736, 34

Bell K. R., Cassen P. M., Klahr H. H., Henning T., 1997, ApJ, 486, 372

Bell K. R., Lin D. N. C., 1994, ApJ, 427, 987

Benneke B., 2015, ArXiv e-prints

Bergin E., Calvet N., D'Alessio P., Herczeg G. J., 2003, ApJL, 591, L159

Bergin E. A., Blake G. A., Ciesla F., Hirschmann M. M., Li J., 2015, Proceedings of the National Academy of Science, 112, 8965

Bertout C., 1989, ARA&A, 27, 351

Bethell T. J., Bergin E. A., 2011a, ApJ, 740, 7

Bethell T. J., Bergin E. A., 2011b, ApJ, 739, 78

Birnstiel T., 2016, Zenodo

Birnstiel T., Andrews S. M., Pinilla P., Kama M., 2015, ApJL, 813, L14

Birnstiel T., Dullemond C. P., Brauer F., 2009, A&A, 503, L5

Birnstiel T., Dullemond C. P., Brauer F., 2010, A&A, 513, A79

Birnstiel T., Klahr H., Ercolano B., 2012, A&A, 539, A148

Birnstiel T., Windmark F., Dullemond C. P., Klahr H., 2011, in LPI Contributions, Vol. 1639, Workshop on Formation of the First Solids in the Solar System, p. 9063

Bitner M. A. et al., 2008, ApJ, 688, 1326

Bitsch B., Crida A., Morbidelli A., Kley W., Dobbs-Dixon I., 2013, A&A, 549, A124

Bitsch B., Lambrechts M., Johansen A., 2015, A&A, 582, A112

Blaes O. M., Balbus S. A., 1994, ApJ, 421, 163

Blum J., Wurm G., 2000, Icarus, 143, 138

Blum J., Wurm G., 2008a, ARA&A, 46, 21

Blum J., Wurm G., 2008b, ARA&A, 46, 21

Bolton S. J. et al., 2017, Science, 356, 821

Booth R. A., Clarke C. J., Madhusudhan N., Ilee J. D., 2017, MNRAS, 469, 3994

Borkowski K. J., Dwek E., 1995, ApJ, 454, 254

Brauer F., Dullemond C. P., Henning T., 2008, A&A, 480, 859

Brewer J. M., Fischer D. A., Madhusudhan N., 2017, AJ, 153, 83

Brogi M., de Kok R. J., Albrecht S., Snellen I. A. G., Birkby J. L., Schwarz H., 2016, ApJ, 817, 106

Brouwers M. G., Vazan A., Ormel C. W., 2017, ArXiv e-prints

Carrasco-González C. et al., 2016, ApJL, 821, L16

Chabrier G., 2003, PASP, 115, 763

Chambers J. E., 2009, ApJ, 705, 1206

Chiang E. I., Goldreich P., 1997, ApJ, 490, 368

Cieza L., Williams J., Kourkchi E., Andrews S., Casassus S., Graves S., Schreiber M. R., 2015, MNRAS, 454, 1909

Cieza L. A. et al., 2016, Nature, 535, 258

Cleeves L. I., Bergin E. A., Adams F. C., 2014, ApJ, 794, 123

Cleeves L. I., Bergin E. A., Qi C., Adams F. C., Öberg K. I., 2015, ApJ, 799, 204

Coleman G. A. L., Nelson R. P., 2014, MNRAS, 445, 479

Coleman G. A. L., Nelson R. P., 2016, MNRAS, 460, 2779

Cridland A. J., Pudritz R. E., Alessi M., 2016, MNRAS, 461, 3274

Cridland A. J., Pudritz R. E., Birnstiel T., 2017a, MNRAS, 465, 3865

Cridland A. J., Pudritz R. E., Birnstiel T., Cleeves L. I., Bergin E. A., 2017b, ArXiv e-prints

Croll B. et al., 2015, ApJ, 802, 28

Cuzzi J. N., Hogan R. C., Paque J. M., Dobrovolskis A. R., 2001, ApJ, 546, 496

D'Alessio P., Calvet N., Hartmann L., Franco-Hernández R., Servín H., 2006, ApJ, 638, 314

D'Alessio P., Calvet N., Hartmann L., Lizano S., Cantó J., 1999, ApJ, 527, 893

D'Alessio P., Cantö J., Calvet N., Lizano S., 1998, ApJ, 500, 411

Dipierro G., Price D., Laibe G., Hirsh K., Cerioli A., Lodato G., 2015, MNRAS, 453, L73

Dittkrist K.-M., Mordasini C., Klahr H., Alibert Y., Henning T., 2014, A&A, 567, A121

Dohnanyi J. S., 1969, JGR, 74, 2531

Dong R., Li S., Chiang E., Li H., 2017, ApJ, 843, 127

Draine B. T., 2003, ApJ, 598, 1026

Draine B. T., Lee H. M., 1984, ApJ, 285, 89

Dubrulle B., Morfill G., Sterzik M., 1995, Icarus, 114, 237

Dullemond C. P., 2012, RADMC-3D: A multi-purpose radiative transfer tool. Astrophysics Source Code Library

Dullemond C. P., Dominik C., 2005, A&A, 434, 971

Dutrey A. et al., 2014, Protostars and Planets VI, 317

Eistrup C., Walsh C., van Dishoeck E. F., 2016, A&A, 595, A83

Fogel J. K. J., Bethell T. J., Bergin E. A., Calvet N., Semenov D., 2011, ApJ, 726, 29

Fortney J. J., Marley M. S., Lodders K., Saumon D., Freedman R., 2005, ApJL, 627, L69

Frank J., King A. R., Raine D. J., 1985, Accretion power in astrophysics, Cambridge and New York, Cambridge University Press, 1985, 283 p.

Fromang S., 2013, in EAS Publications Series, Vol. 62, EAS Publications Series, Hennebelle P., Charbonnel C., eds., pp. 95–142

Fromang S., Nelson R. P., 2009, A&A, 496, 597

Gammie C. F., 1996, ApJ, 457, 355

Gomes R., Levison H. F., Tsiganis K., Morbidelli A., 2005, Nature, 435, 466

Gorti U., Hollenbach D., Dullemond C. P., 2015, ApJ, 804, 29

Gressel O., Pessah M. E., 2015, ApJ, 810, 59

Gressel O., Turner N. J., Nelson R. P., McNally C. P., 2015, ApJ, 801, 84

Gundlach B., Blum J., 2015, ApJ, 798, 34

Gundlach B., Blum J., 2016, A&A, 589, A111

Gundlach B., Kilias S., Beitz E., Blum J., 2011, Icarus, 214, 717

Haisch, Jr. K. E., Lada E. A., Lada C. J., 2001, ApJL, 553, L153

Hartmann L., 2009, Accretion Processes in Star Formation: Second Edition. Cambridge University Press

Hasegawa Y., Pudritz R. E., 2010, ApJL, 710, L167

Hasegawa Y., Pudritz R. E., 2011, MNRAS, 417, 1236

Hasegawa Y., Pudritz R. E., 2012, ApJ, 760, 117

Hasegawa Y., Pudritz R. E., 2013, ApJ, 778, 78

Hayashi C., 1961, PASJ, 13

Helling C., Woitke P., Rimmer P. B., Kamp I., Thi W.-F., Meijerink R., 2014, Life, 4

Henning T., Semenov D., 2013, Chemical Reviews, 113, 9016

Herbst E., Klemperer W., 1973, ApJ, 185, 505

Hernández J. et al., 2007, ApJ, 671, 1784

Ida S., Lin D. N. C., 2004, ApJ, 604, 388

Ida S., Lin D. N. C., Nagasawa M., 2013, ApJ, 775, 42

Ikoma M., Nakazawa K., Emori H., 2000, ApJ, 537, 1013

Jin M., Lee J.-E., Kim K.-T., Evans, II N. J., 2016, ApJS, 225, 21

Johansen A., Klahr H., Henning T., 2011, A&A, 529, A62

Johansen A., Oishi J. S., Mac Low M.-M., Klahr H., Henning T., Youdin A., 2007, Nature, 448, 1022

Jørgensen J. K., Favre C., Bisschop S. E., Bourke T. L., van Dishoeck E. F., Schmalzl M., 2012, ApJL, 757, L4

Kane S. R., Ciardi D. R., Gelino D. M., von Braun K., 2012, MNRAS, 425, 757

Kastner J. H., Huenemoerder D. P., Schulz N. S., Canizares C. R., Weintraub D. A., 2002, ApJ, 567, 434

Kastner J. H., Huenemoerder D. P., Schulz N. S., Weintraub D. A., 1999, ApJ, 525, 837

Kastner J. H., Zuckerman B., Weintraub D. A., Forveille T., 1997, Science, 277, 67

Kataria T., Sing D. K., Lewis N. K., Visscher C., Showman A. P., Fortney J. J., Marley M. S., 2016, ApJ, 821, 9

Kenyon S. J., Hartmann L., 1987, ApJ, 323, 714

Kley W., 1999, MNRAS, 303, 696

Kokubo E., Ida S., 1998, Icarus, 131, 171

Kokubo E., Ida S., 2002, ApJ, 581, 666

Konopacky Q. M., Barman T. S., Macintosh B. A., Marois C., 2014, in IAU Symposium, Vol. 299, Exploring the Formation and Evolution of Planetary Systems, Booth M., Matthews B. C., Graham J. R., eds., pp. 297–298

Kreidberg L. et al., 2014, ApJL, 793, L27

Kunz M. W., Balbus S. A., 2004, MNRAS, 348, 355

Lavie B. et al., 2016, ArXiv e-prints

Lee J.-M., Fletcher L. N., Irwin P. G. J., 2012, MNRAS, 420, 170

Lee J.-M., Heng K., Irwin P. G. J., 2013, ApJ, 778, 97

Lesniak M. V., Desch S. J., 2011, ApJ, 740, 118

Lin D. N. C., Papaloizou J., 1986, ApJ, 309, 846

Lin D. N. C., Papaloizou J. C. B., 1993, in Protostars and Planets III, Levy E. H., Lunine J. I., eds., pp. 749–835

Line M. R., Knutson H., Wolf A. S., Yung Y. L., 2014a, ApJ, 783, 70

Line M. R., Knutson H., Wolf A. S., Yung Y. L., 2014b, ApJ, 783, 70

Line M. R., Vasisht G., Chen P., Angerhausen D., Yung Y. L., 2011, ApJ, 738, 32

Lissauer J. J., Hubickyj O., D'Angelo G., Bodenheimer P., 2009, Icarus, 199, 338

Lubow S. H., Seibert M., Artymowicz P., 1999, ApJ, 526, 1001

Lynden-Bell D., Pringle J. E., 1974, MNRAS, 168, 603

Lyra W., Mac Low M.-M., 2012, ApJ, 756, 62

Lyra W., Paardekooper S.-J., Mac Low M.-M., 2010, ApJL, 715, L68

MacDonald R. J., Madhusudhan N., 2017, ArXiv e-prints

Madhusudhan N., Agúndez M., Moses J. I., Hu Y., 2016a, Space Sci. Rev., 205, 285

Madhusudhan N., Amin M. A., Kennedy G. M., 2014a, ApJL, 794, L12

Madhusudhan N., Amin M. A., Kennedy G. M., 2014b, ApJL, 794, L12

Madhusudhan N., Bitsch B., Johansen A., Eriksson L., 2016b, ArXiv e-prints

Madhusudhan N., Seager S., 2009, ApJ, 707, 24

Madhusudhan N., Seager S., 2010, ApJ, 725, 261

Makino J., Fukushige T., Funato Y., Kokubo E., 1998, New Astronomy, 3, 411

Marley M. S., Saumon D., Guillot T., Freedman R. S., Hubbard W. B., Burrows A., Lunine J. I., 1996, Science, 272, 1919

Masset F. S., 2002, A&A, 387, 605

Masset F. S., Morbidelli A., Crida A., Ferreira J., 2006, ApJ, 642, 478

Masset F. S., Papaloizou J. C. B., 2003, ApJ, 588, 494

Mathis J. S., Rumpl W., Nordsieck K. H., 1977, ApJ, 217, 425

Matsumura S., Pudritz R. E., 2003, ApJ, 598, 645

Matsumura S., Pudritz R. E., 2006, MNRAS, 365, 572

Matsumura S., Pudritz R. E., Thommes E. W., 2009, ApJ, 691, 1764

McCaughrean M. J., O'dell C. R., 1996, AJ, 111, 1977

McElroy D., Walsh C., Markwick A. J., Cordiner M. A., Smith K., Millar T. J., 2013, A&A, 550, A36

Mendoza V. E. E., 1966, ApJ, 143, 1010

Men'shchikov A. B., Henning T., Fischer O., 1999, ApJ, 519, 257

Miguel Y., Kaltenegger L., 2014, ApJ, 780, 166

Miyake K., Nakagawa Y., 1993, Icarus, 106, 20

Montalto M., Iro N., Santos N. C., Desidera S., Martins J. H. C., Figueira P., Alonso R., 2015, ApJ, 811, 55

Mordasini C., Alibert Y., Georgy C., Dittkrist K.-M., Klahr H., Henning T., 2012, A&A, 547, A112

Mordasini C., Klahr H., Alibert Y., Miller N., Henning T., 2014, A&A, 566, A141

Mordasini C., Mollière P., Dittkrist K.-M., Jin S., Alibert Y., 2015, International Journal of Astrobiology, 14, 201

Mordasini C., van Boekel R., Mollière P., Henning T., Benneke B., 2016, ApJ, 832, 41

Moriarty J., Madhusudhan N., Fischer D., 2014, ApJ, 787, 81

Moses J. I., Madhusudhan N., Visscher C., Freedman R. S., 2013, ApJ, 763, 25

Natta A., Testi L., Calvet N., Henning T., Waters R., Wilner D., 2007, Protostars and Planets V, 767

Öberg K. I., Bergin E. A., 2016, ApJL, 831, L19

Öberg K. I., Murray-Clay R., Bergin E. A., 2011, ApJL, 743, L16

Oklopčić A., Hirata C. M., Heng K., 2016, ApJ, 832, 30

Okuzumi S., Momose M., Sirono S.-i., Kobayashi H., Tanaka H., 2016, ApJ, 821, 82

Ormel C. W., Kuiper R., Shi J.-M., 2015, MNRAS, 446, 1026

Paardekooper S.-J., 2014, MNRAS, 444, 2031

Paardekooper S.-J., Baruteau C., Crida A., Kley W., 2010, MNRAS, 401, 1950

Paardekooper S.-J., Baruteau C., Kley W., 2011, MNRAS, 410, 293

Papaloizou J. C. B., Terquem C., 1999, ApJ, 521, 823

Pérez L. M. et al., 2012, ApJL, 760, L17

Pierens A., Nelson R. P., 2008, A&A, 482, 333

Pignatale F. C., Maddison S. T., Taquet V., Brooks G., Liffman K., 2011, MNRAS, 414, 2386

Pinilla P., Birnstiel T., Ricci L., Dullemond C. P., Uribe A. L., Testi L., Natta A., 2012, A&A, 538, A114

Pontoppidan K. M., Salyk C., Bergin E. A., Brittain S., Marty B., Mousis O., Öberg K. I., 2014, Protostars and Planets VI, 363

Pudritz R. E., Norman C. A., 1983, ApJ, 274, 677

Pudritz R. E., Ouyed R., Fendt C., Brandenburg A., 2007, Protostars and Planets V, 277

Qi C., Öberg K. I., Andrews S. M., Wilner D. J., Bergin E. A., Hughes A. M., Hogherheijde M., D'Alessio P., 2015, ApJ, 813, 128

Qi C., Öberg K. I., Wilner D. J., 2013, ApJ, 765, 34

Raettig N., Klahr H., Lyra W., 2015, ApJ, 804, 35

Ranjan S., Charbonneau D., Désert J.-M., Madhusudhan N., Deming D., Wilkins A., Mandell A. M., 2014, ApJ, 785, 148

Ricci L., Testi L., Natta A., Neri R., Cabrit S., Herczeg G. J., 2010, A&A, 512, A15

Richert A. J. W., Feigelson E. D., Getman K. V., Kuhn M. A., 2015, ApJ, 811, 10

Ros K., Johansen A., 2013, A&A, 552, A137

Rowe J. F. et al., 2014, ApJ, 784, 45

Ruden S. P., 1993, in Astronomical Society of the Pacific Conference Series, Vol. 36, Planets Around Pulsars, Phillips J. A., Thorsett S. E., Kulkarni S. R., eds., pp. 197–215

Safronov V. S., 1966, Soviet Astronomy, 9, 987

Schäfer C., Speith R., Kley W., 2007, A&A, 470, 733

Schäfer U., Yang C.-C., Johansen A., 2017, A&A, 597, A69

Schwarz K. R., Bergin E. A., Cleeves L. I., Blake G. A., Zhang K., Öberg K. I., van Dishoeck E. F., Qi C., 2016, ApJ, 823, 91

Seager S., 2010, Exoplanets, edited by S. Seager. Tucson, AZ: University of Arizona Press, 2010, 526 pp. ISBN 978-0-8165-2945-2

Seager S., Deming D., 2010, ARA&A, 48, 631

Semenov D. et al., 2010, A&A, 522, A42

Semenov D., Wiebe D., 2011, ApJS, 196, 25

Semenov D. A., 2011, in IAU Symposium, Vol. 280, The Molecular Universe, Cernicharo J., Bachiller R., eds., pp. 114–126

Shakura N. I., Sunyaev R. A., 1973, A&A, 24, 337

Simon J. B., Bai X.-N., Stone J. M., Armitage P. J., Beckwith K., 2013, ApJ, 764, 66

Sing D. K. et al., 2015, MNRAS, 446, 2428

Sirono S.-i., 2011, ApJ, 735, 131

Smith I. W. M., Herbst E., Chang Q., 2004, MNRAS, 350, 323

Snellen I. et al., 2015, A&A, 576, A59

Stammler S. M., Birnstiel T., Panić O., Dullemond C. P., Dominik C., 2017, A&A, 600, A140

Stepinski T. F., 1998, Icarus, 132, 100

Stevenson K. B. et al., 2010, Nature, 464, 1161

Strom K. M., Strom S. E., Edwards S., Cabrit S., Skrutskie M. F., 1989, AJ, 97, 1451

Tamayo D., Triaud A. H. M. J., Menou K., Rein H., 2015, ApJ, 805, 100

Tanaka H., Inaba S., Nakazawa K., 1996, Icarus, 123, 450

Tazzari M. et al., 2016, A&A, 588, A53

Testi L. et al., 2014, Protostars and Planets VI, 339

Thi W. F., Kamp I., Woitke P., van der Plas G., Bertelsen R., Wiesenfeld L., 2013, A&A, 551, A49

Thiabaud A., Marboeuf U., Alibert Y., Leya I., Mezger K., 2015, A&A, 574, A138

Tielens A. G. G. M., 2005, The Physics and Chemistry of the Interstellar Medium, by A. G. G. M. Tielens, pp. . ISBN 0521826349. Cambridge, UK: Cambridge University Press, 2005.

Turner N. J., Sano T., Dziourkevitch N., 2007, ApJ, 659, 729

Van Grootel V. et al., 2014, ApJ, 786, 2

Venot O., Agúndez M., Selsis F., Tessenyi M., Iro N., 2014, A&A, 562, A51

Wada K., Tanaka H., Suyama T., Kimura H., Yamamoto T., 2008, ApJ, 677, 1296

Wada K., Tanaka H., Suyama T., Kimura H., Yamamoto T., 2009, ApJ, 702, 1490

Wakeford H. R., Sing D. K., 2015, A&A, 573, A122

Wakeford H. R., Visscher C., Lewis N. K., Kataria T., Marley M. S., Fortney J. J., Mandell A. M., 2017, MNRAS, 464, 4247

Walsh C., Millar T. J., Nomura H., 2013, ApJL, 766, L23

Walsh C., Nomura H., Millar T. J., Aikawa Y., 2012, ApJ, 747, 114

Walsh K. J., Morbidelli A., Raymond S. N., O'Brien D. P., Mandell A. M., 2011, Nature, 475, 206

Ward W. R., 1991, in Lunar and Planetary Inst. Technical Report, Vol. 22, Lunar and Planetary Science Conference

Ward W. R., 1997, ApJL, 482, L211

Watson W. D., Salpeter E. E., 1972, ApJ, 174, 321

Weidenschilling S. J., 1977, MNRAS, 180, 57

Weingartner J. C., Draine B. T., 2001, ApJ, 548, 296

Whipple F. L., 1973, NASA Special Publication, 319, 355

White R. J., Hillenbrand L. A., 2004, ApJ, 616, 998

Wilking B. A., Lada C. J., Young E. T., 1989, ApJ, 340, 823

Willacy K., Langer W. D., 2000, ApJ, 544, 903

Williams J. P., Cieza L. A., 2011, ARA&A, 49, 67

Williams J. P. et al., 2013, MNRAS, 435, 1671

Wilson P. A. et al., 2015, MNRAS, 450, 192

Woitke P., Kamp I., Thi W.-F., 2009, A&A, 501, 383

Woodall J., Agúndez M., Markwick-Kemper A. J., Millar T. J., 2007, A&A, 466, 1197

Wyttenbach A., Ehrenreich D., Lovis C., Udry S., Pepe F., 2015, A&A, 577, A62

Xu W., Lai D., 2017, MNRAS, 468, 3223

Yang H. et al., 2012, ApJ, 744, 121

Youdin A. N., Goodman J., 2005, ApJ, 620, 459

Zhang K., Blake G. A., Bergin E. A., 2015, ApJL, 806, L7

Zhang K., Pontoppidan K. M., Salyk C., Blake G. A., 2013, ApJ, 766, 82

Zheng X., Kouwenhoven M. B. N., Wang L., 2015, MNRAS, 453, 2759